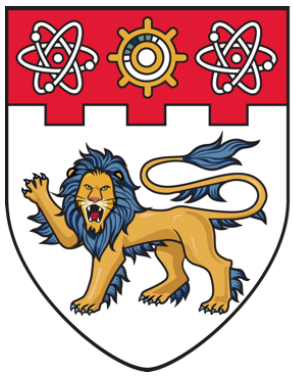

NANYANG TECHNOLOGICAL UNIVERSITY
SINGAPORE

ELECTRON BACKSCATTER DIFFRACTION STUDY FOR ADVANCED SEMICONDUCTOR INTERCONNECT MATERIALS ANALYSIS

LEE WAI KEN AARON

SCHOOL OF MATERIALS SCIENCE AND ENGINEERING

2022

ELECTRON BACKSCATTER DIFFRACTION STUDY FOR ADVANCED SEMICONDUCTOR INTERCONNECT MATERIALS ANALYSIS

LEE WAI KEN AARON

SCHOOL OF MATERIALS SCIENCE AND ENGINEERING

A thesis submitted to the Nanyang Technological University
in partial fulfilment of the requirement for the degree of
Master of Engineering

2022

Statement of Originality

I hereby certify that the work embodied in this thesis is the result of original research, is free of plagiarised materials, and has not been submitted for a higher degree to any other University or Institution.

3 June 2022

. . . . . .
Date

. . . . . .
Lee Wai Ken Aaron

Supervisor Declaration Statement

I have reviewed the content and presentation style of this thesis and declare it is free of plagiarism and of sufficient grammatical clarity to be examined. To the best of my knowledge, the research and writing are those of the candidate except as acknowledged in the Author Attribution Statement. I confirm that the investigations were conducted in accord with the ethics policies and integrity standards of Nanyang Technological University and that the research data are presented honestly and without prejudice.

3 June 2022

. . . . . .

Date

. . . . . .

Prof. Gan Chee Lip

Authorship Attribution Statement

This thesis contains material from 1 paper accepted in the following conference in which I am listed as an author.

Chapter 5 is published as A. Lee, B. Zee and F.J. Foo, "Application of EBSD Study of Cu-Sn IMCs in SAC305 and Sn0.7Cu Solder Joints to Determine the Suitability of Sn0.7Cu Solder as Alternative in Mitigating ILD Cracks/Delamination," in proceedings of the 23rd Electronics Packaging Technology Conference (EPTC), 2021.

The contributions of the co-authors are as follows:

- B. Zee provided the initial project direction and scope.
- I co-designed the study with B. Zee.
- I performed all the laboratory work at the Advanced Micro Devices, Inc (Singapore) Device Analysis Laboratory. I also analyzed the data and prepared the manuscript draft.
- The manuscript was revised by B. Zee and F.J. Foo.

3 June 2022

. . . . . .
Date

. . . . . .
Lee Wai Ken Aaron

Abstract

3-dimensional (3D) semiconductor packaging and interconnection technology, which involves vertically stack IC chips that are electrically interconnected by inter-layer vias and solder joints, is being used to achieve better performance, lower power consumption, and higher integration capability. As interconnects continue to shrink and become denser, it is increasingly important to characterize their microstructure such as grain size and crystallographic orientation, to ensure that these interconnects, are robust and able to survive thermo-mechanical stresses during assembly, reliability testing as well as in field usage. Furthermore, interlayer dielectric (ILD) cracking and delamination still remains a concern. The use of brittle extreme-low *k* (ELK) dielectrics together with lead-free tin-silver-copper solder and stiff copper (Cu) pillars can increase the risk of this occurrence. A possible solution to mitigate this risk is to use a lower modulus solder. However, this may favor the formation of brittle intermetallic compounds (IMCs) in the solder joints and compromising the overall reliability performance of devices. Therefore, a study of the IMCs in the solder joints would be necessary.

Electron backscatter diffraction (EBSD) is a technique which can be used to understand the crystallographic structures of the IMCs, which may influence its reliability. For EBSD analysis to be productive, useful data that allows the crystallographic information to be extracted from must first be obtained from the sample. To achieve this, the analyzed sample has to be optimally prepared. As conventional sample preparation methods for electron microscopy inspection may not be sufficient for the stringent conditions that EBSD samples require, a modified sample preparation workflow is explored and validated as well.

A study of the substrate side IMCs was carried out on SAC305 and Sn0.7Cu solders. A comparison of the IMCs microstructure was done under temperature cycling as well as high temperature storage with the use of energy dispersive x-ray spectroscopy (EDX) and EBSD techniques. Results showed that no significant difference was observed between the IMCs of both substrate solders, validating Sn0.7Cu solder as a viable alternative to conventional SAC305 solder in mitigating ILD cracks and delamination risks.

Lay Summary

With the advancement of semiconductor technologies, miniaturization of transistors and components are becoming more prevalent. As the scaling of components such as solder joints continue to shrink and become denser, it becomes increasingly important to better understand their microstructure and how it may change during testing under conditions similar to its working environment. This is due to the fact that cracking and delamination in the dielectric layers of devices still remain a concern. A possible solution to mitigate this risk is to use a more ductile solder in the solder joints. However, this may lead to the formation of brittle intermetallic compounds (IMCs) in the solder joints and compromising the overall reliability performance of devices. Therefore, a study of the IMCs in the solder joints would be necessary.

Electron backscatter diffraction (EBSD) is a technique which can be used to understand the microstructure of the intermetallic compounds in greater detail. In EBSD analysis, useful microstructure data that provides insights to the properties of the material can be extracted from the sample. However, EBSD analysis will require extensive sample preparation to ensure that the sample surface finish is optimally prepared. As conventional sample preparation methods for electron microscopy inspection may not be sufficient for the stringent conditions that EBSD samples require, a modified sample preparation workflow is explored and validated. This modified sample preparation was shown to be suitable for EBSD analysis.

A comparison of IMCs formed at the substrate side was done between SAC305 and Sn0.7Cu solders under temperature cycling and high temperature storage conditions. Using the techniques of energy dispersive x-ray spectroscopy EDX and EBSD, the analysis results showed that for both substrate solders, there was no significant difference observed in the IMCs, confirming Sn0.7Cu solder as a suitable alternative in mitigating the risk of ILD cracks and delamination.

Acknowledgements

This project is jointly carried out by Advanced Micro Devices (AMD), Inc (Singapore) and Nanyang Technological University (NTU) Singapore under the Industrial Postgraduate Program (IPP) sponsored by the Economic Development Board (EDB).

The author would like to sincerely thank the following people for their invaluable guidance, support, and contributions towards the success of this project:

- Professor Gan Chee Lip, Project Supervisor (NTU)
- Associate Professor Dong Zhili, Project Co-supervisor (NTU)
- Ms. Bernice Zee, Project Supervisor (AMD)
- Mr. Foo Fang Jie, Manager Package Level Failure Analysis (AMD)
- Colleagues of Device Analysis Lab (AMD)
- Dr Wu Jiang, Senior Application Specialist (Oxford Instruments)
- Dr Eugene Choo, Field Service and Application Engineer (Oxford Instruments)
- Ms. Angela Hu, Sales and Application Specialist (Leica Microsystems)

Table of Contents

Table Captions

Figure Captions

Abbreviations

IC	Integrated Circuit
EBSD	Electron Backscatter Diffraction
IMC	Intermetallic Compound
BEOL	Back End of Line
ELK	Extreme Low-*k*
TC	Thermal Cycling
CTE	Coefficient of Thermal Expansion
EBSP	Electron Backscatter Pattern
EDX	Energy Dispersive X-ray
IPF	Inverse Pole Figure
SEM	Scanning Electron Microscope
ENEPIG	Electroless Nickel-Electroless Palladium-Immersion Gold
HTS	High Temperature Storage
SiC	Silicon Carbide
MAD	Mean Angular Deviation
FIB	Focused Ion Beam
BIB	Broad Ion Beam
IQ	Image Quality
NIST	National Institute of Standards and Technology
ICSD	Inorganic Crystal Structure Database
COM	Crystal Orientation Map
EM	Electromigration
FEA	Finite Element Analysis

Chapter 1

Introduction

With the advancement of semiconductor technologies, miniaturization of transistors and components are becoming more commonplace. This has resulted in the shrinkage and densification of interconnects such as solder joints. Consequently, it has become increasingly important to understand interconnect microstructure and how it may change during testing under conditions similar to its working environment. This is because cracking and delamination in the dielectric layers in the back end of line (BEOL) of devices remains a concern. A possible solution to mitigate this risk is to use a more ductile solder in the solder joints. However, this may favor the formation of brittle intermetallic compounds (IMCs) in the solder joints and compromising the overall reliability performance of devices. Therefore, a study of the IMCs in the solder joints would be necessary.

1.1 Background

Over the years, there have been incredible advancements in the manufacturing of integrated circuits (ICs), with feature size shrinking from 10 μm down to 7 nm. With each technology node, feature size has shrunk by almost 0.7 times, with the number of transistors in a chip doubling. This continuous scaling of device dimensions enables more devices to be packed into the same area of a semiconductor microprocessor, thus allowing it to vastly improve its performance [1]. As device dimensions scale down, interconnects will also have to scale in size to keep pace.

With interconnect size continuously shrinking and getting denser, it is also increasingly important that the interconnects remain reliable throughout its lifetime. During applications, interconnects are likely to fail after a period of time due to repeated mechanical or thermal influences. Therefore, in an effort to study and predict the long-term reliability of the interconnects, reliability tests such as thermal aging or thermal cycling are commonly conducted across the industry [2]. Studying the effects that these reliability tests have on the microstructure of the interconnects and characterizing them will aid in the understanding of failure mechanisms and the optimization of assembly processes to develop more reliable interconnects. Furthermore, interlayer dielectric (ILD) cracking and delamination continues to remain as a concern. To this end, exploration of possible solutions to mitigate crack or delamination risk is crucial. One such possibility is through the use of alternative solders in solder joints. Hence, with the exploration of alternative solders, analysis techniques to allow for more detailed and accurate materials characterization is necessary.

1.2 Motivation

In order to understand if an alternative solder is possible in mitigating ILD cracks and delamination, the study and characterization of the solder joint's microstructure in greater detail is necessary. Electron backscatter diffraction (EBSD) is one such technique which allows the study and understanding of crystallographic properties such as crystal orientation, grain size and grain boundary distribution in the solder joints. As such, exploration into this analysis technique and building up its capability play a key role in the study of interconnect reliability.

Prior to EBSD analysis, sample preparation is a crucial step of equal importance since EBSD is a surface analytical technique where information is obtained from only a few tens of nanometers of the sample surface [3]. It is therefore necessary to ensure that the sample surface to be analyzed is of optimal quality and condition, with no deformation present, so as to gather useful information from the EBSD analysis. Although most materials can be prepared with a standard mechanical grinding and polishing workflow, preparation remains a challenge for heterogeneous samples with a variety of materials present, such as solder joints. As different materials respond differently to these standard preparation methods, the sample of interest will usually need to be considered on an individual basis and prepared accordingly. Hence, there is a need to understand how solder joint samples can be best prepared for EBSD analysis. In addition to the standard sample preparation methods, ion beam techniques will also be explored for sample preparation in this study.

Having successfully prepared a workflow for sample preparation that meets the requirements for EBSD analysis, the technique of EBSD itself also has to be optimized for the microstructural analysis of the interconnects. As most interconnect materials are polycrystalline, it is essential to have techniques such as this to allow for the in-depth study of the interconnect microstructures. Thus, in addition to sample preparation workflow and techniques, this report will also document the building up of EBSD capabilities and the analysis of the EBSD data collected to establish the relationship between the microstructure and reliability of interconnects.

1.3 Objective and Scope

The objective of this project covers the development of key sample preparation steps, EBSD analysis workflow and the study of reliability testing such as temperature cycling and high temperature storage on the solder joint-substrate IMC microstructure. Sample preparation and EBSD study will be conducted on copper (Cu) pillar solder joints. Sample preparation workflows, parameters and techniques used to achieve the sample finishes required for EBSD analysis will be documented in addition to EBSD setup parameters and analysis results. Comparison between SAC305 solder and Sn0.7Cu substrate solder IMCs will also be done to determine if there are any significant differences between the IMC formation in the two solders.

1.4 Expected Outcomes/Challenges

Current methods of sample preparation used for scanning electron microscopy (SEM) inspection mainly employs mechanical sectioning, grinding and polishing techniques. Though sufficient for most SEM analysis, surface finish conditions are more stringent for EBSD analysis. Therefore, further exploration into techniques such as ion beam polishing and modifications to the standard sample preparation workflow are being considered. Furthermore, as EBSD is a newly procured capability in AMD, setup and parameters used for analysis are based on knowledge and readings and built up from scratch. Hence, trials on the various parameters in EBSD are essential before a suitable reference condition can be determined and be used for the interconnect studies.

Sn0.7Cu is expected to be a possible alternative to SAC305 solder in mitigating ILD cracks and delamination. Although having a slightly higher Cu content, Sn0.7Cu is expected to show a comparable microstructure as SAC305 as the difference in Cu content is not expected to drastically affect the microstructure, especially in IMC formation.

References

[1] Y. L. Cheng, C. Y. Lee, Y. L. Huang, "Copper Metal for Semiconductor Interconnects", *Noble and Precious Metals – Properties, Nanoscale Effects and Applications*, 2018

[2] M. M. Hossain, F. Zahedi, D. Agonafer, P. Viswanadham, S. O. Dunford, "Reliability of Lead (Pb) Free SAC Solder Interconnects with Different PWB Surface Finishes Under Mechanical Loading", *Thermal and Thermomechanical Proceedings 10th Intersociety Conference on Phenomena in Electronics Systems, 2006. ITHERM 2006*, San Diego, CA, 2006, pp. 1038-1048

[3] Oxford Instruments, "Sample Preparation Techniques for EBSD Analysis (Electron Backscatter Diffraction)", 2013, [Online]. Available: https://www.azonano.com/article.aspx?ArticleID=3702

Chapter 2

Literature Review

Interlayer dielectric (ILD) cracking and delamination remains a concern in semiconductor devices, especially as silicon technology node continues to shrink aggressively. The combination of brittle extreme-low k (ELK) dielectrics, stiff copper pillars and lead-free tin-silver-copper solders increases the risks of this occurrence. A solution to mitigate this risk is to use a lower modulus solder. However, this may lead to the formation of brittle intermetallic compounds (IMCs) in the solder joints, compromising the overall reliability and performance of the devices. Thus, through electron backscatter diffraction (EBSD) analysis, a study on IMCs in solder joints can be done to aid in mitigating ILD crack and delamination risks.

2.1 Dielectric Materials

Dielectric materials play an important role in the function of microelectronic devices by electrically isolating conductive metal back end of line (BEOL) circuitry from one another. In recent years, extreme low-*k* (ELK) dielectrics have been implemented in leading edge silicon node devices to improve performances [1]. To attain such extreme-low dielectric constant, these ELK materials tend to be highly porous, which results in them being brittle with lower fracture strengths as compared to traditional dielectric materials [2]. When there is temperature fluctuation during reliability testing such as temperature or power cycling or even during field usage, thermal-mechanical stresses resulting from coefficient of thermal expansion (CTE) mismatch between the die and substrate develop in the solder joints. These stresses can also cause interlayer dielectric (ILD) cracking or delamination in brittle ELK dielectric materials as shown in Figure 2.1. ILD cracks and delamination are known to have caused electrical or functional failure of devices by forming shorts or leakage paths at the metal layers [3]. As such, it is of paramount importance that the risk of such ILD cracks and delamination are mitigated.

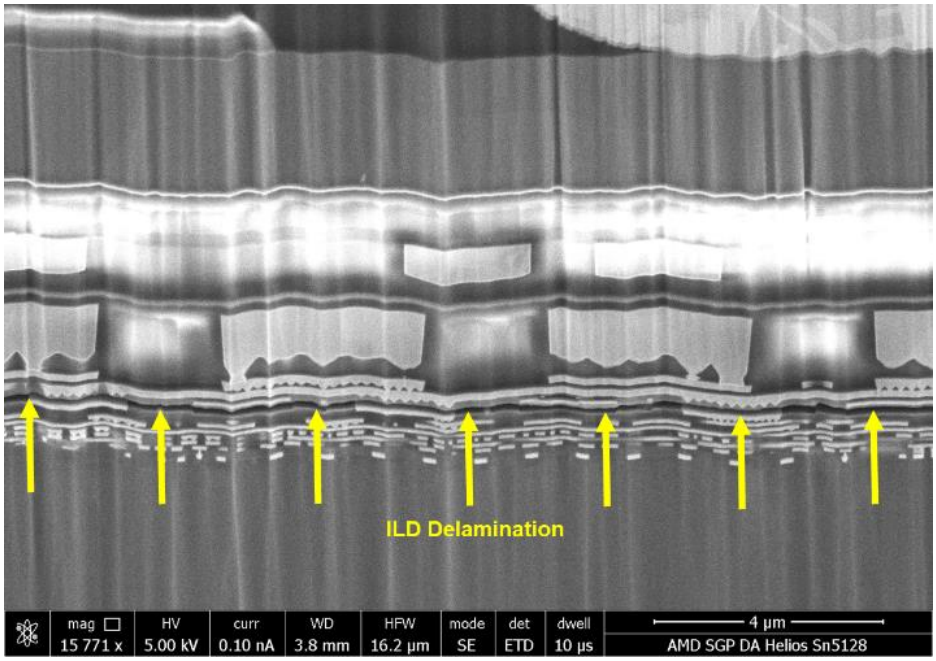

Figure 2.1: Cross section of sample with ILD delamination observed.

2.2 Thermal Cycling and Thermal-mechanical Stress

Reliability testing plays an important role in the development and implementation of microelectronic systems. Amongst the many different tests used to assess the reliability of microelectronic components, the most commonly employed test for characterizing interconnects is the thermal cycling (TC) test [4]. The goal of the TC test is to determine the ability of the interconnects like the copper-pillar solder bumps to withstand the rapid temperature fluctuations in an environment that mimics the real operating conditions. This test is designed so that the effects due to differences in CTE across materials are accelerated [5]. Due to this large CTE mismatch between the die and substrate, the thermal-mechanical stresses induced during thermal cycling becomes one of the contributing factors of ILD crack or delamination [6]. With the increase in power dissipation and the growing trend of decreasing chip sizes, thermal-mechanical stress-induced failures in interconnects are becoming a significant reliability problem.

Thermal-mechanical stress induced at the solder joints can be represented by the following equation:

$$\text{Stress} = \frac{F}{A} = -E\,\alpha\,dT \tag{2.1}$$

where E = Young's Modulus of solder joint

α = CTE

dT = temperature difference

From equation 2.1, it can be determined that the amount of stress induced on the solder joints is proportional to its Young's Modulus [7]. Therefore, to reduce the amount of thermal-mechanical stress induced and hence reduce the risk of ILD cracks and delamination, a possible solution is to use solder with a lower Young's Modulus.

Besides the induced thermal-mechanical stresses, studies have shown that the process of thermal cycling itself can influence the growth and microstructural evolution of the

intermetallic compounds (IMCs) in the solder joints [8]. During TC tests, it has been reported that the growth of IMCs is prevalent along the interconnects and the growth is mainly controlled by diffusion mechanisms which often do not follow Fick's diffusion law [9]. Growth of the IMCs can significantly affect the reliability of the solder joints. Solder joints observed after TC tests have been shown to have variations in their microstructures that can affect the deformation properties of the joint [10]. Therefore, to allow better anticipation and prediction of solder joints reliability, further examinations into the IMC growth and microstructure evolutions, such as the IMC thickness and crystal orientation, will be conducted.

Based on the JEDEC Standard, JESD22-A104-B, various TC test conditions are denoted across a range of different temperatures as shown in Table 2.1. Test condition G is one of such conditions used in the semiconductor industry.

Table 2.1: Thermal cycling test conditions based on JESD22-A104-B [5].

Test Condition	Nominal Ts(min) (°C) with tolerances	Nominal Ts(max) (°C) with tolerances
A	-55(+0, -10)	+85(10, -0)
B	-55(+0, -10)	+125(+15, -0)
C	-65(+0, -10)	+150(+15, -0)
G	-40(+0, -10)	+125(+15, -0)
H	-55(+0, -10)	+150(+15, -0)
I	-40(+0, -10)	+115(+15, -0)
J	-0(+0, -10)	+100(+15, -0)
K	-0(+0, -10)	+125(+15, -0)
L	-55(+0, -10)	+110(+15, -0)
M	-40(+0, -10)	+150(+15, -0)
S	-40(+0, -10)	+60(+15, -0)

2.3 Solder Joints and Intermetallic Compound Growth

Lead free tin-based solders have been used as interconnect joints for many years, with one of the most common being SAC305, where its composition consists of tin (Sn), 3% silver (Ag) and 0.5% copper (Cu). The presence of Ag in the solder increases the bulk solder modulus [11]. Therefore, an alternative solder with the absence of Ag would be expected to have a lower Young's modulus. A possible Ag-free candidate of lower Young's modulus would be Sn0.7Cu solder and it could be a potential alternative solder in mitigating ILD crack and delamination risks.

In copper pillar solder joints, Sn-based SAC305 solder is commonly used alongside Cu due to their excellent solderability properties. Interaction between the Cu and Sn-based solder will lead to the formation of IMCs at the Cu/Sn interface. The formation of Cu-Sn IMCs is one of the critical factors that significantly affect the reliability of the copper-pillar solder bumps [12]. Presence of a thin interfacial layer of Cu-Sn IMC is essential for promoting good wetting characteristics between the Sn and Cu [13]. However, if the IMC layer is too thick, the joint may weaken and result in mechanical failure in the operating environment, or during reliability tests such as thermal cycling. Due to the brittle nature of the IMCs, a weakened interfacial Cu-Sn IMC will potentially become a preferential crack initiation site, especially when the joint is subjected to thermal influences [14].

Interfacial Cu-Sn IMC layer grows in thickness over the course of its operational life. This growth of the IMC layer degrades the mechanical strength of the bumps. Initially, the interfacial IMC consists of mainly Cu_6Sn_5 phase when Sn-based solders are connected to the Cu pillars [15]. This formation of the Cu_6Sn_5 IMC is due to Cu and Sn atoms diffusing with one another under a concentration gradient [16]. Upon the introduction of a thermal gradient, such as heating during reflow, the diffusion of atoms accelerates and a Cu bi-metallic couple IMC will gradually result, with not only the growth of Cu_6Sn_5 phase but the formation of the Cu_3Sn phase as well [13]. Reflow typically takes place at elevated temperatures between $230^{O}C$ and $260^{O}C$. As observed from the phase diagram shown in Figure 2.2, Cu_6Sn_5 can exist as at least two different crystal structures, with hexagonal η-

Cu_6Sn_5 at temperatures above 186^{O}C and monoclinic η′-Cu_6Sn_5 at temperatures lower than 186^{O}C. IMCs formed at the bumps during reflow will mainly compose of scallop-shaped η-Cu_6Sn_5. As it cools to temperatures below 186^{O}C, there will be an allotropic transformation of the IMC from η-Cu_6Sn_5 to η'-Cu_6Sn_5 [17]. On the other hand, Cu_3Sn has an orthorhombic crystal structure as shown in Table 2.2.

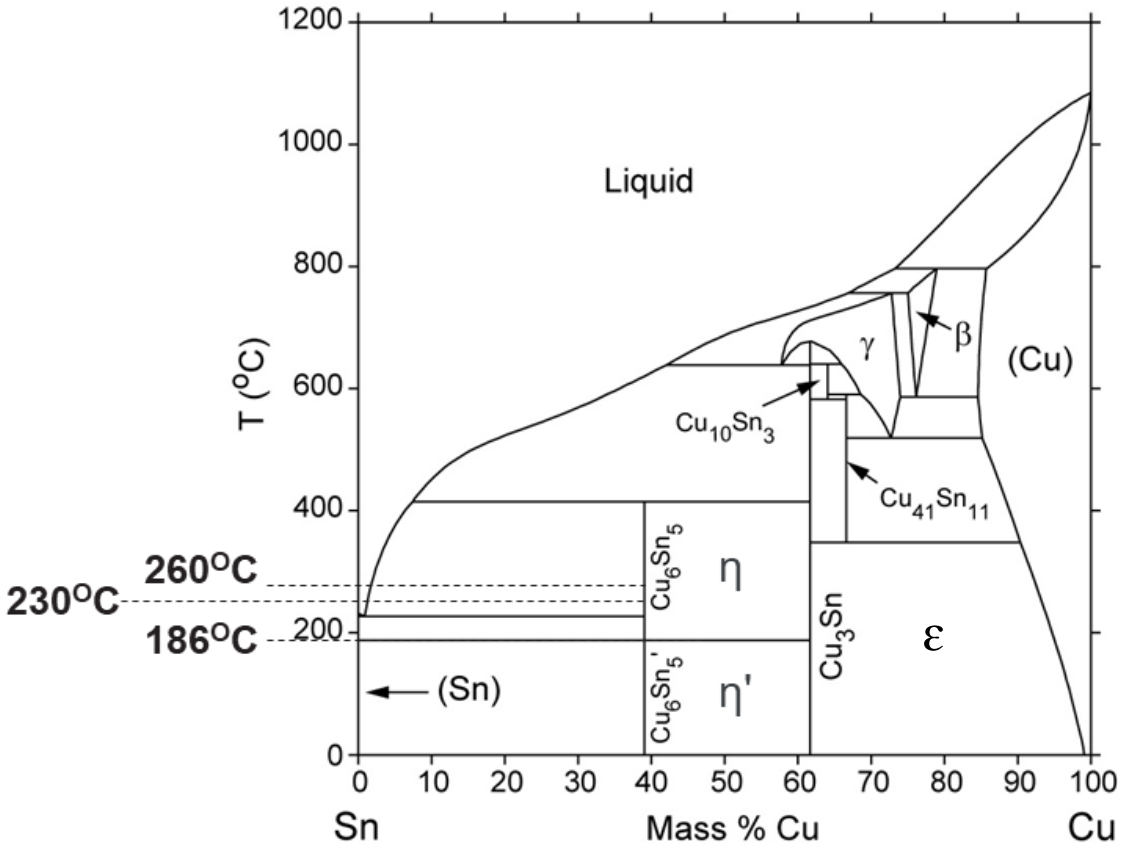

Figure 2.2: Phase diagram of binary Cu-Sn system [18].

Table 2.2: Crystal structures of intermetallic compounds η-Cu_6Sn_5, η'-Cu_6Sn_5 and Cu_3Sn [19-22].

Intermetallic Compound	Crystal Structure	Unit Cell Constants
η'-Cu_6Sn_5	Monoclinic Space group: C2/c	a=11.022Å b=7.282 Å c=9.827 Å β=98.84º
η-Cu_6Sn_5	Hexagonal Space group: $P6_3/mmc$	a= 4.19 Å c= 5.08 Å
Cu_3Sn	Orthorhombic Space group: Cmcm	a=5.618 Å b=4.367 Å c=4.835 Å

However, with the typical cooling rates after reflow, there is usually insufficient time for the transformation from η-Cu_6Sn_5 to η'-Cu_6Sn_5. The high temperature η-Cu_6Sn_5 remains as a metastable phase in the as-reflowed bump [17]. On the other hand, upon prolonged thermal influence, it could also result in cases where all solder in the interconnect is fully converted into IMC [23]. This phenomenon will become more apparent as interconnects shrink in size. An example would be in copper-pillar micro-bumps where the volume of Sn-based solder is much less as compared to a regular copper-pillar solder bump, as shown in Figure 2.3. As the IMCs are known to be very brittle, these conversion of solder into IMCs poses a potential reliability risk in the bumps, especially under elevated temperature conditions [15].

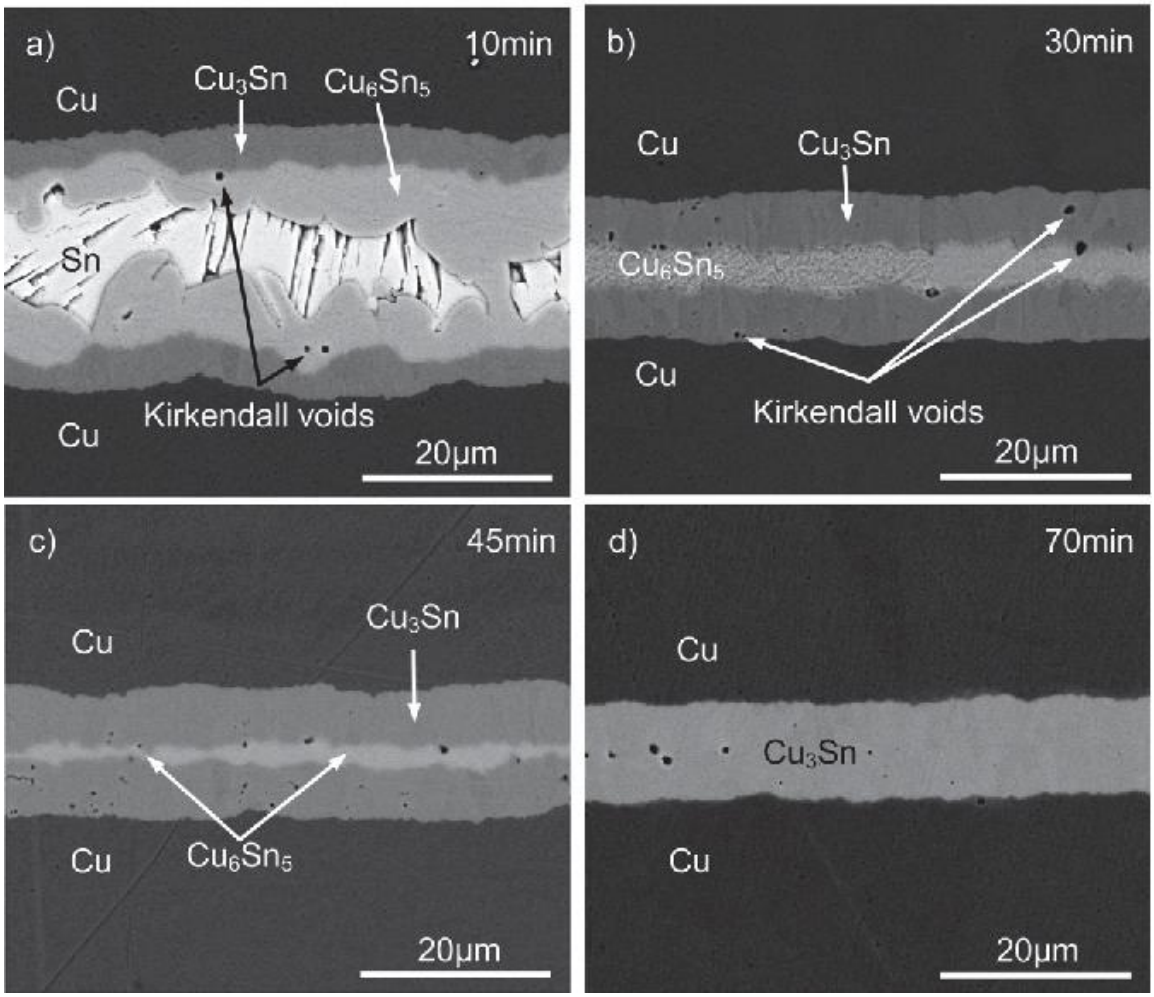

Figure 2.3: Cross-sectional SEM images of Cu/Sn/Cu micro-joints bonded at fixed elevated temperature for: (a) 10 min, (b) 30 min, (c) 45 min, and (d) 70 min [24].

In addition, it has also been reported that micro-voids, also known as Kirkendall voids, are able to form along the Cu_3Sn IMC interface as well as in the Cu_3Sn layer itself under elevated temperatures [13]. These Kirkendall voids are a damaging factor that tend to lead to the weakening of the interconnect joint and several studies have shown that these voids in Cu_3Sn have led to the degradation of solder joint reliability in board level tests [25-27]. As both Cu_6Sn_5 and Cu_3Sn IMCs encompass the characteristics of intrinsic brittleness and microporous enrichment, its growth will greatly affect the physical and mechanical properties of the copper-pillar solder bumps [13]. This may in turn degrade the long-term reliability of the bumps when the IMC layer grows too thick, promoting brittle failure at

the joint, as observed in Figure 2.4.

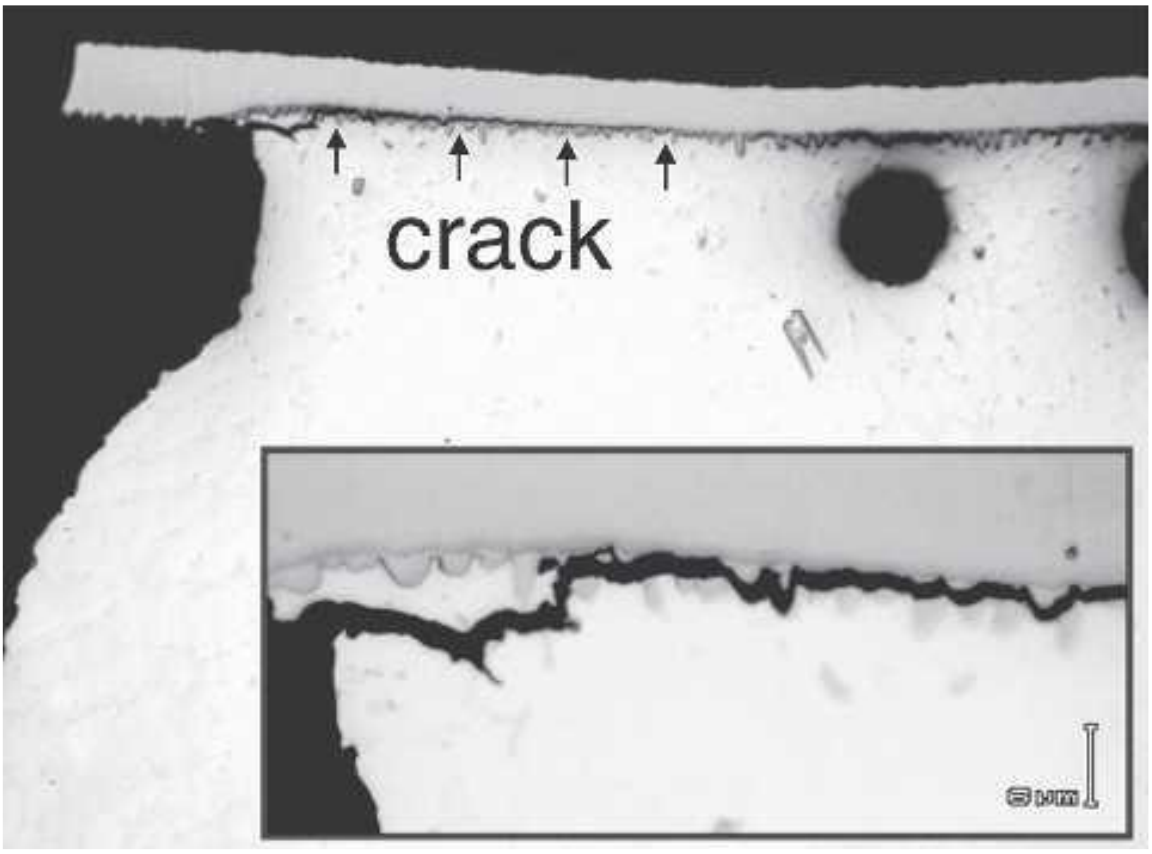

Figure 2.4: Brittle fracture through Cu_6Sn_5 IMC [27].

Therefore, although Sn0.7Cu solder is Ag-free and is expected to have a lower Young's modulus, it has a higher Cu content at 0.7% as compared to 0.5% in SAC305 solder. This higher Cu concentration fuels the concern of a thicker Cu-Sn IMC growth in the solder joints. Hence, to determine if Sn0.7Cu solder is a suitable alternative in mitigating ILD crack or delamination risk without compromising the joint integrity, there is a need to study the Sn0.7Cu solder joints to observe if there are excessive IMC growth as compared to SAC305 solder joints. This study would be possible with the use of the crystallographic analysis technique known as electron backscatter diffraction.

2.4 Electron Backscatter Diffraction

Electron backscatter diffraction (EBSD) is a scanning electron microscopy (SEM) based technique that provides crystallographic information about the microstructure of a sample [28]. A typical EBSD setup is shown in Figure 2.5. When a primary electron beam interacts with a tilted crystalline sample in the SEM, the accelerated primary electrons can be diffracted by various atomic layers in the sample. These diffracted electrons will generate lines known as Kikuchi bands or electron backscatter diffraction patterns (EBSPs) that are captured on a fluorescent phosphor screen in the detector [29]. EBSPs are characteristics of a crystal structure and orientation of the sample region where it is generated, effectively projecting the geometry of lattice planes. Together with a software and data base of crystallographic structure information, EBSPs can be indexed and information such as orientation measurements, microstructure characterization, phase and strain analysis can be determined [30].

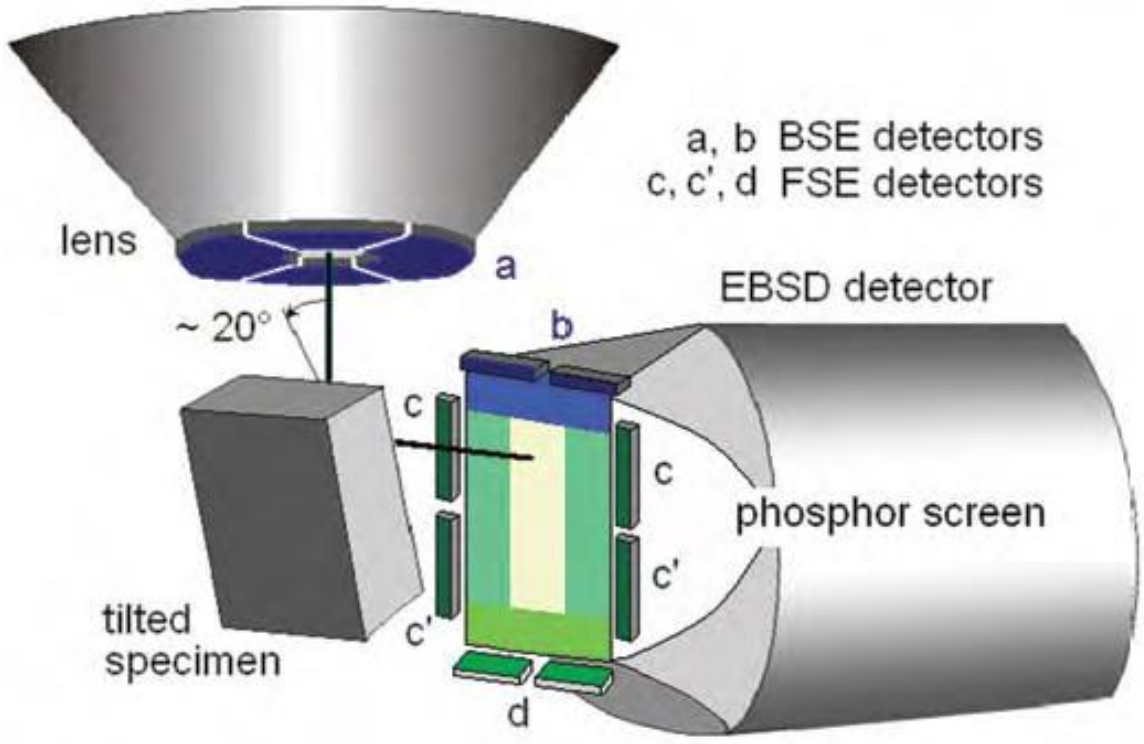

Figure 2.5: Typical setup of an EBSD system showing back-scattered electron (BSE) detectors, fore-scattered electron (FSE) detectors and phosphor screen in the EBSD detector [31].

2.4.1 Generating and Interpreting EBSD Diffraction Patterns

In the SEM, a primary electron beam of typically 15 to 20 keV interacts with a tilted sample, and a certain portion of these primary electrons will inelastically backscatter to form a divergent source of electrons near the sample surface. Subsequently, some of these electrons are diffracted at the lattice planes of the sample at angles that satisfy Bragg's Law [32] (see Figure 2.6), which is denoted by the equation:

$$2d \sin \theta = \lambda \tag{2.2}$$

where λ = wavelength of electrons

d = spacing of the diffracting plane

θ = angle of incidence of the electrons on the diffracting plane

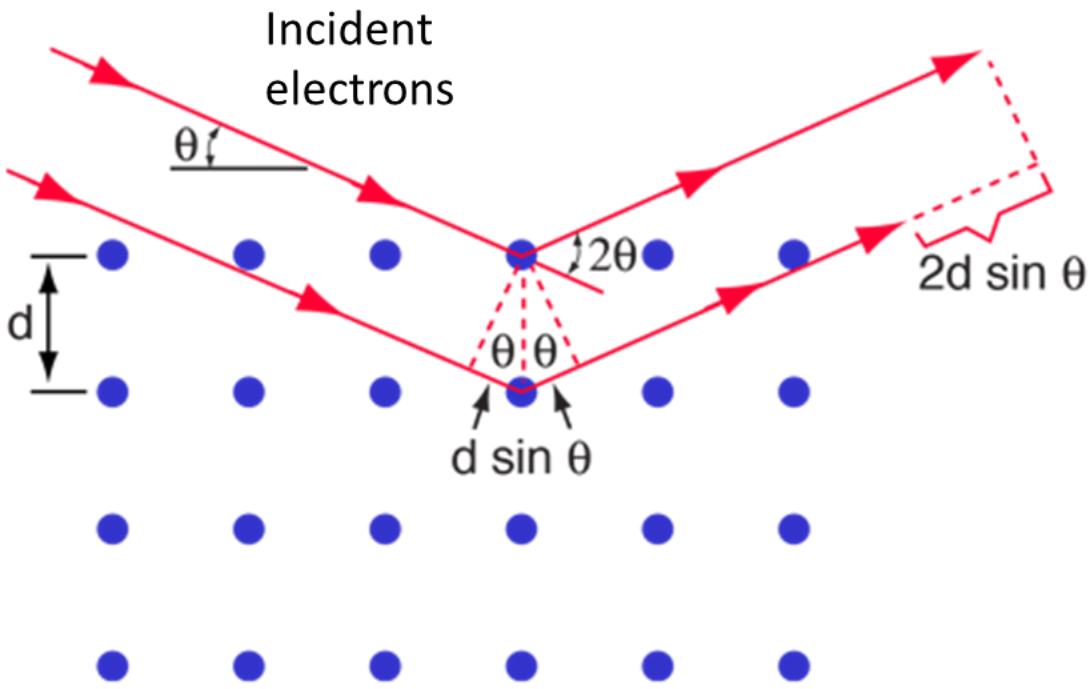

Figure 2.6: Incident electron on the crystal at an angle (θ) will produce coherent diffraction when difference in distance travelled ($2d\sin\theta$) equals to the wavelength (λ) [33].

These diffracted electrons form a coupled-set of large-angle cones, known as Kossel Cones, which corresponds to each diffracting plane. Kossel Cones are projected onto a fluorescent phosphor screen where an image containing the characteristic Kikuchi lines is produced [34]. The resulting Kikuchi pattern observed is in fact a gnomonic representation of the Kossel cones, as shown in Figure 2.7.

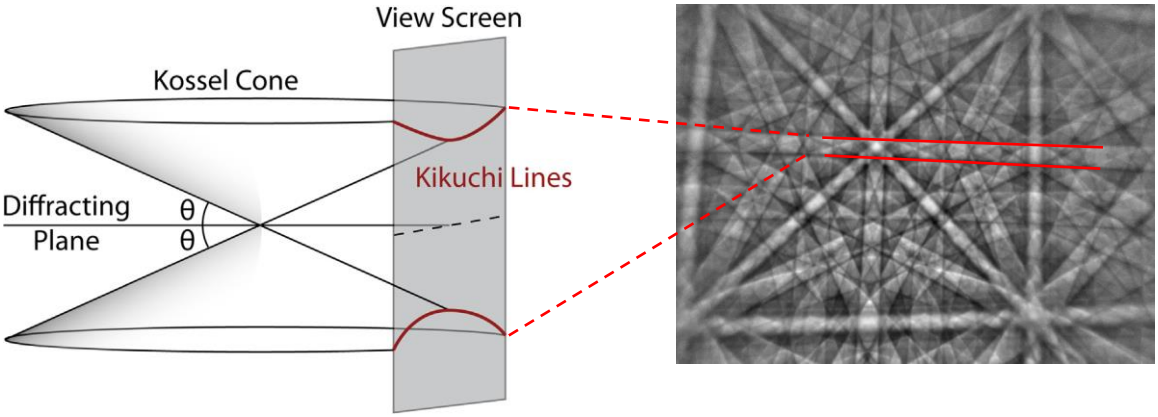

Figure 2.7: Kossel Cone and Kikuchi lines formation from a diffracting plane [34-35].

The center line within the Kikuchi bands reflect to where the diffracting planes intersect with the phosphor view screen. Therefore, it is possible for each Kikuchi band to be indexed by the Miller indices of the diffracting plane that forms the band. Intersections of Kikuchi bands in a highly diffracting zone will correspond to the zone axes in the crystal [36], as shown in Figure 2.8.

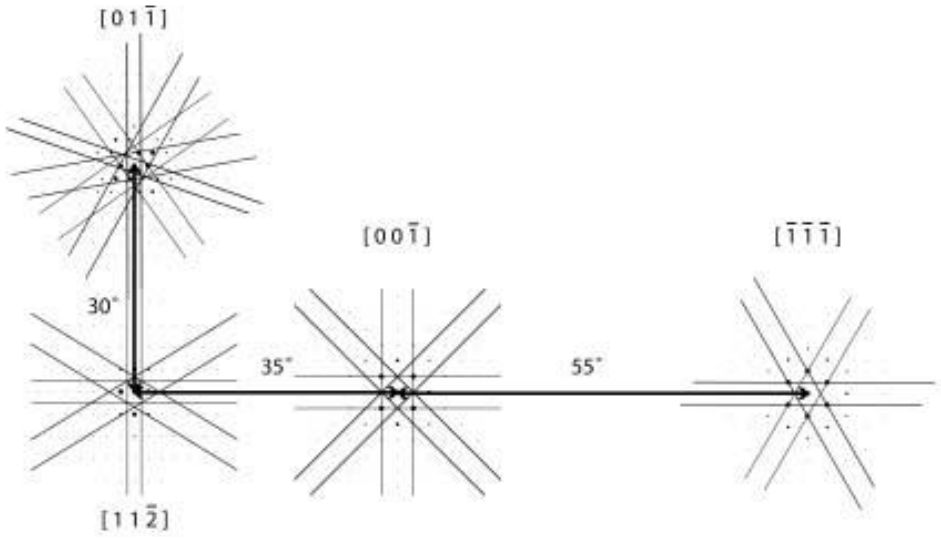

Figure 2.8: Zone axes and Kikuchi bands provide a roadmap of the crystal structure [36].

Lastly, the width of the Kikuchi bands that are close to the pattern center is given by the following equation:

$$w \approx 2l\theta = \frac{l\lambda}{d} \tag{2.3}$$

where w = width of Kikuchi band

l = distance of sample to screen

d = spacing of the diffracting plane

From equation 2.3, it can be observed that for planes with a wider *d,* the Kikuchi band width will be smaller. As diffraction pattern is determined by the crystal structure of the sample, the pattern will change according to the different crystal orientations. Hence, the positions of the Kikuchi bands can be used in calculating crystal orientations [37]. To facilitate the maximum number of backscattered electrons diffracting out of the sample surface, the sample is typically tilted at an angle of 70^{O} during analysis. This tilt will result in a sharp peak in backscattered electron energy distribution as shown in Figure 2.9. With a much well-defined energy of backscattered electrons, the subsequent resulting diffraction patterns generated will be much sharper [38].

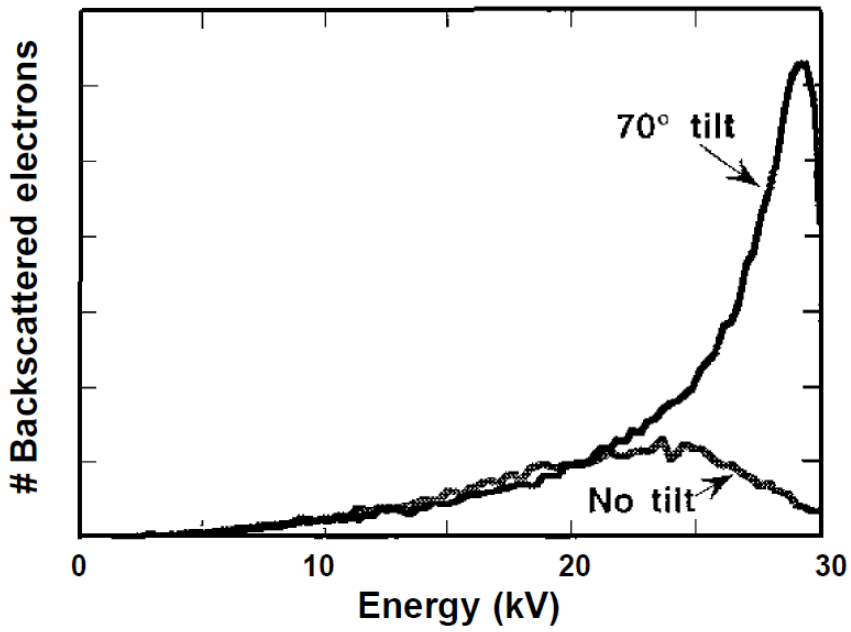

Figure 2.9: Effect of sample tilt on backscatter electron yield [38].

2.4.2 The Hough Transform

The Hough Transform determines the positions of the Kikuchi bands by converting the images taken from the EBSD camera in the *x*-*y* image space into a representation in the ρ-θ Hough space through the equation [39]:

$$\rho = x\cos\theta + y\sin\theta \tag{2.4}$$

where ρ = perpendicular distance from line to origin in *x*-*y* image space

θ = angle made with the x-axis in the *x*-*y* image space

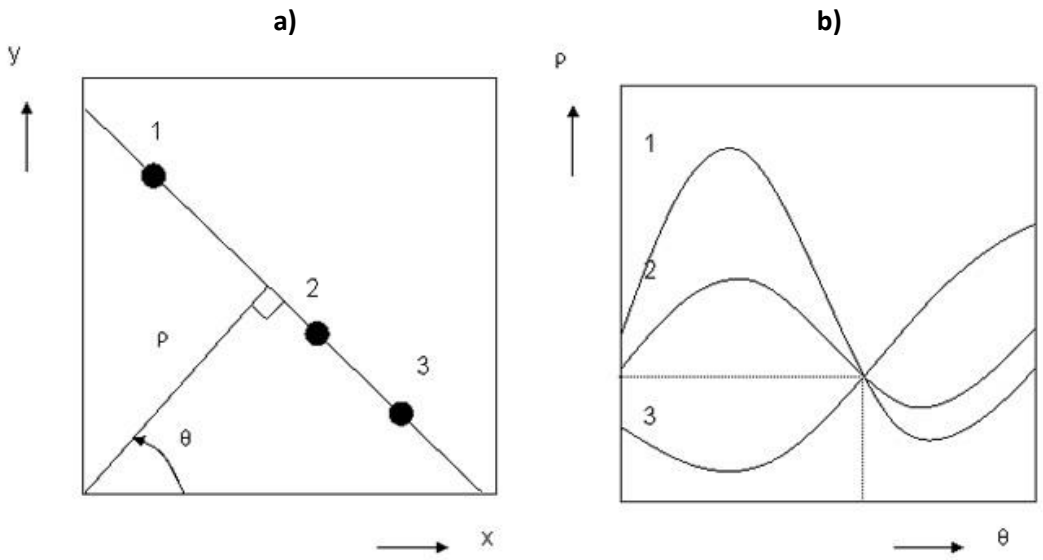

Figure 2.10: Hough transform of lines from (a) image space to points in (b) Hough space [39].

As observed in Figure 2.10, through the equation, a line in the image space can be converted and represented in the Hough space by a single point. In the Hough space, Kikuchi bands will appear as bright points or peaks which can be distinguished easily and used to determine the original band positions. This conversion can be observed in Figure 2.11.

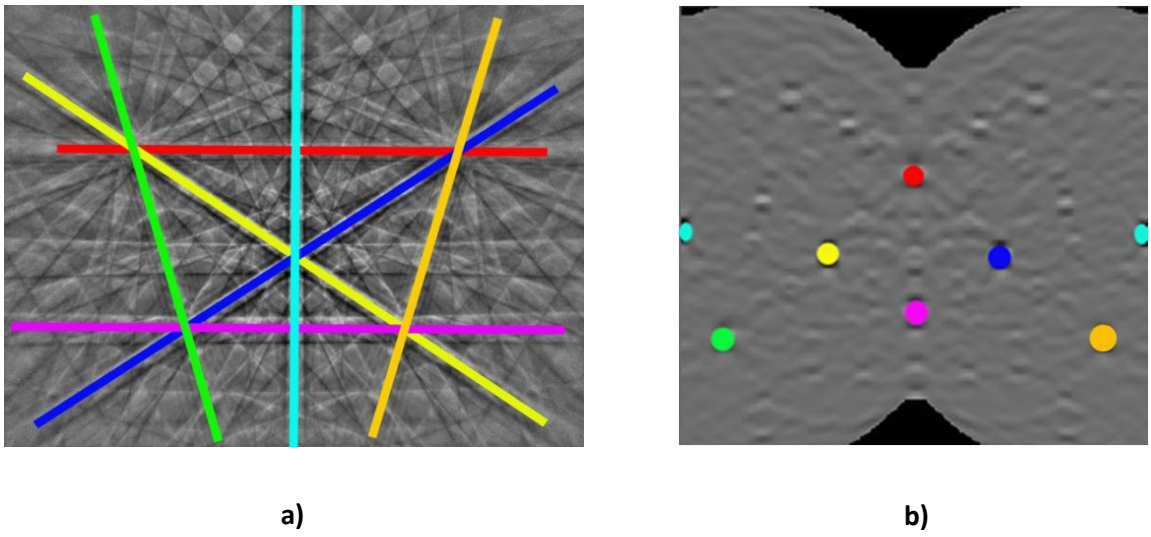

Figure 2.11: Kikuchi bands in the (a) original diffraction patterns corresponding to (b) bright peaks in the Hough space and colored similarly [39].

2.4.3 Diffraction Pattern Indexing

Modern EBSD systems have greatly improved in their indexing capabilities, making it possible for Kikuchi patterns to be automatically indexed. After a pattern is captured on the detector, a software is used to index the individual Kikuchi bands, where the Hough transformation algorithm is introduced to the Kikuchi pattern [40]. The Hough transform helps to identify the positions of the Kikuchi bands and after determining the locations of several bands, it is matched against various possible solutions to determine a best fit orientation matrix. A subsequent simulation of the pattern against a library database then confirms the orientation of the grains and the identity of the crystal structure, allowing various crystallographic information to be obtained for microstructure study [41].

Data acquired with EBSD can then be further processed to obtain information about the sample. Common examples of such information include grain size, grain boundaries, phase distribution and orientation data. By studying this information, links can be made to the sample regarding its performance properties or even the processing history of the materials [42].

2.4.4 Phase and Orientation Mapping

A valued application of EBSD is in obtaining data of the phase and crystal orientation. A phase map can display the spatial distribution of phases that are present in a sample and is useful in determining precipitates or IMC formation. Orientation data collected can be displayed as orientations maps in the form of either a phase map or as a series of inverse pole figure (IPF) maps.

Phase maps provide a representation of the different phases present in the sample while IPF maps assign colors to the measured crystal orientations based on the viewing direction, making visualization of preferred orientation easier [42]. Examples of phase and orientation maps can be observed in Figure 2.12.

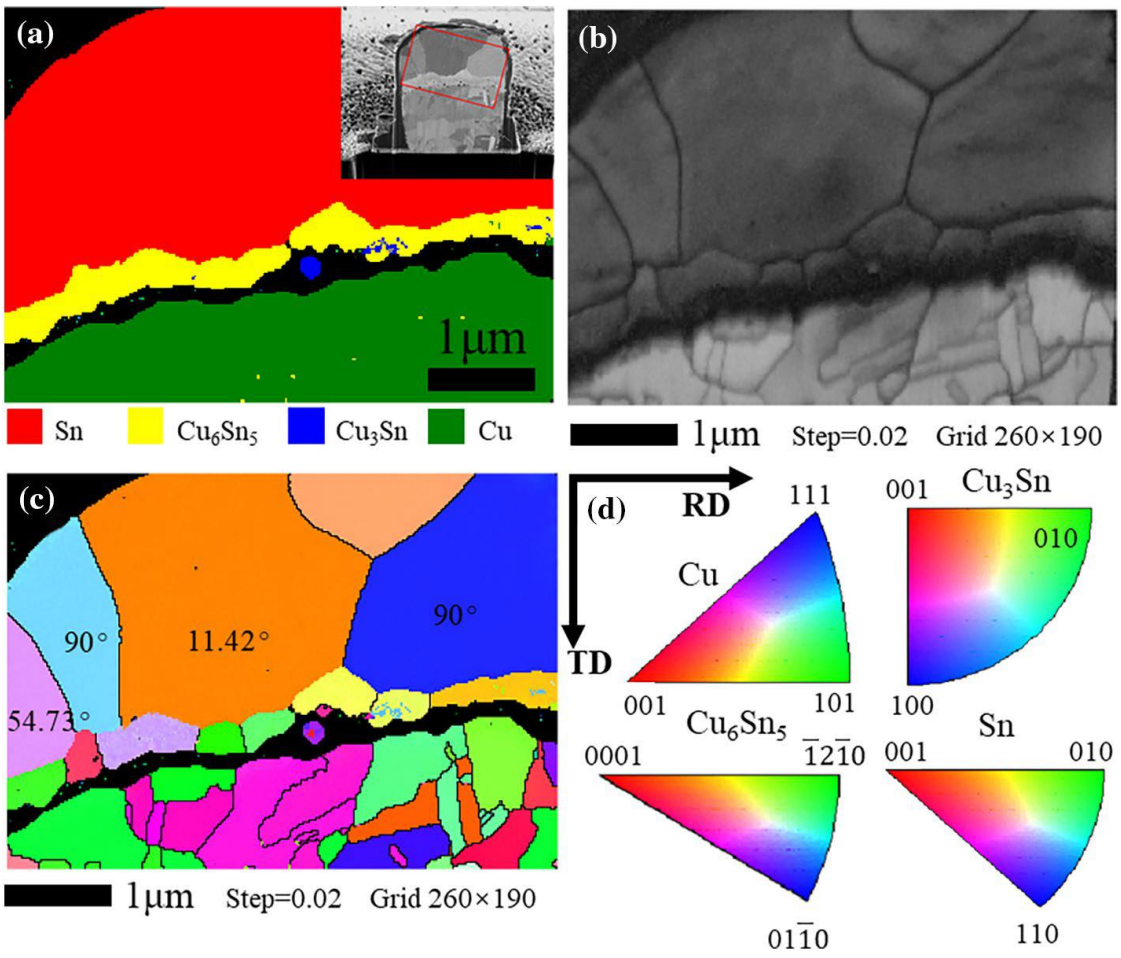

Figure 2.12: (a) Phase map of a sample cross section, (b) SEM image of the same sample and its (c) orientation map with corresponding (d) orientation triangle [43].

These maps will play a crucial role, especially in the analysis of the copper-pillar solder bumps. The phase map will be able to identify the phases that makes up the IMC in the bumps while the IPF maps will allow the study of the crystal orientations and to determine if there is any preferred orientation or texture in the microstructure. As EBSD is mainly a technique used in the study of crystallographic information, there are occasions where phase identification becomes inconclusive with the limited crystallographic information collected. Therefore, the combined use of EBSD and another technique known as energy dispersive X-ray (EDX) spectroscopy can be applied in order to uniquely identify every phase present [44]. This can be done by integrating the chemical information collected from EDX with the crystallographic information from EBSD.

2.5 Energy Dispersive X-ray Spectroscopy

Energy dispersive X-ray (EDX) spectroscopy is a complementary characterization technique to EBSD where it is used in determining the chemical composition of solid materials. EDX systems are also generally attached to an electron microscope, and it is based on the excitation of electrons and emission of characteristic X-rays from atoms [45]. A typical setup of the EDX is as shown in Figure 2.13.

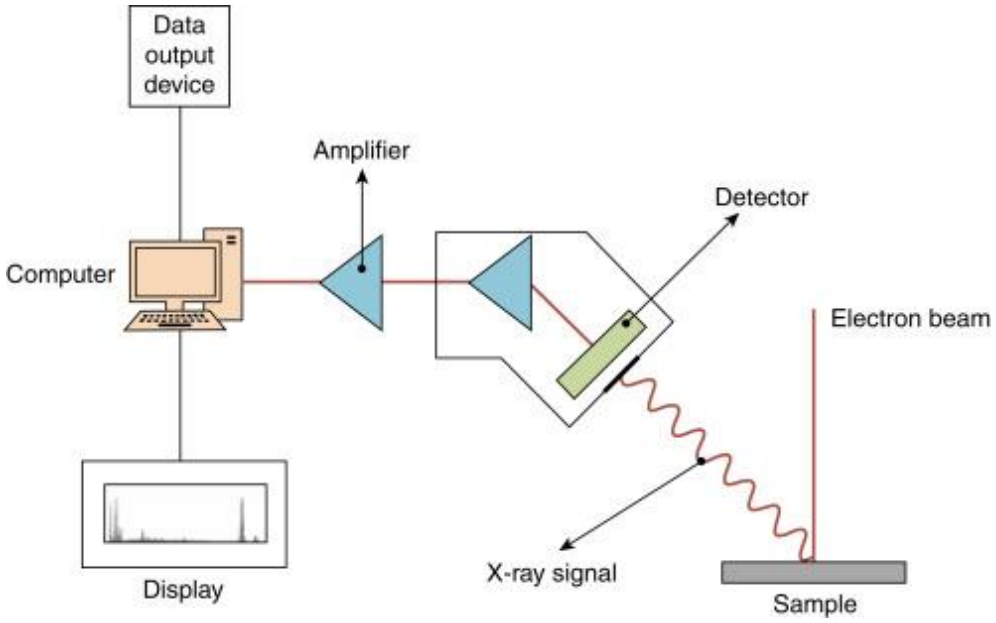

Figure 2.13: Energy dispersive X-ray spectroscopy setup [45].

A simplified process to explain EDX spectroscopy starts from an incident electron beam hitting the surface of a sample. This results in characteristic X-rays being emitted from the sample which are then collected by the detector. The X-ray signals are then converted and output through a software. As each element emits a unique set of X-ray frequencies, measuring these X-ray signals will be able to provide qualitative and quantitative information on the near-surface composition of the sample.

2.5.1 Characteristic X-ray

An electron's energy state in the quantum mechanical model of an atom is defined by the primary quantum number, *n*. *n* describes the electron's energy level and all sub-levels that share similar primary quantum number forms an energy 'shell'. These shells are labelled using alphabetical labels, where K shell represents $n = 1$, L shell has $n = 2$, M shell has $n = 3$ and so on. Increasing *n* corresponds with the increase in average distance from the nucleus and increase in energy [46]. Electron transitions between the energy shells abides to the law of energy conservation. The excitation of an electron to a higher energy state will require an external input of energy while the relaxation of an electron to a lower energy state will release energy into the environment. One of the most common methods of releasing energy out of an atom is through electromagnetic radiation [46].

When an incident electron beam interacts with a sample, the incoming incident electrons will interact with the core electrons inside the atom, transferring energy in the process. As shown in Figure 2.14, when an incoming electron of sufficient energy from the electron beam interacts with a core electron in the atom, the energy transferred from the incident electron to the core electrons will be sufficient to eject them from the atom. This ejected electron is subsequently known as a secondary electron. The removal of the core electron will also leave behind a vacancy that higher energy electrons in the atom can fill. As a higher energy electron begin filling the vacancy, it will release energy as it relaxes [47]. The energy is released in the form of X-rays.

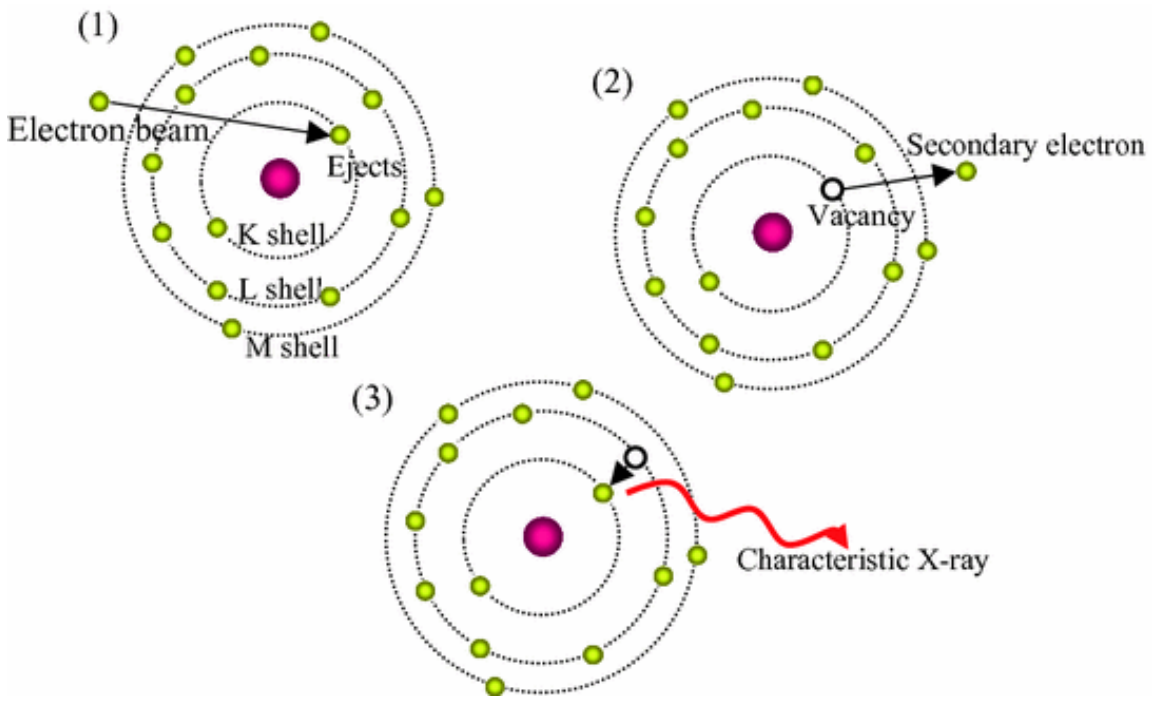

Figure 2.14: Electron beam interaction of an atom and the generating of secondary electrons and characteristic X-rays [46].

As each of the elements has a different nuclear charge, the energies of the core shells vary for each element. Therefore, with enough resolving power, the X-rays emitted from the energy transitions can be considered characteristic of each element and can be used to determine the composition of the sample [45]. Each characteristic X-ray peak of an element is usually presented in a spectrum with keV on the *x*-axis and peak intensity on the *y*-axis, as shown by an example in Figure 2.15.

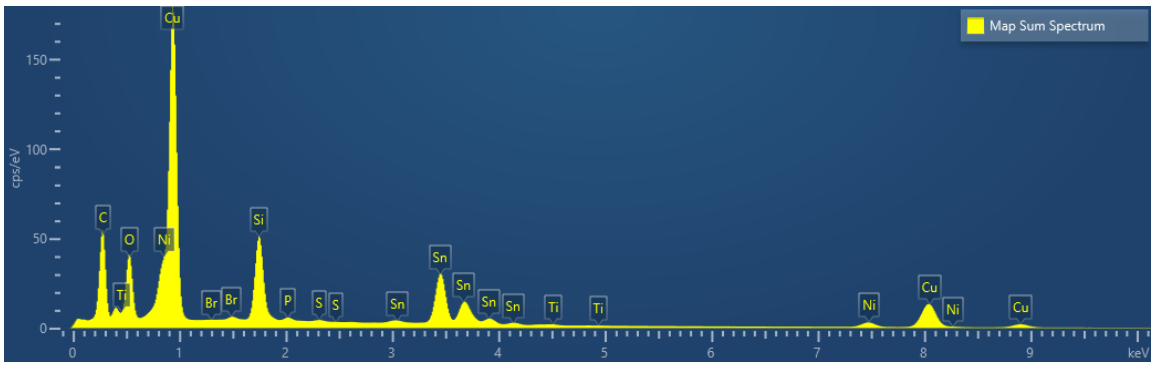

Figure 2.15: EDX spectra showing the characteristic X-ray peaks of various elements.

References

[1] V. Gupta, J. Zhao, D. Edwards, C. D. Mortensen, C. Heideman, D. C. Johnson, K. H. G. Lu, P. S. Ho, "Ultra Low-k Dielectric Mechanical Property Characterization", *2008 11th Intersociety Conference on Thermal and Thermomechanical Phenomena in Electronic Systems*, 2008, pp. 714-719

[2] S. Raghaven, I. Schmadlak, S. K. Sitaraman, "Interlayer Dielectric Cracking in Back End of Line (BEOL) Stack", *2012 IEEE 62nd Electronic Components and Technology Conference*, 2012, pp. 1467-1474

[3] R. L. Zelenka, "A Reliability Model for Interlayer Dielectric Cracking During Temperature Cycling", *29th Annual Proceedings Reliability Physics 1991*, 1991, pp. 30-34

[4] R. Ghaffarian, "Accelerated Thermal Cycling and Failure Mechanisms for BGA and CSP Assemblies", *Journal of Electronic Packaging*, 2000, Vol.122(4), pp. 335-340

[5] Innovative Circuits Engineering INC, "Temperature Cycling Testing (TC, Air to Air)", [Online]. Available: https://icenginc.com/temperature-cycle/

[6] H. V. Nguyen, C. Salm, J. Vroemen, J. Voets, B. Krabbenborg, J. Bisschop, A. J. Mouthaan, F. G. Kuper, "Fast Temperature Cycling and Electromigration Induced Thin Film Cracking in Multilevel Interconnection: Experiments and Modeling", *Microelectronics and Reliability*, 2002, Vol.42(9), pp.1415-1420

[7] I. Tolen, "How to Calculate Thermal Stress", 2020 [Online]. Available: https://sciencing.com/formulas-yield-stress-5434783.html

[8] X. Li, F. Li, "Effect of Thermal Cycling on interfacial IMCs Growth and Fracture Behaviour of SnAgCu/Cu Joints", *2009 International Conference on Electronic Packaging Technology & High-Density Packaging*, 2009, pp. 1144-1148

[9] J. K. Chen, J. E. Beraun, D. Y. Tzou, "A Dual-Phase-Lag Diffusion Model for Predicting Intermetallic Compound Layer Growth in Solder Joints", *Journal of Electronic Packaging*, 2001, Vol.123(1), pp. 52-57

[10] T. R. Bieler, H. Jiang, L. P. Lehman, T. Kirkpatrick, E. J. Cotts, B. Nandagopal, "Influence of Sn Grain Size and Orientation on the Thermomechanical Response and Reliability of Pb-free Solder Joints", *IEEE Transactions on Components and Packaging Technologies*, 2008, Vol.31(2), pp. 370-381

[11] R. Pandher, T. Lawlor, " Effect of Silver in Common Lead-free Alloys", 2009

[12] F. Hodaj, O. Liashenko, A. M. Gusak, "Cu_3Sn Suppression Criterion for Solid Copper/Molten Tin Reaction", *Philosophical Magazine Letters*, 2014, 94:4, pp. 217-224

[13] Y. C. Chan, A. C. K. So, J. K. L. Lai, "Growth Kinetics Studies of Cu-Sn Intermetallic Compound and its Effect on Shear Strength of LCCC SMT Solder Joints", *Materials Science and Engineering B, Solid-State Materials for Advanced Technology*, 1998, 55(1-2), pp. 5-13

[14] P. L. Tu, Y. C. Chan, J. K. L. Lai, "Effect of Intermetallic Compounds on the Thermal Fatigue of Surface Mount Solder Joints", *IEEE Transactions on Components, Packaging, and Manufacturing Technology: Part B*, 1997, 20(1), pp. 87-93

[15] M. P. C. Roma, S. Kudtarkar, O. Kierse, D. Sengupta, J. Cho, "Aging Studies of Cu-Sn Intermetallics in Cu Micropillars Used in Flip Chip Attachment onto Cu Lead Frames", *Journal of Electronic Materials*, 2018, Vol.47(2), pp. 1694-1704

[16] Z. Yin, F. Sun, M. Guo, "Effect of Sn/Cu Thickness Ratio on the Transformation Law of Cu6Sn5 to Cu3Sn in Sn/Cu Interface During Aging", *Materials Research Express*, 2018, Vol.5(8), pp. 86503

[17] K. Nogita, C. M. Gourlay, S. D. McDonald, Y. Q. Wu, J. Read, Q. F. Gu, "Kinetics of the η–η' Transformation in Cu_6Sn_5", *Scripta Materialia*, 2011, Vol.65(10), pp. 922-925

[18] NIST Material Measurement Laboratory, "Cu-Sn System", [Online]. Available: http://www.metallurgy.nist.gov/phase/solder/cusn.html

[19] X. Y. Pang, S. Q. Wang, L. Zhang, Z. Q Liu, J. K. Shang, "First Principles Calculation of Elastic and Lattice Constants of Orthorhombic Cu3Sn Crystal", *Journal of Alloys and Compounds*, 2008, Vol.466 (1-2), pp. 517-520

[20] C. Wieser, W. Hügel, A. Walnsch, A. Leineweber, "Two Two-Phase η′ + η Region in Cu6Sn5 Intermetallic: Insight into the Order–Disorder Transition from Diffusion Couples", *Journal of Electronic Materials*, 2020, Vol.49 (1), pp. 245-256

[21] H. Okamoto, "Phase Diagrams of Dilute Binary Alloys", *ASM International*, 2002, pp. 243

[22] A. Leineweber, C. Wieser, W. Hügel, "Cu6Sn5 Intermetallic: Reconciling Composition and Crystal Structure", *Scripta Materialia*, 2020, Vol.183, pp. 66-70

[23] J. Li, Y. Zhang, H. Zhang, Z. Chen, C. Zhuo, X. Liu, W. Zhu, "The Thermal Cycling Reliability of Copper Pillar Solder Bump in Flip Chip via Thermal Compression Bonding", *Microelectronics and Reliability*, 2020, Vol.104

[24] R. Zhang, Y. Tian, B. Liu, C. Hang, "Growth Mechanism of Cu-Sn Full IMC Joints on Polycrystalline and Single Crystal Cu Substrate", *14th International Conference on Electronic Packaging Technology*, 2013, pp. 1276-1279

[25] J. Yu, J. Kim, "Effects of Residual S on Kirkendall Void Formation at Cu/Sn-3.5Ag solder joints", *Acta Materialia*, 2009, Vol.56(19), pp. 5514-5523

[26] L. Xu, J. Pang, F. Che, "Impact of Thermal Cycling on Sn-Ag-Cu Solder Joints and Board-Level Reliability", *Journal of Electronic Materials*, 2008, Vol.37(6), pp. 880-886

[27] T. Mattila, J. Kivilahti, "Reliability of Lead-Free Interconnections Under Consecutive Thermal and Mechanical Loadings", *Journal of Electronic Materials*, 2006, Vol.35(2), pp. 250-256

[28] B. J. Inkson, "Scanning Electron Microscopy (SEM) and Transmission Electron Microscopy (TEM) for Materials Characterization", *Materials Characterization Using Nondestructive Evaluation (NDE) Methods*, 2016, pp. 17-43

[29] B. L. Adams, S. R. Kalidindi, D. T. Fullwood, "Electron Backscatter Diffraction Microscopy and Basic Stereology", *Microstructure Sensitive Design for Performance Optimization*, 2013, pp. 341-371

[30] G. Nolze, "Fundamentals and Applications of EBSD", *Method Coupling in Microanalysis*, 2015

[31] R. A. Schwarzer, J. Hjelen, "Backscattered Electron Imaging with an EBSD Detector", *Microscopy Today*, 2015, Vol.23(1), pp. 12-17

[32] M. A. Meyer, I. Zienert, E. Zschech, "Electron Backscatter Diffraction: Application to Cu Interconnects in top-View and Cross Section", *Materials for Information technology: Devices, Interconnects and Packaging,* 2005, pp. 485-495

[33] S. T. Thornton, A. Rex, "Modern Physics for Scientists and Engineers", *Saunders College Publishing,* 1993

[34] Oxford Instruments, "Pattern Formation", 2020 [Online]. Available: http://www.ebsd.com/ebsd-explained/10-ebsd-explained

[35] A. D. Herron, S. P. Coleman, K. Q. Dang, D. E. Spearot, E. R. Homer, "Simulation of Kinetic Kikuchi Diffraction Patterns form Atomistic Structures", *MethodsX,* 2018, Vol.5, pp. 1187-1203

[36] L. Karlsson, Z. Liliental-Weber, "Transmission Electron Microscopy of III-V Nanowires and Nanotrees", 2007

[37] Oxford Instruments, "Interpreting the Diffraction Pattern", 2020 [Online]. Available: http://www.ebsd.com/ebsd-explained/interpreting-the-diffraction-pattern

[38] J. R. Michael, "FIB Sample Preparation for EBSD: Is it Worth the Effort?", 2006, [Online]. Available: https://www.osti.gov/servlets/purl/1264285

[39] Oxford Instruments, "Basics of Automated Indexing", 2020 [Online]. Available: http://www.ebsd.com/ebsd-explained/basics-of-automated-indexing

[40] M. Claire, F. Roland, "A 3D Hough Transform for Indexing EBSD and Kossel Patterns", *Journal of Microscopy (Oxford),* Vol.230(3), pp. 520-529

[41] R. Schwarzer, "An Introduction to EBSD Backscatter Kikuchi Diffraction in the Oxford Instruments, "Interpreting the Diffraction Pattern", 2020 [Online]. Available: http://www.ebsd.com/ebsd-explained/interpreting-the-diffraction-pattern

[42] Oxford Instruments, "Microstructure Visualization in SEM", 2020 [Online]. Available: http://www.ebsd.com/solving-problems-with-ebsd/microstructure-visualization-in-sem#grain-size

[43] K. Chen, D. Wang, H. Ling, A. Hu, M. Li, W. Zhang, L. Cao, "Effects of Sn Grain Size on Intermetallic Compounds Formation in 5μm Diameter Cu/Sn Pillar Bumps", *Journal of Materials Science,* 2018, Vol.29(22), pp. 19484-19490

[44] C. L. Chen, R. C. Thomson, "The Combined Use of EBSD and EDX Analyses for the Identification of Complex Intermetallic Phases in Multicomponent Al-Si Piston Alloys", *Journal of Alloys and Compounds*, 2010, Vol.490(1), pp.293-300

[45] C. O. Colpan, Y. Nalbant, M. Ercelik, "Fundamentals of Fuel Cell Technologies", *Comprehensive Energy Systems*, 2018, Vol.4, pp. 1107-1130

[46] P. M. V. Raja, A. R. Barron, "An Introduction to Energy Dispersive X-ray Spectroscopy", *Physical Methods in Chemistry and Nano Science*, 2009, pp. ID55830

[47] B. Gaston, C. Protter, "Energy-Dispersive X-ray Spectroscopy (EDS)", *Introduction to Materials Characterization - CHM 412 Collaborative Text*, 2018-2019, pp. ID 142900

Chapter 3

Experimental Methodology

To study and compare the Cu-Sn IMC growth in the SAC305 and Sn0.7Cu solders, scanning electron microscopy (SEM), energy dispersive X-ray (EDX) spectroscopy and electron backscatter diffraction (EBSD) were employed. EDX is a characterization technique to determine the elemental composition of materials while EBSD provides crystallographic information about the sample. Two sets of samples were analyzed, each utilizing a different solder at the substrate side, namely SAC305 and Sn0.7Cu. Samples of each solder type are reliability tested separately under different temperature cycling and high temperature storage conditions. Subsequently, the samples are then prepared and analyzed.

3.1 Problem Statement

ILD crack and delamination continue to be of concern in the semiconductor industry. With the combined use of the brittle ELK dielectrics and stiff copper pillar solder joints, the risk of crack or delamination occurring increases, especially when there is a fluctuation in temperature, such as during reliability temperature cycling or during field usage. The thermal-mechanical stresses induced due to CTE mismatch between the die and substrate can result in ILD crack and delamination, ultimately causing the failure of the devices. It is therefore of interest to determine possible solutions to mitigate such crack and delamination risks.

As mentioned in Chapter 2 section 2.2, the thermal-mechanical stresses induced at the solder joints can be represented by equation 2.1, where the amount of stress induced on the solder joint is proportional to its Young's modulus. Therefore, to reduce the amount of stress exerted on the ILD and hence in turn reduce the risk of ILD crack and delamination, a possible solution is to use a more ductile solder with a lower Young's modulus. One of the most common lead-free tin-based solders in use as interconnect joints is SAC305, consisting of Sn – 3%, Ag – 0.5% and remaining Cu. The inclusion of Ag in the solder provides it with a good electrical and thermal conductivity as well as improving its mechanical strength. However, the presence of Ag in the solder also increases its bulk solder modulus [1]. As such, commercially available alternative Ag-free solders such as the binary Sn-Cu solders would be expected to have a lower Young's modulus. Among the Sn-*x*Cu solders, Sn0.7Cu is known to be one of the most promising in the area of electronics packaging, due to its low cost and high electrical conductivity [2].

Sn0.7Cu solder is Ag-free and consists of 0.7% Cu as opposed to 0.5% Cu, in SAC305 solder. Due to the higher Cu concentration in Sn0.7Cu solder, there is a concern of potentially thicker Cu-Sn IMC growth in the solder joints as a result. As mentioned in Chapter 2 section 2.3, presence of the Cu-Sn IMCs is essential in promoting good wetting between Sn and Cu. On the other hand, because of the brittle nature of the Cu-Sn IMCs, if the IMC layer is too thick, the solder joints may weaken and eventually result in mechanical

failure [3].

Therefore, to determine if Sn0.7Cu solder is a suitable alternative in mitigating ILD crack and delamination risks without compromising the solder joint integrity, there is a need to study and compare the Sn0.7Cu and SAC305 solder joints to observe if there are excessive IMC growth in Sn0.7Cu joints.

3.2 Experiment Samples

To determine if Sn0.7Cu solder would be a suitable alternative in mitigating ILD crack and delamination risks as compared to the conventional SAC305 solder, a comparison between the two solders will be made. Two sets of devices were prepared, each utilizing a different solder at the substrate side, namely SAC305 and Sn0.7Cu solders, as shown in Figure 3.1. The surface finish of the solder pads were electroless nickel-electroless palladium-immersion gold (ENEPIG). The solder cap at the copper pillar side for both sets of devices is SAC305 solder.

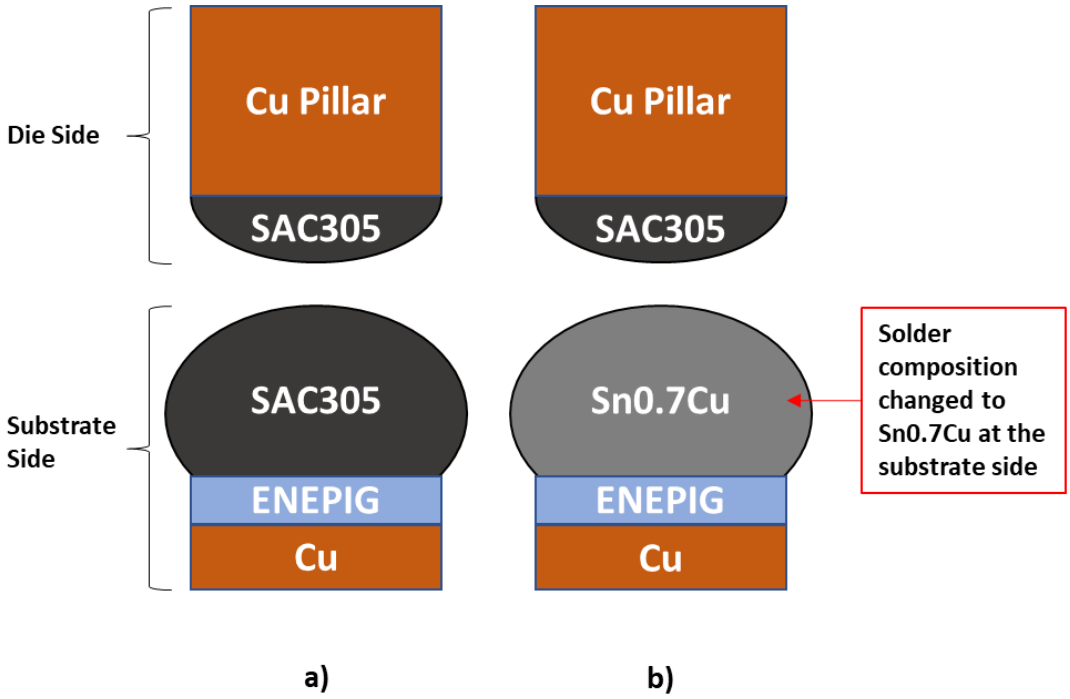

Figure 3.1: Schematic cross section of devices using a) SAC305 solder at the substrate side and b) Sn0.7Cu solder at the substrate side.

From literature, it is also known that IMC growth in solder bumps during reliability testing and field usage can ultimately affect the properties and hence the reliability of the solder bumps. Therefore, in addition to comparing SAC305 and Sn0.7Cu solder, the two sets of devices were also reliability tested under various conditions to study the IMC formation and growth. Samples of each solder type are reliability tested separately under temperature cycling – condition 'G' (TCG) and high temperature storage (HTS). As shown in Chapter 2, Table 2.1, TCG subjects the samples to a temperature range of -40(+0,-10) ^{O}C to +125(+15, -0) ^{O}C.

Under the TCG condition, two samples were prepared for each solder used. One sample was subjected to TCG conditions for an extended test point of 2000 cycles while the other sample was subjected to the TCG conditions for an intermediate test point of 1200 cycles. Together with a reference sample, the samples prepared under the two test points will allow a better understanding of the IMC growth trends, if any. Similarly, under the HTS conditions, two samples were also prepared for each solder. The first sample was subjected to HTS for an extended period of 2000 hours whereas the second sample was subjected to HTS for an intermediate period of 1000 hours. The temperature under HTS was kept at 125 ^{O}C.

For this study, the naming convention for each solder sample subjected to the various reliability test conditions are denoted in Table 3.1 for ease of identification.

Table 3.1: Sample naming convention.

	SAC305	**Sn0.7Cu**
Reference Sample	Sample 0	Sample Z
TCG 1200 Cycles	Sample 1	Sample A
TCG 2000 Cycles	Sample 2	Sample B
HTS 1000 Hours	Sample 3	Sample C
HTS 2000 Hours	Sample 4	Sample D

3.3 Sample Preparation Approaches

To study the Cu-Sn IMC growth in the solder bumps, Scanning Electron Microscopy (SEM), Energy Dispersive X-ray (EDX) Spectroscopy and Electron Backscatter Diffraction (EBSD) were employed. However, prior to EBSD analysis, the samples must undergo thorough preparation. Sample preparation for EBSD analysis is of utmost importance as diffracted electrons escape from within approximately a few nanometers of the sample surface. It is critical to ensure that the sample surface is devoid of any contamination, oxidization, or damage, to acquire useful EBSD data. Furthermore, as the sample is tilted at a high angle (typically 70 ^{O}) during EBSD analysis, it is also equally important to maintain the sample surface topography to a minimum. Generally, for simple SEM analysis, standard sample preparation techniques up to the final polishing stage will suffice. However, EBSD analysis has stricter requirements and furthermore, different materials may behave differently during sample preparation. Hence, the materials of interest should be prepared accordingly on a case-by-case basis. In this study, the samples will be prepared via a series of steps that involved cutting of the sample, mounting of the sample in epoxy resin as well as grinding and polishing of the sample.

3.4 Experimental Setup for EBSD Analysis

Although EBSD is able to provide crystallographic information on the IMC phases in the samples, identification of these IMCs will not be conclusive based on crystallographic information alone. To determine the chemical information of the IMCs, another characterization technique, energy dispersive X-ray (EDX) spectroscopy, was used as well. However, EDX used in isolation will be of little use due to the IMCs typically having similar chemical composition. Therefore, in order to accurately identify the various IMC phases, a combination of EDX and EBSD was used. By simultaneously acquiring the chemical information from EDX and the crystallographic information form EBSD, phase identification of the IMCs can be improved and made more accurate.

Prepared samples were first mounted onto a sample stub using silver conductive paint and the stub was placed on a hot plate heated to 120 °C for 5 minutes to allow the silver conductive paint to set. This silver paint would form a thin and highly conductive layer between the sample and stub, providing a conductive path that will reduce charging during analysis in the SEM. After the paint has set, the stub-mounted sample was then placed onto a 70 ° pre-tilt holder, secured and loaded into the Apreo SEM as shown in Figure 3.2. After adjusting the working distance to 10 mm and navigating the sample to the region of interest, the EBSD detector was then inserted. An accelerating voltage of 15 kV and beam current of 1.6 nA was used in the EBSD data acquisition. EBSD data were collected and analyzed through the AZtec software.

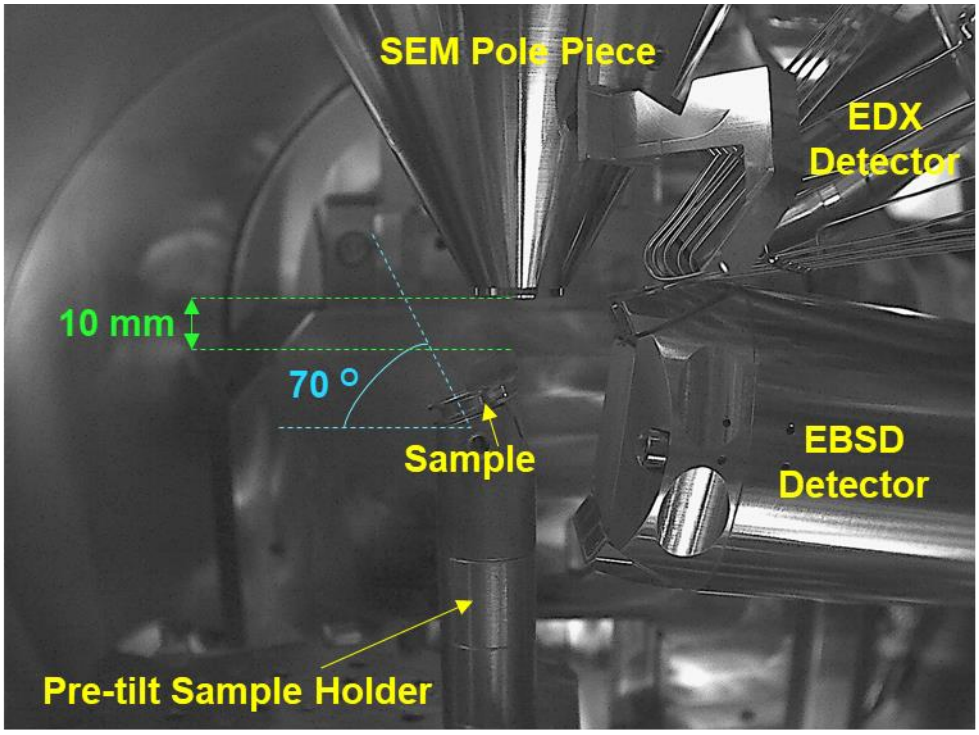

Figure 3.2: EBSD setup in Apreo SEM.

3.5 IMC Analysis

To determine if Sn0.7Cu would be suitable as an alternative to SAC305 in mitigating ILD crack and delamination risks, the IMC composition as well as the average IMC thickness of the samples were determined and compared. The crystal orientations of the IMC were also analyzed and compared to determine if there are any significant deviations from one another. The IMC composition and crystal orientation information were extracted from the EDX and EBSD data through the AZtecCrystal software.

As observed from literature, the interfacial IMC layers were mainly irregularly shaped. Therefore, the average equivalent thickness of the IMC layers in this study was calculated by dividing the total area of the IMC in the scan region by the length of the IMC layer in the same region, as given by the following equation and illustrated by Figure 3.3:

$$t_{Ave} = A / L \tag{3.1}$$

where t_{Ave} = average equivalent thickness of IMC

A = total area of IMC in scan region

L = length of IMC in scan region

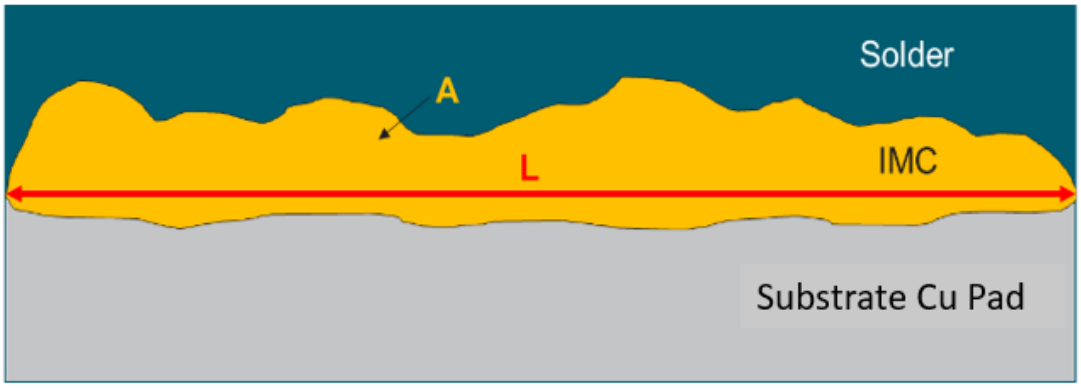

Figure 3.3: Close-up schematic cross section of copper pillar solder bump IMC region.

References

[1] R. Pandher, T. Lawlor, “Effect of Silver in Common Lead-free Alloys”, 2009

[2] Y. Lai, X. Hu, X. Jiang, Y. Li, “Effect of Ni Addition to Sn0.7Cu Solder Alloy on Thermal Behavior, Microstructure, and Mechanical Properties”, *Journal of Materials Engineering and Performance*, 2018, Vol.27(12), pp. 6564-6576

[3] P. L. Tu, Y. C. Chan, J. K. L. Lai, “Effect of Intermetallic Compounds on the Thermal Fatigue of Surface Mount Solder Joints”, *IEEE Transactions on Components, Packaging, and Manufacturing Technology: Part B*, 1997, Vol.20(1), pp. 87-93

Chapter 4

Sample Preparation

A customized sample preparation process flow was developed prior to EBSD analysis to ensure that the EBSD data collected were as accurate as possible. Several samples were prepared using different approaches to identify the best sample preparation process. To determine if the sample finish is the most suitable for EBSD analysis, the diffraction pattern quality and diffraction band detection of the samples were obtained and compared. Overall, mechanical polishing with diamond suspension followed by broad ion beam rotary stage polishing produced the best surface finish for EBSD analysis.

4.1 Sample Preparation Process

To study the Cu-Sn IMC growth in the solder bumps, Scanning Electron Microscopy (SEM), Energy Dispersive X-ray (EDX) Spectroscopy and Electron Backscatter Diffraction (EBSD) were employed. However, prior to EBSD analysis, the samples will have to first undergo thorough preparation. Sample preparation for EBSD analysis is of utmost importance as diffracted electrons escape from within approximately a few nanometers of the sample surface. It is critical to ensure that the sample surface is devoid of any contamination, oxidization, or damage, to acquire useful EBSD data. Furthermore, as the sample is tilted at a high angle (typically 70 ^{O}) during EBSD analysis, it is also equally important to maintain the sample surface topography to a minimum. Generally, for simple SEM analysis, standard sample preparation techniques up to the final polishing stage will suffice. However, EBSD analysis has stricter requirements and furthermore, different materials may behave differently during sample preparation. Hence, the materials of interest should be prepared accordingly on a case-by-case basis.

In this study, a customized sample preparation process flow that maximizes the formation of EBSD diffraction patterns at the bump IMC region was explored. A generic SAC305 solder bump sample that was not part of the study was used in the sample preparation process development. The sample were first prepared for EBSD analysis with a standard workflow. A standard workflow is generally described as a preparation process that mainly utilized mechanical cutting, grinding, and up to polishing to prepare samples for analysis. After which, a subsequent final step of ion beam polishing of the exposed cross-sectioned bump surface was performed. The surface finish of the cross-sectioned bumps was then evaluated via a quick observation of the diffraction patterns to determine if any useful data can be extracted. The 2-part sample preparation process can be observed as follows in Figure 4.1.

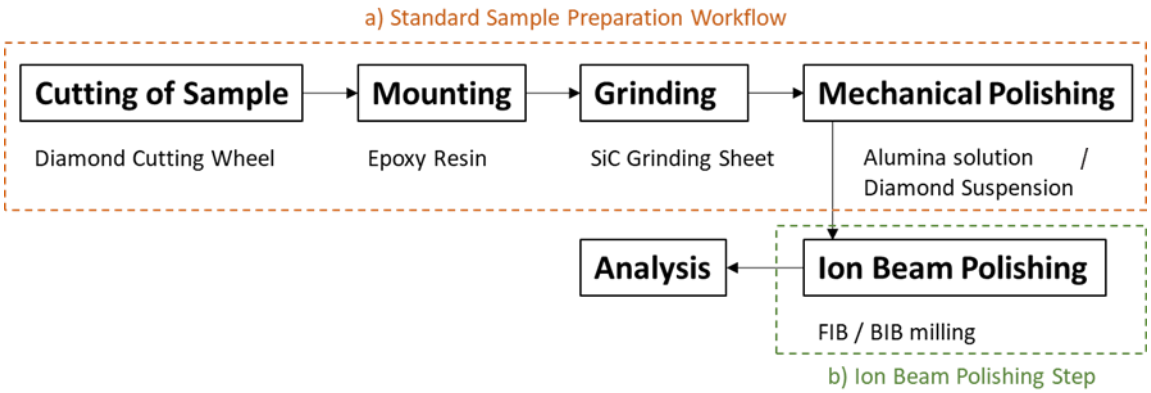

Figure 4.1: 2-part sample preparation process applying (a) standard workflow and (b) ion beam polishing.

4.2 Standard Sample Preparation

In preparation of the solder bump sample for EBSD analysis, the sample size was first reduced into a smaller sample of approximately 15 mm by 15 mm. This helped to facilitate the subsequent steps of sample preparation such as curing of epoxy during the mounting step as well as cross section grinding will be faster. At the same time, the sample remains sufficiently large enough to clamp during grinding and a decent array of solder bumps were still available for analysis.

It was crucial that the sample must not be damaged in the process, as any changes that occurred in the sample would lead to inaccurate results later. A common concern of sample damage is deformation due to excess heat during cutting. Cutting at extremely high speeds or the use of excessive force can cause the sample to overheat locally. This unwarranted heating may result in changes in the microstructure on the cut sample surface. Excess heat has been known to cause bigger grain sizes in the materials, resulting in a very different structure than the original [1]. The deformation may be so severe that it extends from the surface, to deep inside the bulk material that subsequent grinding and polishing cannot remove. EBSD analysis is especially sensitive to such damages, and therefore it is important to avoid overheating and compromising the sample.

In this study, to prevent overheating of the sample, the Struers Minitom precision cutter, as shown in Figure 4.2, was used to cut the sample. The Minitom is a low speed, automatic precision cutting machine designed for cutting samples that are sensitive to heat generated by high-speed cutting. Together with its micrometer screw gauge, it allows the sample to be cut as close as possible to the surface of interest, up to an accuracy of +0.01 mm, while minimizing the risk of damage to the sample due to heating.

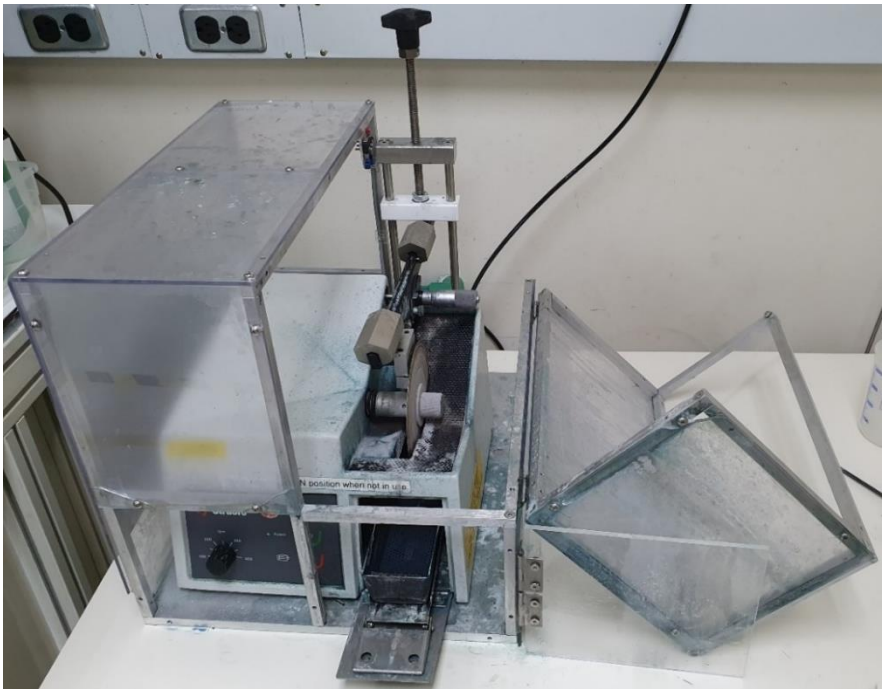

Figure 4.2: Struers Minitom Precision Cutter with customized safety casing.

After the sample was cut, mounting was done using Allied EpoxyBond 110. As shown in Figure 4.3, this is a two-part (resin and hardener) epoxy resin. Upon low temperature curing, this epoxy resin will become chemically resistant to etchants. It will also not outgas under vacuum, which makes it suitable for EBSD analysis given that the mounted sample will be analyzed under vacuum in an SEM.

Figure 4.3: Allied EpoxyBond 110 set.

Mounting of the sample started with the sample placed in a mold. The two-part epoxy resin was then mixed in a mixing cup in the ratio of 10:1 for Part A (resin) and Part B (hardener) respectively, until the two liquids became homogeneous in color, after which the mixture was poured over the sample in the mold until the sample was fully submerged. The epoxy mixture was left to cure over a hotplate at a temperature of 100^{O}C for 10 minutes. As shown in Figure 4.4, marking the endpoint of curing, the fully cured epoxy resin would be visibly noticed by its brick-red color, a unique feature of the EpoxyBond 110.

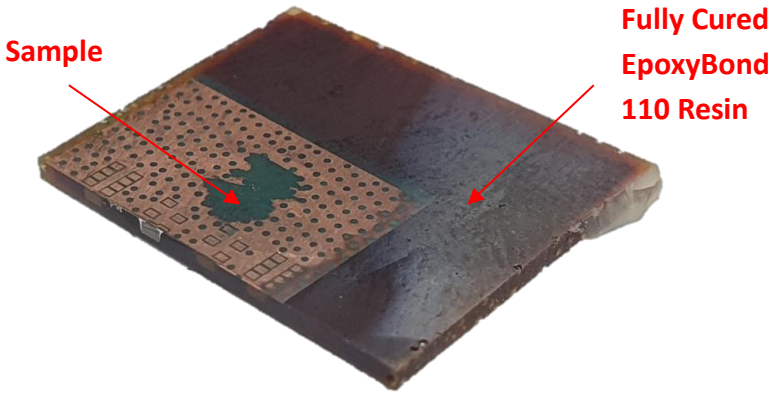

Figure 4.4: Sample mounted in fully cured EpoxyBond 110 resin.

After the sample has been securely mounted in epoxy resin, cross-sectional grinding was performed to expose the solder bumps. Grinding also removes any damage introduced during cutting and should introduce less damage than the original cutting step, ultimately levelling the sample surface. For the grinding setup, the sample was mounted onto a customized jig, as shown in Figure 4.5. The customized jig was specially designed by AMD, for the purpose of cross section grinding of samples. Risks of uneven sample surface due to hand grinding are reduced with the use of the customized jig, as the clamped sample would always be perpendicular to the grinding surface. In addition, a weight on the customized jig also ensured that a constant force was exerted on the sample during grinding, reducing the risk of sample overheating due to excessive force employed by hand.

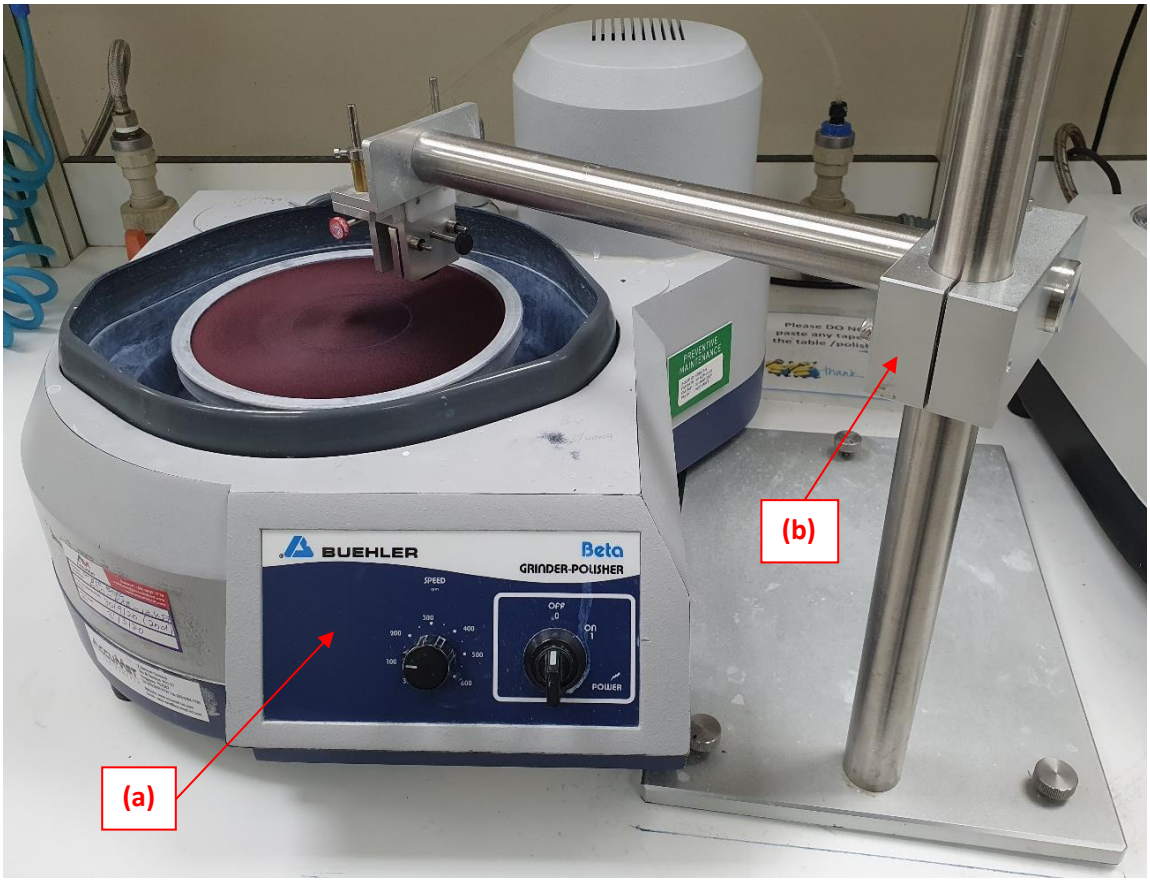

Figure 4.5: Sample grinding setup with (a) Buehler Beta Grinder-polisher tool and (b) customized cross section jig.

With the sample securely clamped onto the jig, the sample was cross sectionally grinded using the Buehler Beta Grinder-polisher tool and Allied SiC grinding paper. Several grits of paper were used in this sample preparation and because the SiC grinding paper blunts very quickly as well, it was replaced frequently to maintain efficient removal of material and to preserve the sample surface. Grinding with a blunt paper might result in surface damage to the sample such as smearing and localized heating.

600 grit (P-1200) grinding paper was first used to remove any damage resulting from the cutting step. Each grinding paper used was replaced every 2 minutes of grinding at a speed of 250 rpm to ensure that the sample was continuously grinded with a sharp abrasive surface. The sample was periodically inspected under a light microscope to ensure that damage from the cutting stage was removed. Subsequently, finer grit paper was used progressively from 800 grit (P-2400) to finally 1200 grit (P-4000) for fine grinding. Similarly, during each stage of paper grit used, the sample was inspected periodically under light microscope to ensure that damages from the previous grinding grit was completely removed.

At times, even after fine grinding with 1200 grit paper, the sample surface would still be left with deformation and fine scratches. Hence, to reduce the chance of this occurrence, the sample was further mechanically polished. Mechanical polishing has a similar action to grinding and was performed using the same Buehler Beta Grinder-polisher tool, except that the polishing medium holding the abrasive was now a polishing cloth with more shock absorbing capability than the SiC grinding papers. The shock absorbing characteristics of the polishing cloth would allow for a gentler removal of material from the sample surface, greatly reducing the associated damages.

For mechanical polishing, generally two common types of polishing suspensions used were alumina and diamond polishing suspensions. In this study, to observe each of their effects on the final surface finish of the sample, two polishing suspensions, 0.05 μm alumina suspension and 0.05 μm diamond suspension were experimented with. Samples were polished using each of the suspension for 1 minute.

4.2.1 Standard Sample Preparation Surface Finish

During the grinding process, periodic inspection of the surface finish was done under a light microscope. It can be observed from Figure 4.6 that as sample grinding progressed from 600 grit to finer 1200 grit, scratches on the surfaces were gradually removed. However, deformation such as fine scratches still remained on the surface even after grinding to the finest abrasive size. Such surface finish was not optimal for EBSD analysis. Thus, to ensure that damages induced during this grinding stage was removed as well, further mechanical polishing was necessary.

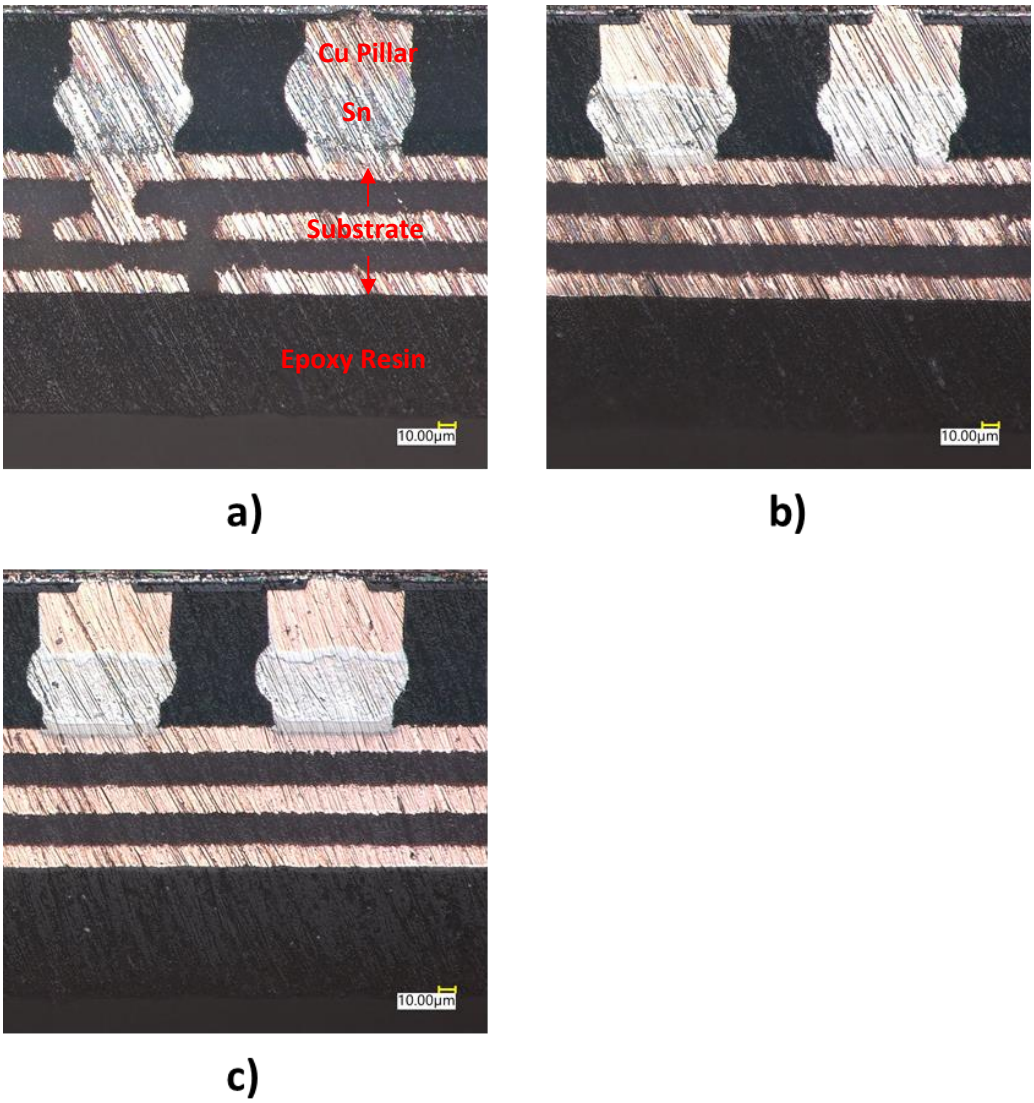

Figure 4.6: Surface finish of sample observed under light microscope at 500x magnification, after (a) 600 grit, (b) 800 grit and (c) 1200 grit grinding.

After fine grinding at 1200 grit, samples were separately polished using 0.05 μm alumina suspension and 0.05 μm diamond suspension. The resulting surface finish after polishing by each of the suspension can be observed from the optical light microscope images as shown in Figure 4.7. It can be observed that both resulting surface finishes have improved, with significantly reduced artifacts on the surfaces as compared to the previously grinded surfaces. However, upon comparing the two polished surfaces, the surface finish after the alumina suspension polishing still retains very prominent deep scratches on the surface, whereas most deep scratches were observed to be removed after diamond suspension polishing. This is to be expected since diamond is a harder material as compared to alumina and hence able to achieve a more efficient removal of material for same duration of polish.

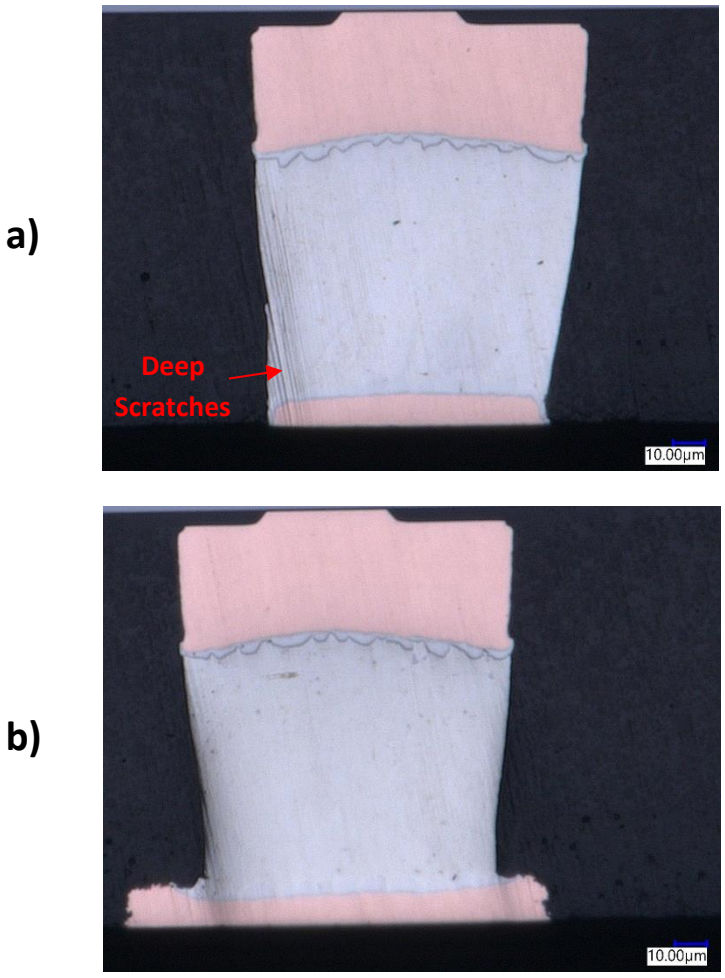

Figure 4.7: Surface finish of sample observed under light microscope at 700x magnification, after (a) 0.05 μm alumina suspension and (b) 0.05 μm diamond suspension.

Subsequently, the grinded and polished samples were analyzed under a Thermo Fisher Scientific Apreo SEM and inspected using the UltimMax100 EDX and Symmetry EBSD system from Oxford Instruments (see Figure 4.8).

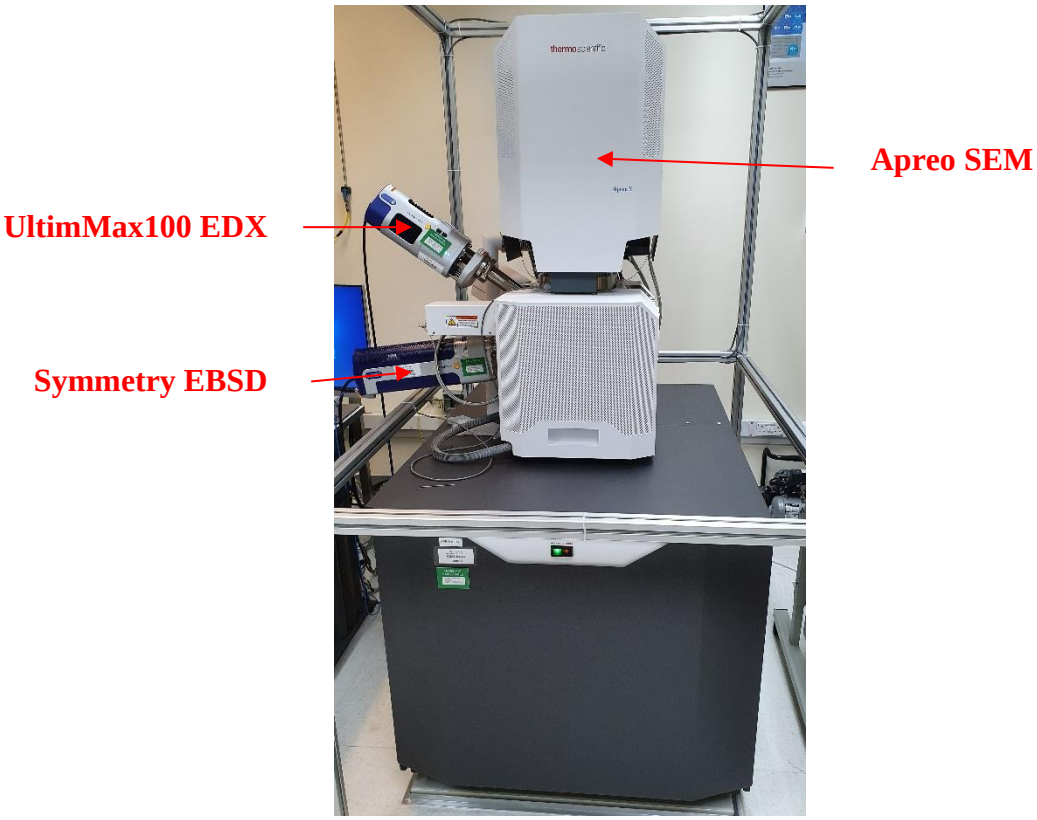

Figure 4.8: Thermo Fisher Scientific Apreo SEM and Oxford Instruments EDX/EBSD setup.

The goal of EBSD sample preparation is always to produce a deformation free surface that maximizes the EBSD pattern quality from the entire sample surface. A quick indication to determine if a sample has been sufficiently prepared and is suitable for EBSD analysis, was to visually compare the EBSD diffraction patterns generated. A sample surface with the optimal condition for EBSD analysis would generally be one that generates a diffraction pattern with the best contrast against the background signal. A faint or noisy pattern cannot be analyzed, and no useful crystallographic information can be obtained from it. However, visual observation tends to be subjective, and the quality of patterns will vary depending on each analyst.

Using Oxford Instrument's AZTec software, the diffraction pattern quality can be quantified by comparing the number of diffraction bands the measured pattern can match against a calculated pattern in the software's library. The software calibration was performed using cobalt (Co) and Manganese (Mn) as the standard for system gain and detector resolution respectively. A maximum of 12 diffraction bands can be identified using the AZTec software. The more diffraction bands that can be matched, the better the sample surface is for EBSD analysis. Another parameter that can be used to quickly quantify the surface finish is the mean angular deviation (MAD) values. The MAD values indicate the misfit between the measured and calculated angles between two bands. Hence the larger the MAD value, the larger the misfit and overall indexing confidence will be lowered. Typically, MAD values that are less than 0.6 are considered acceptable for EBSD analysis. Diffraction patterns from various stages of sample preparation was obtained. At each preparation stage, diffraction patterns were observed at several regions of the sample. To observe and evaluate the results of the various grinding and polishing stages, the EBSD diffraction patterns, average band detection values and average MAD values were acquired after each stage. EBSD diffraction patterns were obtained at a 622 x 512 pixels resolution. The average band detection and MAD values were determined from 10 random measurement points with about 2 μm spacing in between the points and averaging out the values.

Results of the various grinding and polishing stages on the diffraction patten quality are shown in Figure 4.9. Based on visual inspection, it was observed that grinding up to 1200 grit SiC paper produced very weak patterns. However, as further polishing was done with 0.05 μm alumina and 0.05 μm diamond suspension, the diffraction pattern quality was observed to have increased significantly. Through the visual observations, the diffraction pattern quality after the 1200 grit SiC grinding stage was deemed unsuitable for EBSD analysis as the patterns were barely visible for analysis. In contrast, diffraction patterns were more visible after polishing with 0.05 μm alumina suspension and 0.05 μm diamond suspension. However, between alumina and diamond suspension, the surface finish after polishing with diamond suspension produced a clearer diffraction pattern with better contrast as compared to alumina suspension.

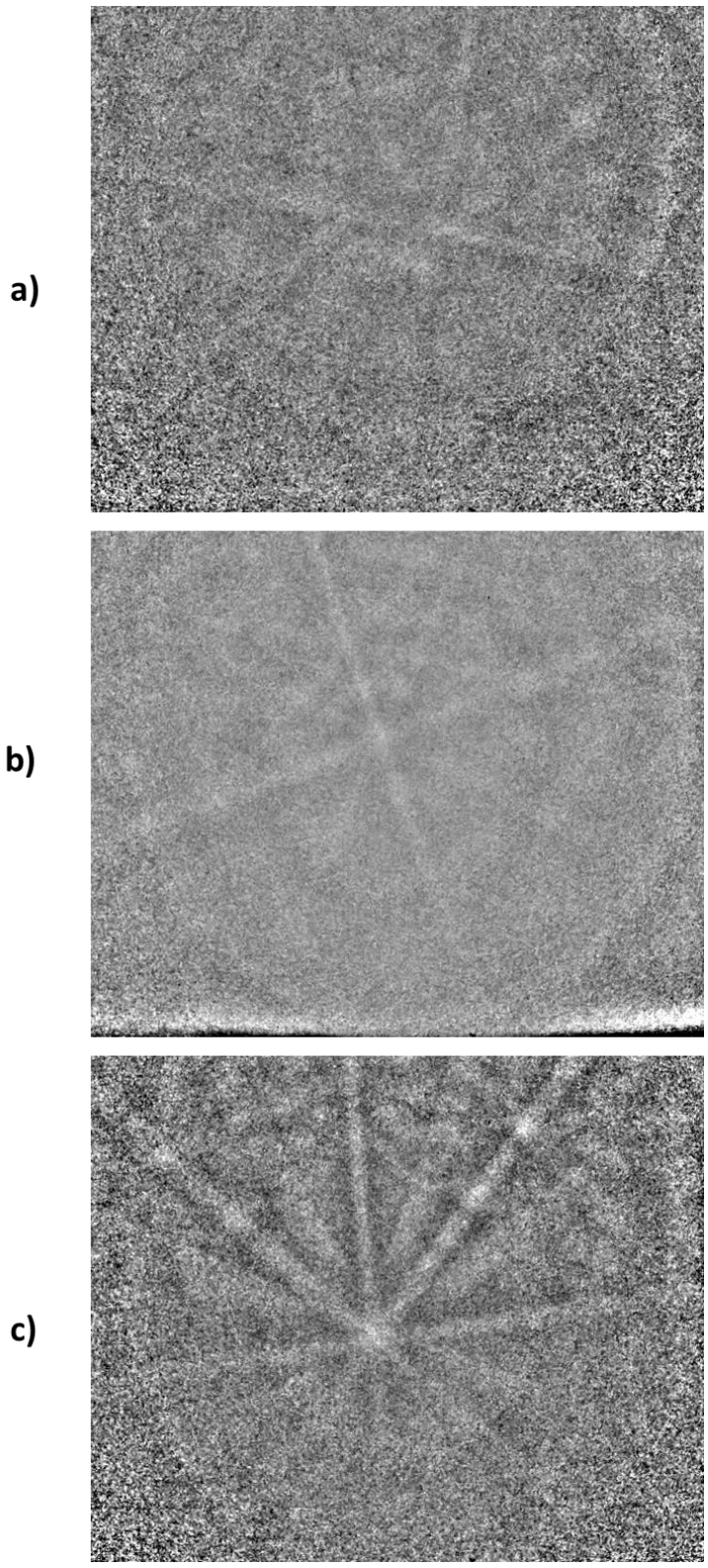

Figure 4.9: EBSD diffraction patterns after grinding with (a) 1200 grit SiC paper, polishing with (b) 0.05 μm alumina suspension and (c) 0.05 μm diamond suspension.

Although visual observation of the diffraction patterns is one method of quickly evaluating the sample preparation, this method of evaluation heavily depends on how each analyst perceives the pattern quality, especially in cases with diffraction patterns of similar contrast. As such, different analyst would have their own opinions on how good the patterns were. Therefore, to minimize this ambiguity, the average number of diffraction bands detected, and the average MAD value were used to quantify the pattern quality. A summary of the average diffraction bands detected, and average MAD values acquired is shown in Table 4.1.

Table 4.1: Table of average diffraction bands detected, and average MAD value acquired after sample grinding and polishing.

Grinding/Polishing Stage	Average Bands Detected	Average MAD Value
1200 grit SiC paper	7	1.31
0.05 μm alumina suspension	8	1.01
0.05 μm diamond suspension	9	0.85

After grinding with 1200 grit SiC paper, the average number of diffraction bands detected was 7 out of a maximum detection limit of 12 bands. The average MAD value obtained after this stage was 1.31. As the deviation value was way over the acceptable limit of 0.6, the diffraction pattern will not be useful for EBSD analysis as results obtained from subsequent data processing may not be accurate due to the large angular deviation. Similarly, after polishing was done with 0.05 μm alumina suspension, only 8 diffraction bands were detected from the patterns. However, there was a slight improvement in the average MAD value at 1.01, which was lower as compared with the value obtained with 1200 grit SiC grinding. Although there was overall improvement in the angular deviation value, it was still above the value limit of 0.6. Hence, further EBSD analysis would not be deemed accurate as well. Lastly, with a final polish using 0.05 μm diamond suspension, the overall diffraction patterns acquired were significantly improved. The software was able to determine an average of 9 diffraction bands from the patterns and the average MAD value was determined to be at 0.85. As this MAD value was still more than 0.6, the diffraction pattern obtained after the final polish stage was still insufficient for accurate analysis.

Overall, with the standard sample preparation workflow, it was observed that a final mechanical polish with 0.05 μm diamond suspension produced the best diffraction pattern quality as compared with fine grinding with 1200 grit SiC paper and mechanical polishing with 0.05 μm alumina suspension. This was in line with the fact that diamond being the hardest material, was able to remove material more efficiently and hence produce the best surface finish among the grinding and polishing steps. However, the diamond polished surface finish was still insufficient for accurate EBSD analysis, with its MAD value still above the acceptable limit of 0.6. Therefore, a further polishing technique known as ion beam polishing was performed in a bid to acquire higher-quality diffraction patterns.

4.3 Ion Beam Polishing

Ion beam polishing was used as a final step in the sample preparation process. Generally, ion beam polishing uses ions to bombard the top surface atoms of a sample and removing them in the process to reveal a clean underlying surface. Ion beam polishing was subsequently performed on 0.05 μm diamond suspension polished samples. Two types of ion beam polishing techniques, namely Focused Ion Beam (FIB) and Broad Ion Beam (BIB) polishing, were used and the resulting surface finish of the samples after polishing by the respective techniques were compared.

4.3.1 Focused Ion Beam (FIB) Polishing

Focused ion beam (FIB) is a technique that has been widely used in sample preparation for TEM and SEM analysis. The gallium (Ga) ion beam used can remove material from the sample surface to reveal regions of interest for EBSD analysis. The exposed surface can then be subjected to EBSD analysis directly without the need for any further preparations, making it especially useful as a final polish step. For this study, FIB polishing was performed using a Thermo Fisher Scientific Helios NanoLab 450S (see Figure 4.10) and the polishing setup of the FIB polishing is as shown in Figure 4.11, where the sample surface to be polished was tilted 1.5 ° to the incident ion beam.

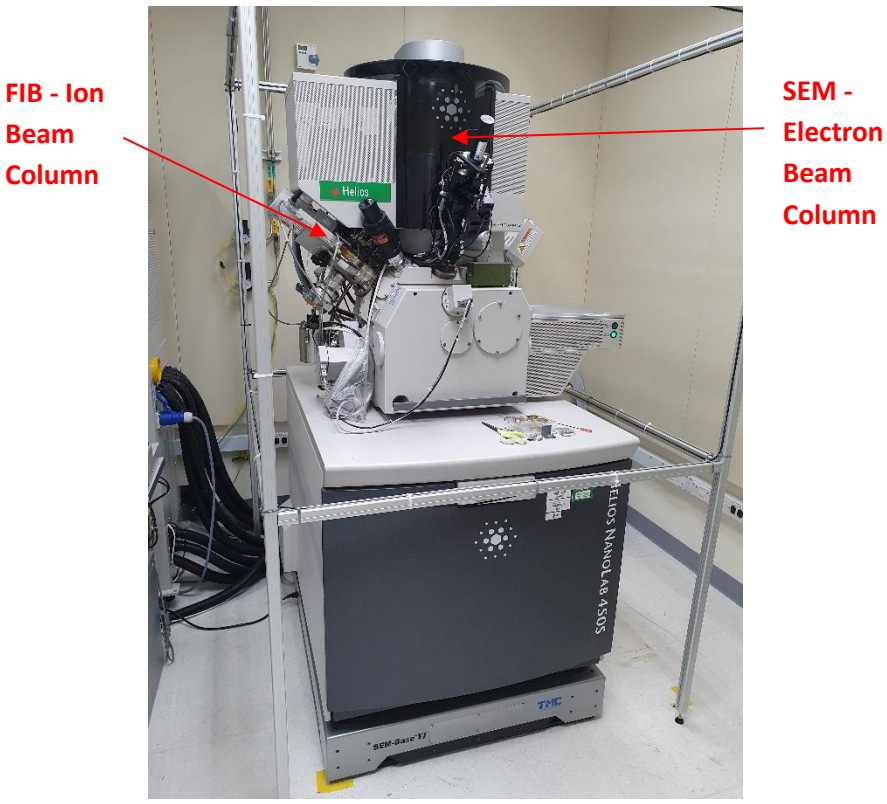

Figure 4.10: Thermo Fisher Scientific Helios NanoLab 450S.

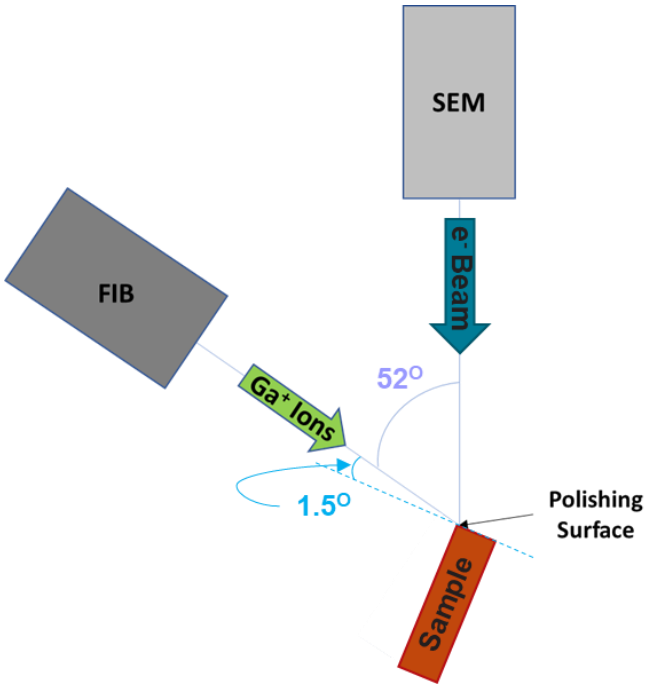

Figure 4.11: Schematic of FIB polishing setup.

During FIB polishing, high-energy Ga^+ ions strike the sample, sputtering atoms from the surface to reveal a clean underlying surface. However, the Ga^+ ions can also potentially become implanted onto the top few nanometers of the sample surface, and in turn causes the surface to become amorphous. This damage to the crystalline surface may result in extremely poor quality EBSD patterns that would not allow useful data to be collected. To minimize the amorphization of the sample surface as much as possible, a small probe current of 1 nA was used. The use of a small probe current would also reduce the effects of curtaining. However, with the probe current limited to a small value of no more than 1 nA, the polishing rate of the bump was slow. To fully polish a single copper pillar solder bump, the amount of time taken was well over 10 hours. As such, FIB polishing to prepare a row of bumps for EBSD analysis was not deemed efficient as a considerable amount of time would be required. Therefore, an alternative technique of ion beam polishing known as broad ion beam polishing was explored as well.

4.3.2 Broad Ion Beam (BIB) Polishing

In recent years, broad ion beam (BIB) polishing has become one of the most widely used techniques for surface preparation. This technique utilizes high-energy argon ions to bombard a sample, milling away materials in the process. Surface quality after BIB polishing is known to be very good for surface sensitive studies, such as EBSD. As compared to Ga^+ FIB polishing, BIB produces a surface finish with very minimal levels of damage. Furthermore, BIB polishes over a wider area than FIB and is also able to avoid issues that are associated with edge-on milling methods, such as curtaining [6]. In this study, BIB polishing was done using a Leica EM TIC 3X Triple Ion Beam System miller (see Figure 4.12). Following mechanical cross section grinding and polishing, the samples were then loaded into the ion miller for the final surface polishing. Two different methods of BIB polishing were performed in this study, namely slope cut polishing and rotary polishing.

Figure 4.12: Leica EM TIC 3X.

4.3.2.1 Slope Cut Polishing

Slope cut polishing is a method used in cross section sample preparations. In this method, a sharp-edged mask is placed over the sample such that only a small region of the sample of approximately 30 μm is exposed above the mask. An ion beam from the direction of the mask would strike the exposed sample region, removing material in the process. The resulting surface finish of the sample would have minimal preparation artifacts due to the parallel incidence of the ion beam. The setup and side view schematic of slope cut ion milling is shown in Figure 4.13 and Figure 4.14, respectively.

For slope cut polishing of the copper pillar solder bumps, the mechanically prepared sample was first mounted onto a standard stage sample holder and placed into the ion miller with the surface to be polished exposed and orientated parallel to the ion gun. The sample and the ion milling mask were then adjusted such that approximately 30 μm of material was exposed above the mask for the ion beam to mill away.

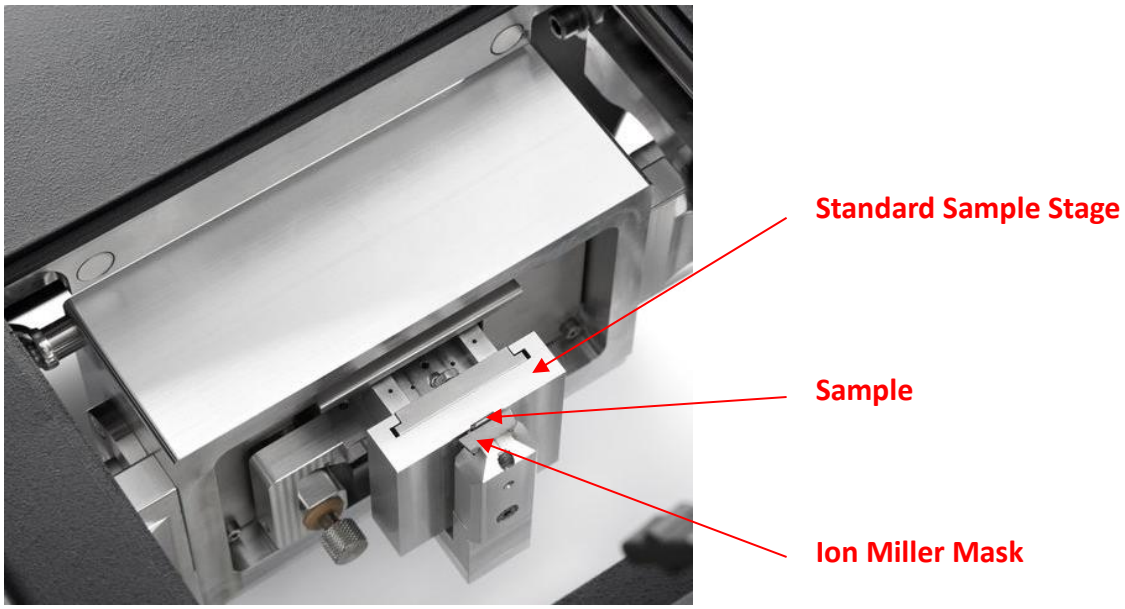

Figure 4.13: Leica EM TIC 3X standard stage slope cut polishing setup [2].

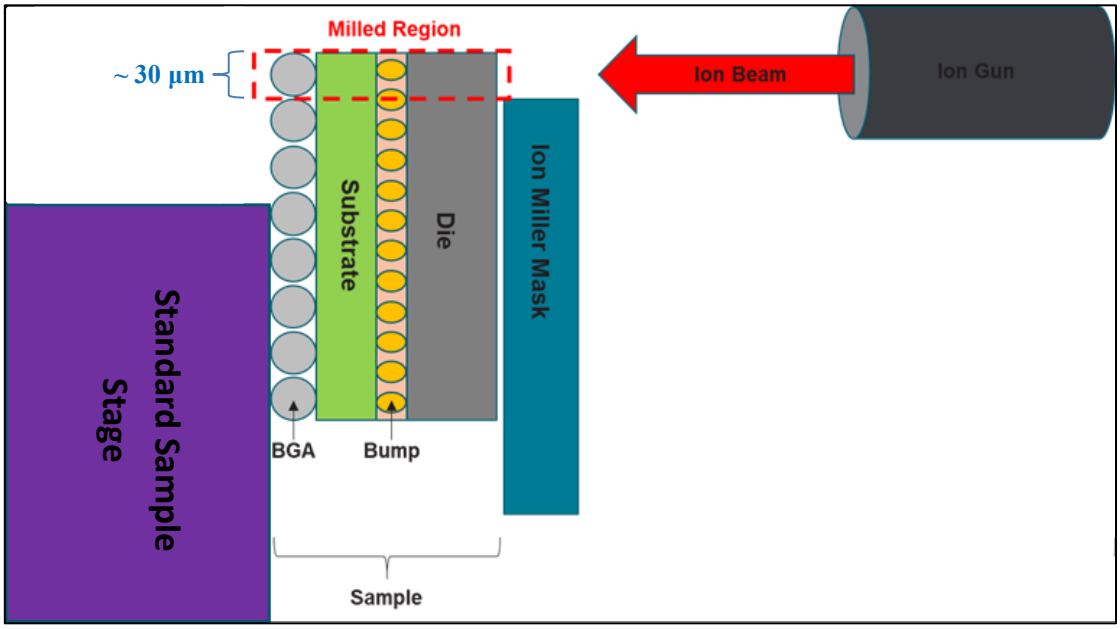

Figure 4.14: Side view schematic of slope cut setup.

An accelerating voltage of 5.5 kV to 6 kV was used for the surface polishing. However, at that accelerating voltage, it required more than 20 hours to fully polish the entire copper pillar solder bump. Polishing time could be reduced with an increase in the accelerating voltage. However, increasing too high of the voltage may lead to redeposition of material onto the sample surface as well. Therefore, to balance the accelerating voltage and polishing duration, a two-step polishing setup was used. A larger accelerating voltage was used first to remove most of the material before using a lower voltage for the final polishing. As such, an accelerating voltage of 8 kV was first used to mill the sample for a duration of 12 hours before a final polish at 4 kV for 1 hour.

4.3.2.2 Rotary Stage Ion Polishing

In contrast to slope cut polishing, polishing with a rotary stage can uniformly process large sample surfaces by employing a combination of two stage movements, rotation, and translation as seen in Figure 4.15. The rotary stage also allows the sample to be tilted from a range 0 ° to 48 °. By adjusting the sample tilt at various angles with respect to the incident ion beam, the sample surface can either be polished, cleaned, or even contrast enhanced.

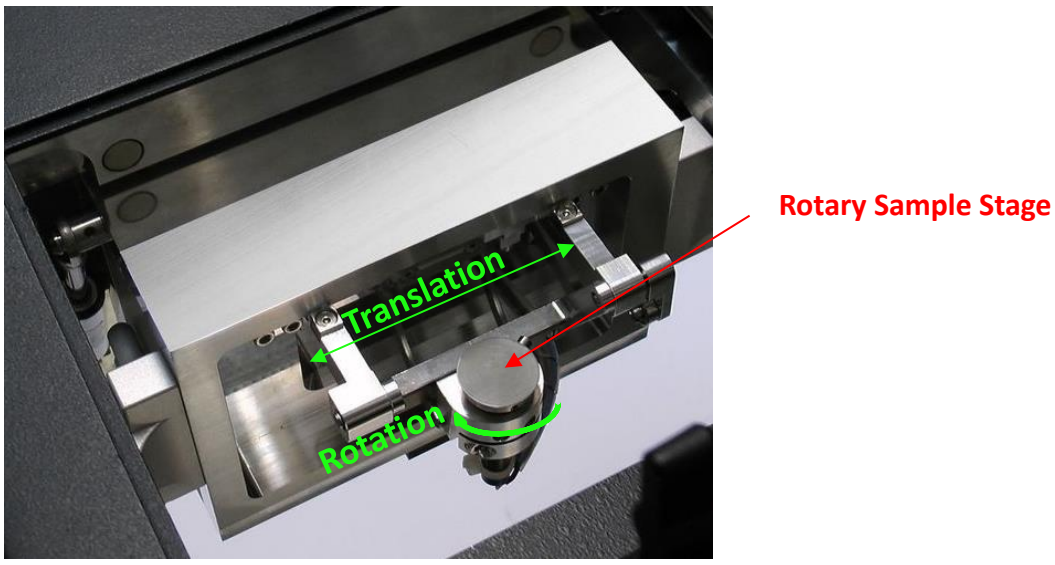

Figure 4.15: Leica EM TIC 3X rotary stage [2].

For the final polishing of the Cu pillar bump sample via the rotary stage, the sample was first mechanically polished to remove most of the surface artifacts. The quality of the mechanical polishing should be as high as possible as the rotary ion cleaning is only the final step in improving the surface finish quality. Due to the relatively low milling angle used in this final cleaning step, the sample surface will not be affected too drastically. As such, any deep scratches that are inherently present must be removed prior to the ion cleaning to obtain a smooth surface finish. If not, even after the ion cleaning, the scratches will remain.

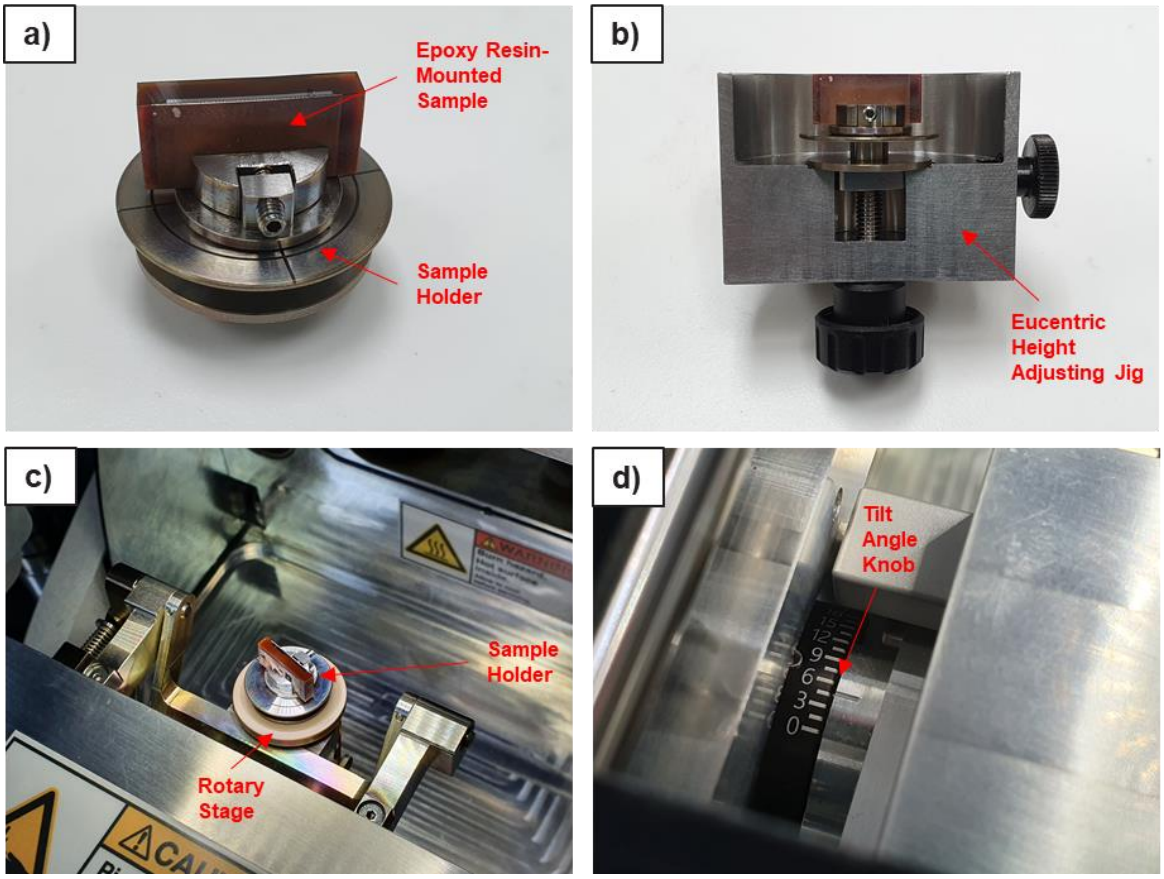

Figure 4.16: Rotary polishing setup with (a) mounting sample onto sample holder, (b) adjusting sample surface to eucentric height, (c) loading sample on sample holder onto rotary stage, and (d) setting the tilt angle for polishing.

In rotary ion polishing, mask is not required. As shown in Figure 4.16, to ensure that the sample surface and ion beam are aligned, the sample holder was set at an eucentric height using an eucentric height adjusting jig, before loading onto the ion miller rotary stage. A tilt angle of 4.5 ° was first set for the initial milling. Given the large area milling capabilities of the rotary stage, an accelerating voltage of 6 kV was used to polish the sample surface for a duration of 1.5 hours. A translational distance of half the sample width was also set to ensure that the sample surface was uniformly milled across. As the rotary stage has the option of allowing the tilt angle to be varied during polishing, after the initial polishing at 4.5 °, the sample was set for a final polishing at a tilt angle of 10.5 °, at an accelerating voltage of 4 kV for 15 minutes. Studies have shown that ion beam incidence angle influences EBSD pattern image quality (IQ) [3]. As shown in Figure 4.17, average pattern IQ increases to a maximum at around an incidence angle of 10 °, where it will start to decrease at higher angles. This decrease at higher angles can be due to the channeling effect, roughness of the sample surface and inhomogeneous sputtering [3].

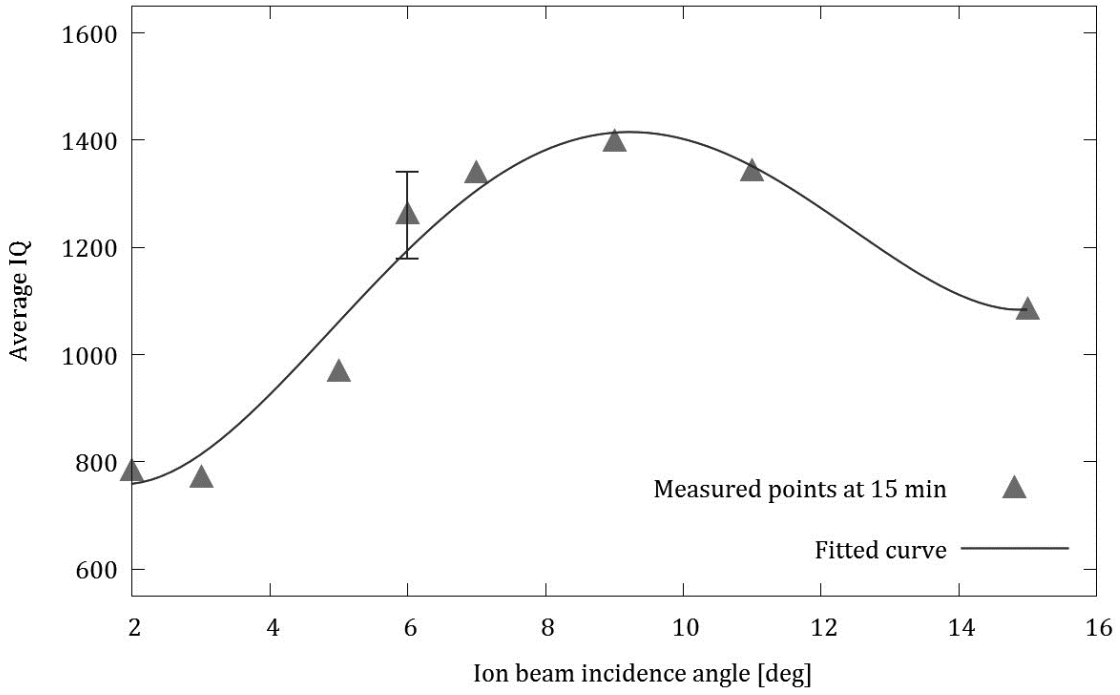

Figure 4.17: Effect of ion beam incidence angle on average IQ [3].

4.3.3 Results and Discussion of Ion Beam Polishing

SEM images of the Cu pillar solder bump sample surfaces after FIB milling, ion miller slope cut polishing and ion miller rotary stage polishing were observed as follow in Figure 4.18. and EBSD pattern quality of the samples are shown in Figure 4.19.

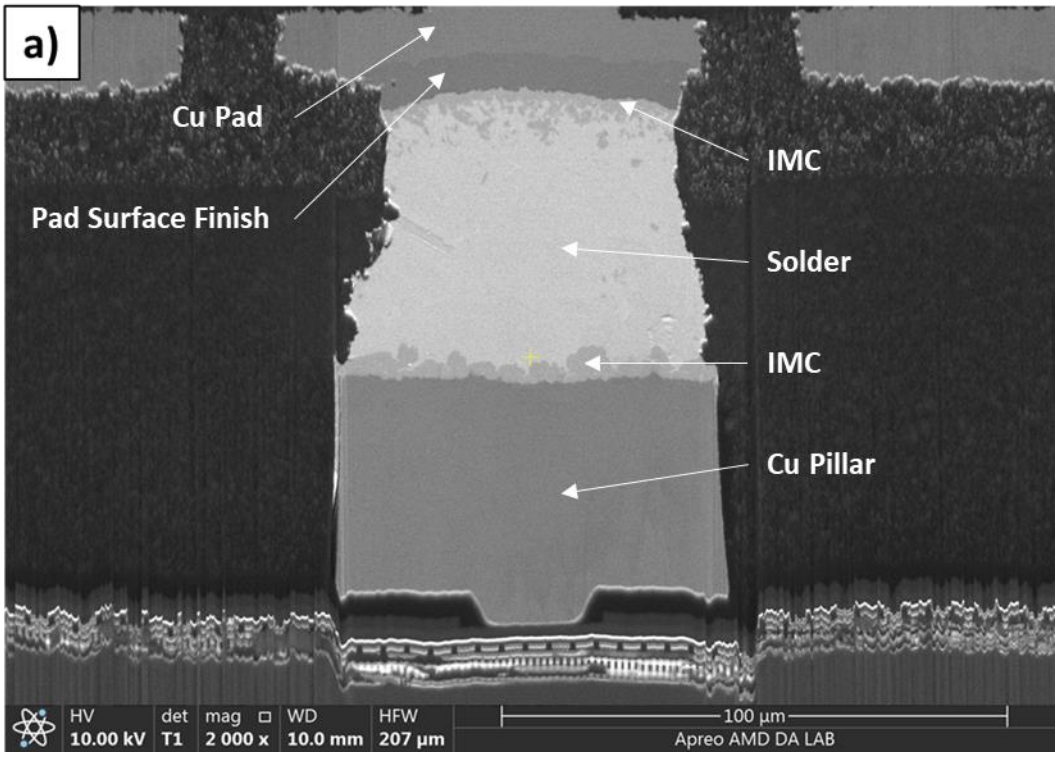

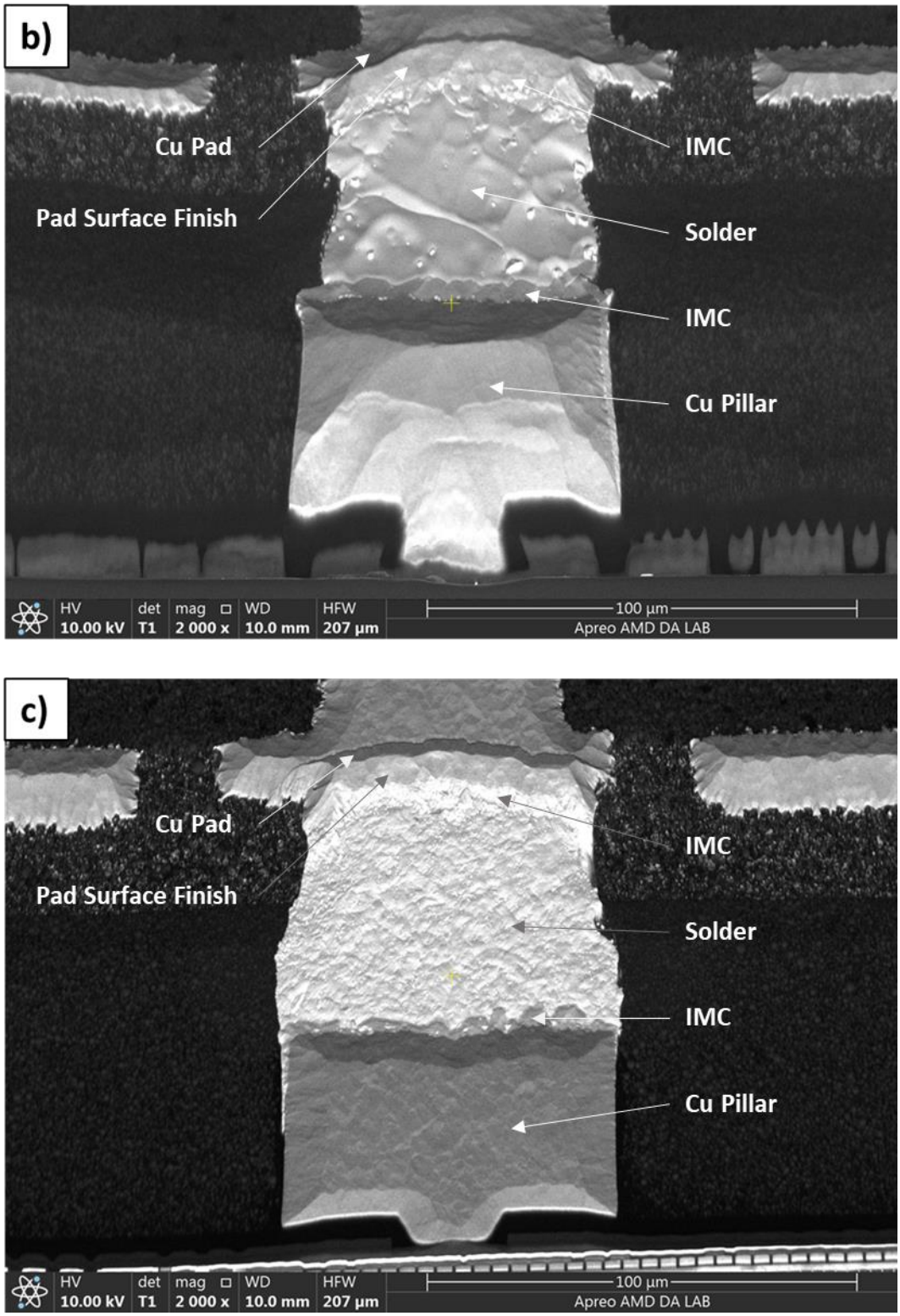

Figure 4.18: SEM images of sample surface after polishing by (a) FIB, (b) slope cut ion miller polishing, and (c) rotary stage ion miller polishing.

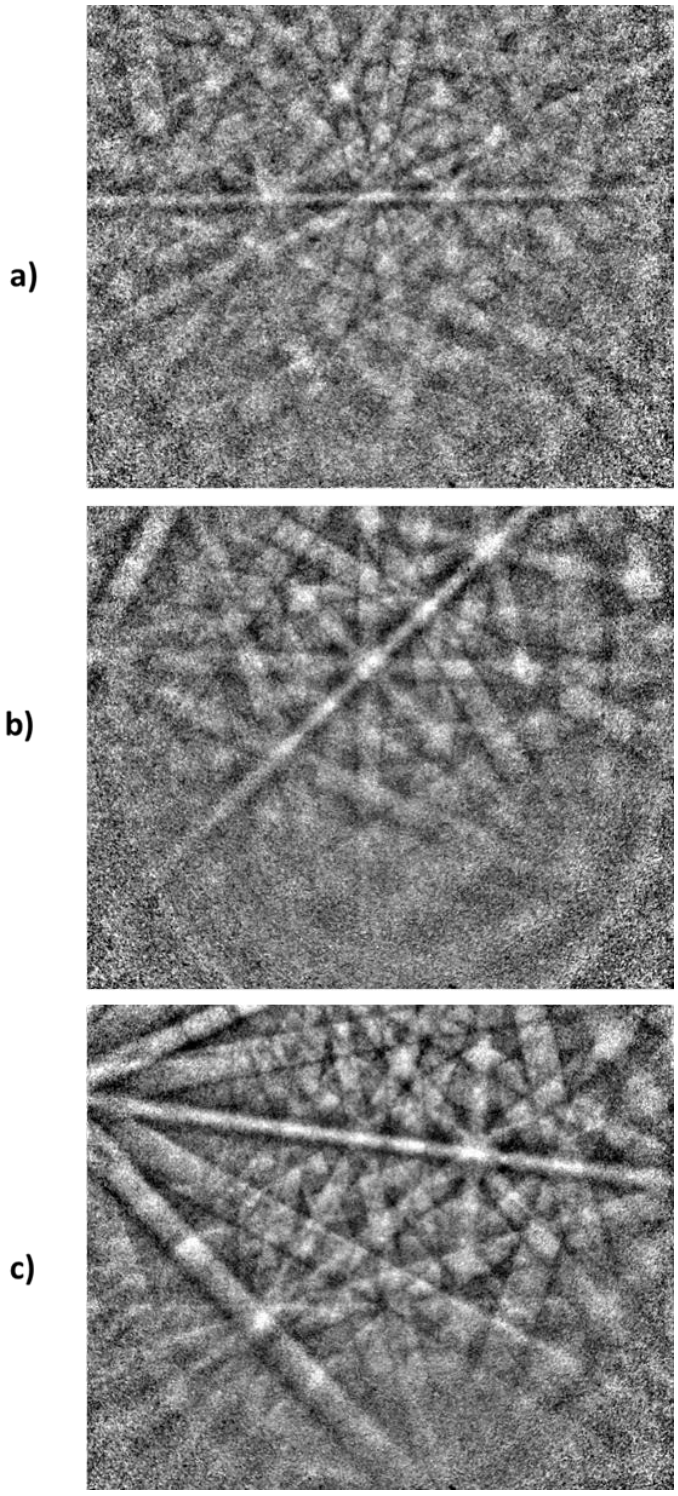

Figure 4.19: EBSD diffraction patterns after ion beam polishing with (a) FIB, (b) slope cut ion mill polishing and (c) rotary stage ion mill polishing.

From visual observation of the diffraction patterns, it was observed that after ion beam polishing, the patterns obtained is significantly clearer and sharper as compared with mechanical polishing. The summary of the average diffraction bands detected, and average MAD values acquired by the ion beam polishing techniques is as shown in Table 4.2.

Table 4.2: Table of average diffraction bands detected, and average MAD value acquired after ion beam polishing.

Polishing Technique	Average Bands Detected	Average MAD Value
FIB polish	9	0.72
BIB slope cut polish	10	0.68
BIB rotary stage polish	11	0.55

The average number of diffraction bands detected was 9 after the sample was polished with FIB. The average MAD value obtained from this technique was 0.72. As for the average number of diffraction bands and average MAD values obtained from the ion miller polished samples, the slope cut polished sample has an average of 10 diffraction bands detected and the average MAD value was 0.68. Lastly, the rotary stage polished sample obtained the highest number of average diffraction bands detected amongst all the preparation techniques at 11 bands and the MAD value obtained was the lowest at 0.55.

By comparing the SEM images obtained from the different ion beam polishing techniques, it was observed that curtaining effect was present on the sample surface obtained from the FIB polishing. Typically, curtaining effects is seen as vertical lines on the milled surface, as seen in a close-up SEM image in Figure 4.20, and its occurrence can be due to various reasons. Curtaining, or sometimes known as waterfall effect, occurs as a result of porous materials or in this case of Cu pillar solder bump, a composite of different materials which causes a spatial variation of the sputter rate in the material [4]. Curtaining effect is not a desirable outcome for EBSD analysis as it results in the sample surface becoming uneven and where subsequent EBSD diffraction signals will be weakened. For the ion miller polished samples, no curtaining effects were observed.

Therefore, this could be the reason the FIB polished samples were not able to attain as high a diffraction pattern quality as the ion miller polished samples.

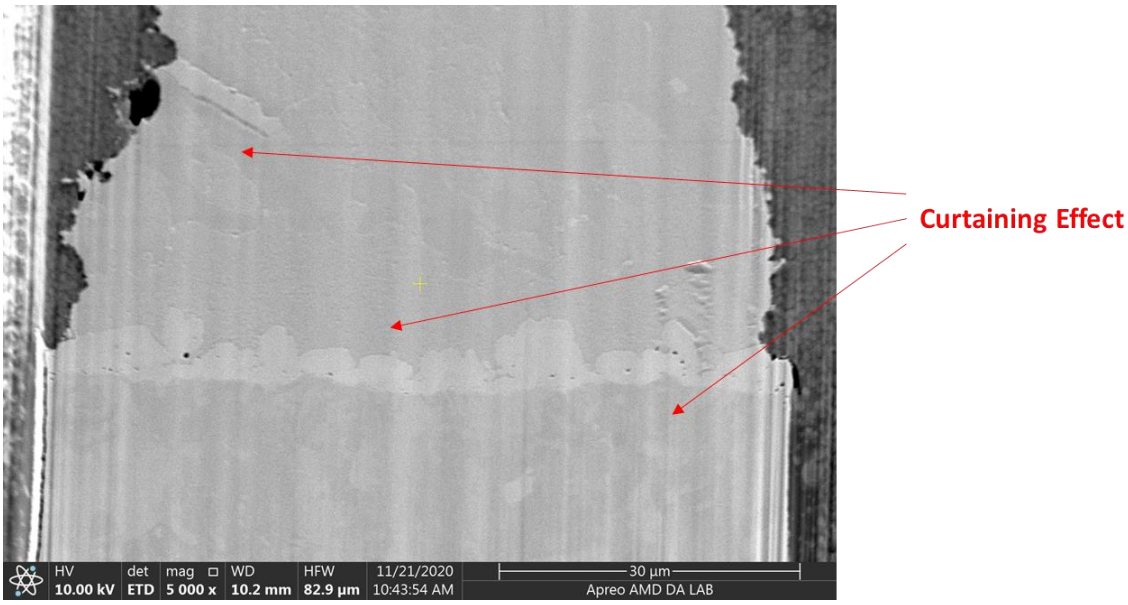

Figure 4.20: Close-up SEM image of a Cu pillar solder bump sample with visible curtaining effect on FIB polished surface.

On the other hand, as compared to the 10.5 ° tilted sample in the rotary stage ion milling polish, the slope cut ion milling polish sample surface was positioned parallel to the incident beam. During the process of ion milling, incident ions will transfer energy to the atoms on the target surface through series of collisions. If the target surface atoms manage to gain enough energy to overcome the surface binding energy, then the atoms will be removed from the surface. This removal of atoms will depend mainly on the surface material and the energy density provided to the surface atoms, which is in turn, is affected by the direction of incidence of the ion beam [5]. Hence, based on the relation shown in Figure 4.17, the sample prepared with the rotary stage at a tilted angle will produce an overall better surface finish for generating EBSD diffraction pattern.

4.4 Sample Preparation Summary

In summary, it is possible to prepare and attain a better sample finish for EBSD analysis with the use of BIB rotary stage polishing. The EBSD diffraction pattern quality obtained with this technique was the best among all the techniques explored. Therefore, for the sample preparation of copper pillar solder bumps for EBSD analysis in this study, diamond suspension was used in the mechanical polishing step followed by BIB rotary stage polishing in the ion beam polishing step, as shown by the workflow in Figure 4.21.

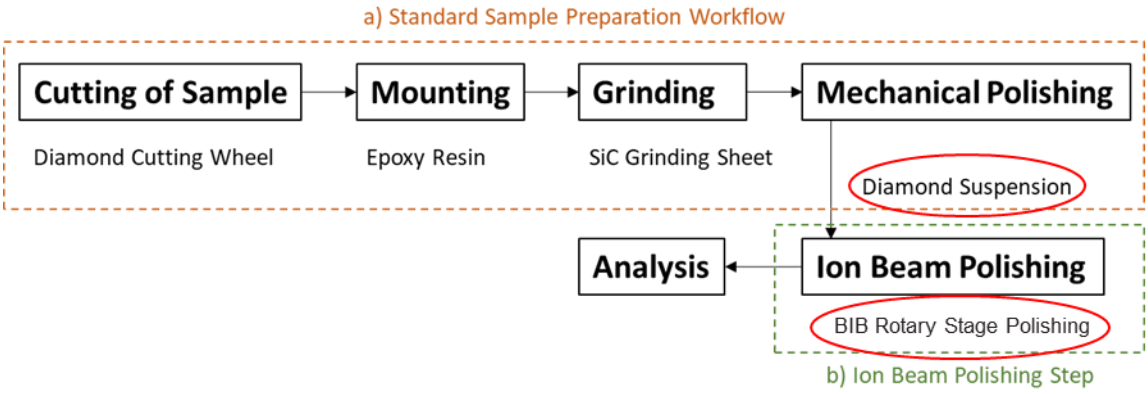

Figure 4.21: Sample preparation workflow used for samples in subsequent EBSD analysis.

References

[1] R. Pandher, T. Lawlor, " Effect of Silver in Common Lead-free Alloys", 2009

[2] P. L. Tu, Y. C. Chan, J. K. L. Lai, "Effect of Intermetallic Compounds on the Thermal Fatigue of Surface Mount Solder Joints", IEEE Transactions on Components, Packaging, and Manufacturing Technology: Part B, 1997, 20(1), pp. 87-93

[3] A. Akkurt, "The Effect of Cutting Process on Surface Microstructure and Hardness of Pure and Al 6061 Aluminum Alloy", *Engineering Science and Technology, an International Journal*, 2015, Vol.18(3), pp. 303-308

[4] T. H. Loeber, B. Laegel, S. Wolff, S. Schuff, F. Balle, T. Beck, D. Eifler, J. H. Fitschen, G. Steidl, "Reducing Curtaining Effects in FIB/SEM Applications by a Goniometer Stage and an Image processing Method", Journal of Vacuum Science and Technology. B, Nanotechnology & microelectronics, 2017, Vol.35(6), pp. 6

[5] T. Berecz, S. Kalácska, G, Varga, Z. Dankházi, K. Havancsák, "Effect of High Energy Ar-Ion Milling on Surface of Quenched Low-Carbon Low Alloyed Steel", *Materials Science Forum*, 2015, Vol.812, pp. 285-290

[6] A. Gholinia, M. E. Curd, E. Bousser, K. Taylor, T. Hosman, S. Coyle, M. H. Shearer, J. Hunt, P. J. Withers, "Coupled Broad Ion Beam-Scanning Electron Microscopy (BIB-SEM) for Polishing and Three-Dimensional (3D) Serial Section Tomography (SST)", *Ultramicroscopy*, 2020, Vol.214, 112989

Chapter 5

IMC Phase Identification at Solder Joint

Before analysis and studies can be done on the IMCs, it is important to first determine if the IMC phases are accurately identified. Phase identification was performed separately via EBSD and EDX and the results were compared. EBSD provides crystallographic information on the IMC while EDX determines the elemental composition of the IMC. By utilizing both EBSD and EDX techniques together, the IMC phases could be identified with more accuracy. A study of the substrate side IMCs was then done between SAC305 and Sn0.7Cu substrate solder samples. Comparison of the IMCs was also done under temperature cycling and high temperature storage conditions to determine the feasibility of Sn0.7Cu solder as an alternative in mitigating ILD cracks and delamination risks. With the application of EDX and EBSD techniques, the results showed that there were no significant differences in the IMCs of both substrate solders, confirming Sn0.7Cu solder as a viable alternative.

* This section is published substantially as "Application of EBSD Study of Cu-Sn IMCs in SAC305 and Sn0.7Cu Solder Joints to Determine the Suitability of Sn0.7Cu Solder as Alternative in Mitigating ILD Cracks/Delamination" in proceedings of the 23rd Electronics Packaging Technology Conference (EPTC), 2021. Reprinted with permission. © 2021 IEEE

5.1 Phase Identification

The first step after obtaining the primary raw EBSD data is to determine if the phases present in the sample are accurately identified. To determine this, a copper pillar solder bump sample was prepared, comprising of commercially available SAC305 solder of 96.5% Sn, 3.0% Ag and 0.5% Cu. The IMCs were observed under SEM at the interface between the copper pillar and solder as shown in Figure 5.1. Typically, interfacial Cu-Sn based solder IMCs mainly compose of Cu_6Sn_5 (η phase) and Cu_3Sn (**ε** phase). As seen from the Cu-Sn system phase diagram from Figure 2.2 in Chapter 2, Cu_3Sn is Cu-rich and will tend to form on the copper pillar side, while Cu_6Sn_5 will form on the solder side.

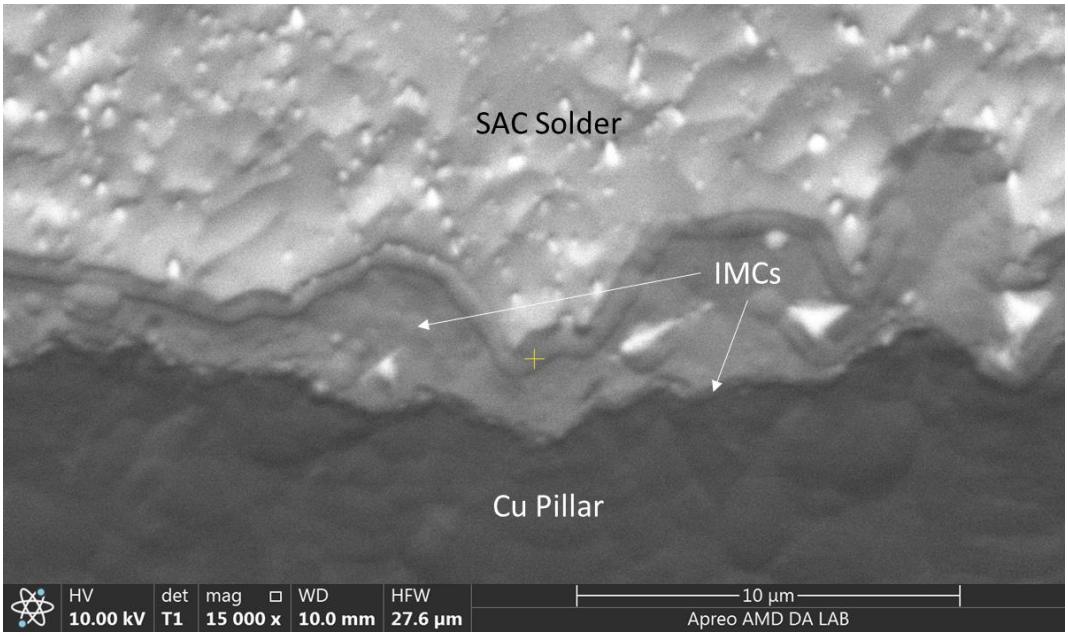

Figure 5.1: Close-up SEM image of T=0 bump with IMC region indicated.

Morphology of Cu_6Sn_5 grains is observed to be characteristically scallop-type. On the other hand, Cu_3Sn in the IMCs is not easily identifiable, due to its small grain sizes and it consists of the same elements as Cu_6Sn_5. As the anisotropic properties of both these IMC phases can greatly affect the reliability of the interconnect joints, it is therefore important to analyse the growth direction and orientation of each of the IMC phases. Thus, there is a need to be able to distinguish between the two Cu_6Sn_5 and Cu_3Sn IMC phases.

5.2 Phase Identification by EBSD Indexing

In EBSD analysis, crystallographic information is obtained from diffraction patterns. This extracted information is compared with information from a standard database to determine the possible phases, after which a best-fit solution is determined. Cu_6Sn_5 can exist as two different crystal structures, namely hexagonal η phase Cu_6Sn_5 at high temperatures, usually above 186 °C and monoclinic η' phase Cu_6Sn_5 at lower temperatures (refer to phase diagram in Figure 2.2). Cu_3Sn on the other hand, has an orthorhombic **ε** phase.

EBSD was performed on the time = 0 (T = 0) bump with the focus at the IMC region. The crystallographic information acquired was compared against crystallographic information from the National Institute of Standards and Technology (NIST) Inorganic Crystal Structure Database (ICSD) provided in the EBSD software. Generally, crystallographic information obtained will allow the identification of the IMC phases easily. However, in the case of the Cu-Sn IMC system, because of the small grain sizes of Cu_3Sn, it was a challenge for the EBSD to get a good signal. The diffraction pattern quality of Cu_3Sn obtained was not optimal, as compared with the diffraction pattern quality of Cu_6Sn_5, shown in Figure 5.2. However, as observed from Table 5.1, the average diffraction bands detected for Cu_6Sn_5 and Cu_3Sn were 11 and 9 respectively and the average MAD values for both IMCs were 0.46 and 0.68, respectively.

a)

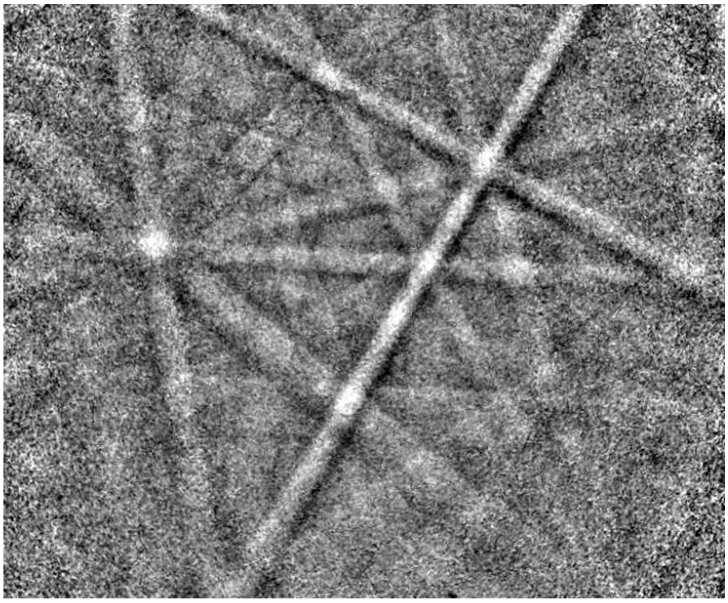

b)

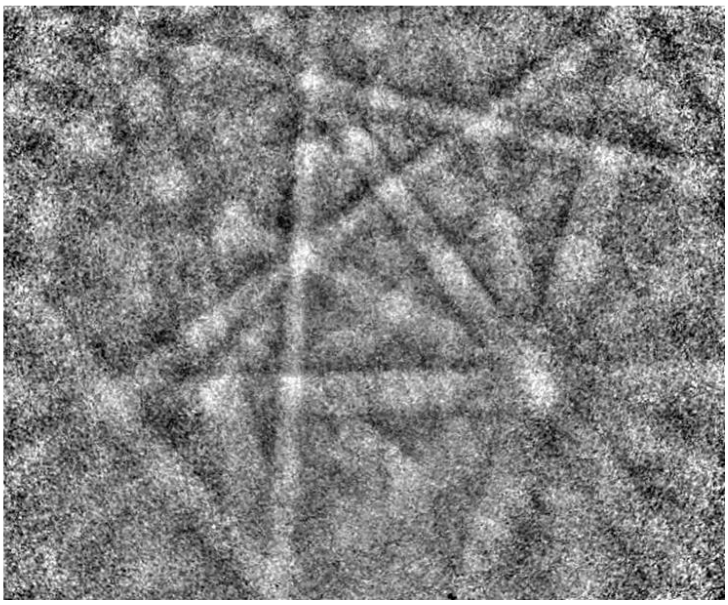

Figure 5.2: EBSD diffraction pattern obtained at supposed (a) Cu_6Sn_5 IMC region and at (b) Cu_3Sn IMC region.

Table 5.1: Table of average diffraction bands detected, and average MAD value acquired at the supposed Cu_6Sn_5 and Cu_3Sn regions.

IMC Phase	Average Bands Detected	Average MAD Value
Cu_6Sn_5	11	0.46
Cu_3Sn	9	0.68

As expected, with a MAD value of greater than 0.6, the diffraction pattern obtained for Cu_3Sn was not as accurate as Cu_6Sn_5. The resulting phase map obtained based solely on EBSD indexing was not able to accurately identify the Cu_3Sn phase, shown in Figure 5.3.

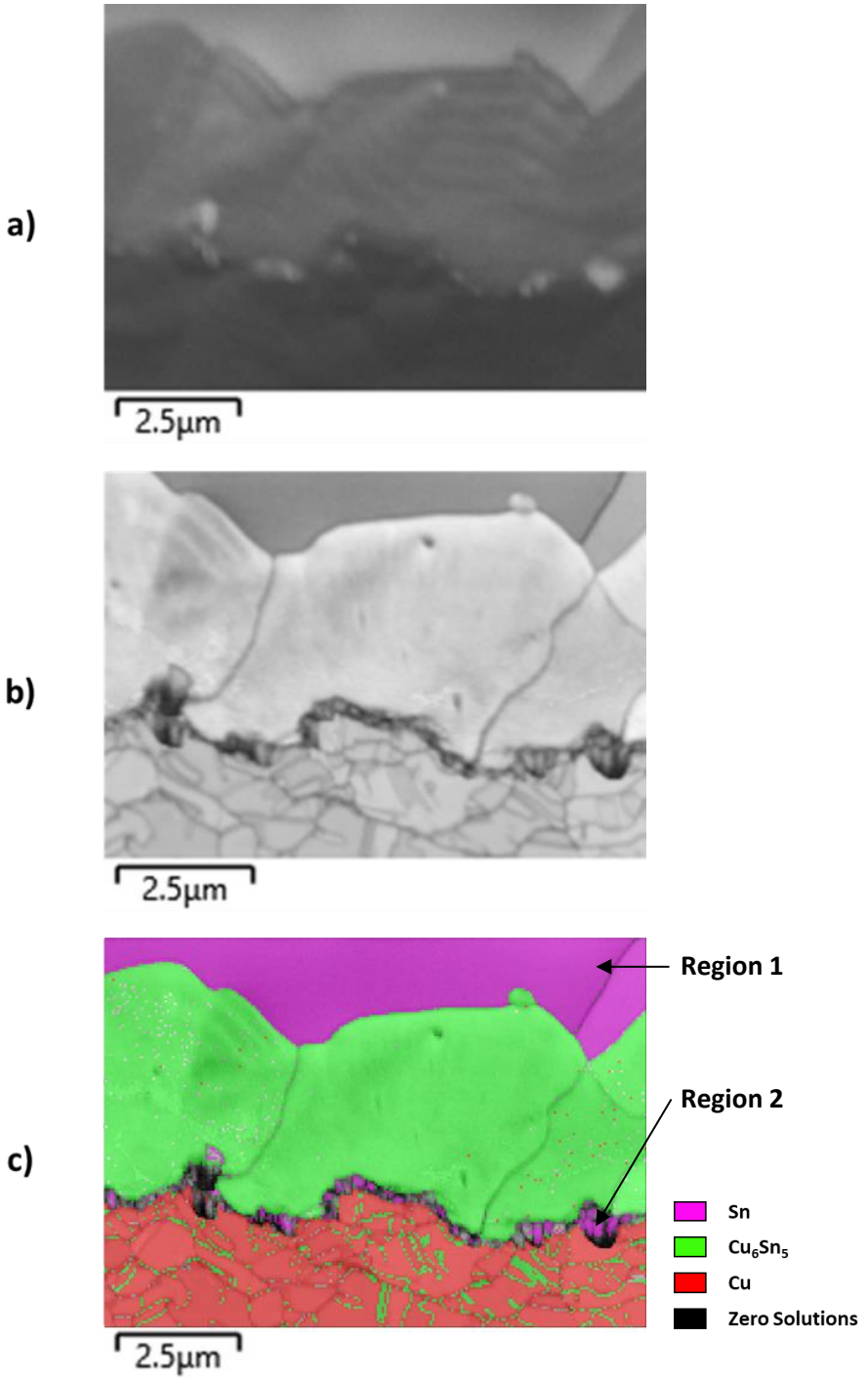

Figure 5.3: (a) SEM image of scanned IMC region, (b) EBSD band contrast map and (c) EBSD phase map overlaying band contrast map.

As observed from the phase map in Figure 5.3, Sn, Cu and the Cu_6Sn_5 phases were able to be identified. The region between the Cu and Cu_6Sn_5 phases (Region 2) is supposedly where Cu_3Sn phase was to be expected. However, from the phase map obtained, Region 2 where Cu_3Sn was supposed to be present was indexed as Sn. Furthermore, it was observed that small areas of Cu_6Sn_5 were indexed within the Cu pillar region as well. This may not be an accurate indexing as mentioned in Chapter 2, as IMC growth usually takes place at the Sn side, where the Sn is slowly consumed and transformed into Cu_6Sn_5. Upon closer inspection, it was observed that these areas of Cu_6Sn_5 were along the grain boundaries of the Cu pillar grains. A possible reason could be due to the fact that grain boundaries are disordered regions that have a lower melting point than the grains [1]. During reflow, the temperature of liquid Sn-rich solder may be high enough to melt the grain boundaries and penetrate along these grain boundaries forming a Cu-Sn liquid. Upon cooling, the Cu-Sn liquid then solidifies, forming Cu-Sn IMC. However, along the Cu pillar grain boundaries, the Cu-Sn liquid formed would be expected to be rich in Cu. Hence, the IMC formed along the grain boundaries was expected to be Cu-rich Cu_3Sn instead of Cu_6Sn_5 as observed in Figure 5.3. Therefore, indexing of the Cu pillar grain boundary region might not be accurate as well.

Furthermore, a comparison between Region 1 and Region 2 shows very different microstructures. Region 1 was indexed as Sn of very large grain size while Region 2 was indexed as Sn with very small grain size. Comparing together with the Cu_6Sn_5 grains and Cu grains, the very small grains observed at Region 2 is consistent with literature where Cu_3Sn is expected at that region. As such, it was noted that this method of phase identification based purely on EBSD indexing was not an accurate method. However, by gathering the chemical information with EDX, the phase identification process can be improved.

5.3 EDX Elemental Composition Analysis

To determine the chemical information of the phases present at the IMC region, EDX can be carried out. According to the NIST database, the general elemental atomic percentage (At.%) of Cu_6Sn_5 and Cu_3Sn are as shown in Table 5.2, where Cu_3Sn is expected to be more Cu-rich. By performing EDX at the IMC regions and comparing the composition of the data collected with the database, it would be possible to distinguish the two IMC phases.

Table 5.2: General elemental composition of Cu_6Sn_5 and Cu_3Sn IMCs.

IMC Phase	Cu (At.%)	Sn (At.%)
Cu_6Sn_5	55	45
Cu_3Sn	75	25

Hence, EDX spectrum was collected at several regions of the sample to determine the elemental composition at that position. Each region selected for EDX is denoted separately as regions 1, 2, 3 and 4 as shown in Figure 5.4. For each of the EDX region, upon collecting the spectra, the At.% of the elements was analyzed. Based on the At.% determined at the region, EBSD phase indexing would be improved. EDX spectra for the four regions are as shown in Figure 5.5 and the elemental compositions of each region are shown in Table 5.3-5.6.

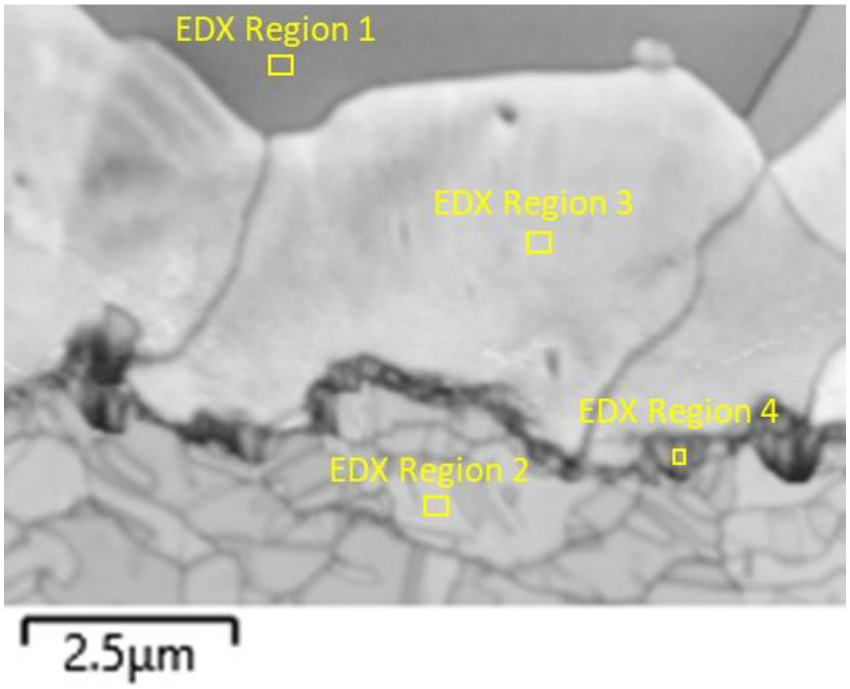

Figure 5.4: Regions of the sample subjected to EDX analysis.

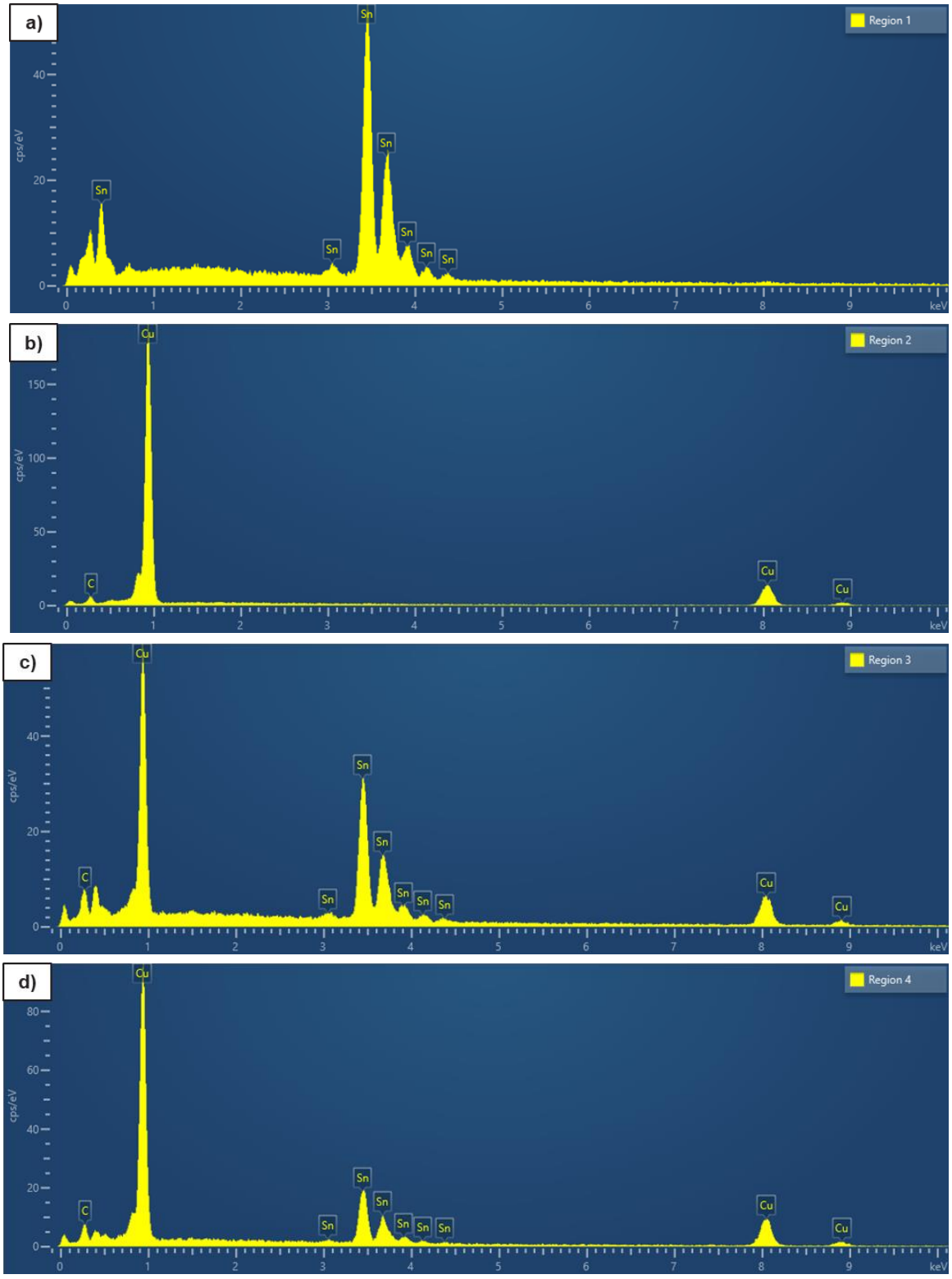

Figure 5.5: EDX spectra from (a) Region 1, (b) Region 2, (c) Region 3 and (d) Region 4.

Table 5.3: Elemental composition at Region 1 to Region 4.

	Cu (At.%)	Sn (At.%)	Total (At.%)
Region 1	0.0	100.0	100
Region 2	100.0	0.0	100
Region 3	69.5	30.5	100
Region 4	82.8	17.2	100

From the EDX spectra observed in Figure 5.5 and the At.% observed from Table 5.3, it was confirmed that Region 1 and Region 2 are Sn and Cu, respectively. For Regions 3 and 4, it was observed from the collected spectra that both Cu and Sn were present, suggesting that the two regions are likely the Cu-Sn IMCs. The amount of Cu and Sn at Region 3 are At.% 69.46 Cu and At.% 30.54 Sn while at Region 4, the composition was At.% 82.80 Cu and At.% 17.20 Sn. This suggests that Cu-rich Cu_3Sn was likely the IMC phase at Region 4 due to the higher At.% ratio of Cu to Sn at that region as compared to Region 3. Hence it is very likely that Region 3 was Cu_6Sn_5 phase and Region 4 was Cu_3Sn phase.

Having determined the chemical makeup of the different phases from EDX, the EDX information can then be used as reference spectrum and incorporated during EBSD analysis.

5.4 Phase Identification by Combination of EDX and EBSD

With the incorporation of the chemical information obtained from EDX, the software was then able to utilize this information during EBSD indexing to allow for a more accurate matching of phases with the database. With the additional EDX information, re-analysis of EBSD at the IMC region of the sample was done, and the resulting phase map as compared to the original EBSD phase map, are shown in Figure 5.6.

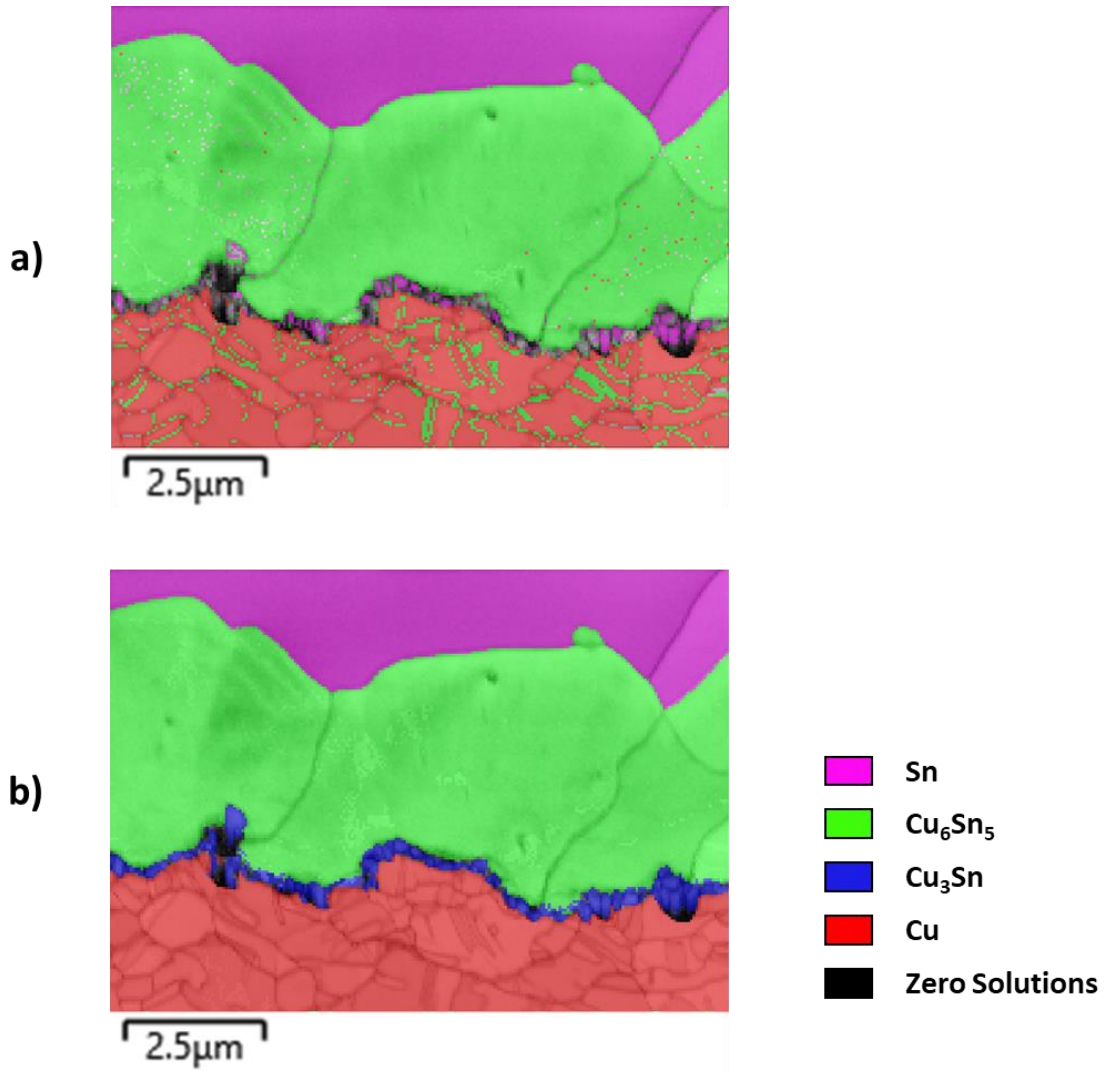

Figure 5.6: (a) Original EBSD phase map overlaying band contrast map and (b) re-analyzed EBSD phase map by combining EBSD and EDX overlaying band contrast map.

As observed in Figure 5.6, the new phase mapping is more consistent with the expected phases present. With the chemical composition of the phases identified by EDX providing as reference, the EBSD indexing was able to determine the presence of the Cu_3Sn phase and identify the region it occupies, whereas in the original EBSD phase map, only the Cu_6Sn_5 IMC was identified. In addition, the mis-indexed Cu_6Sn_5 at the Cu pillar region were corrected as well.

In summary, the original phase map obtained from EBSD indexing was only able to detect and index the Cu_6Sn_5 IMC phase. With EDX analysis, chemical information on the IMCs can be obtained. By utilizing both EDX and EBSD techniques together, both the Cu_6Sn_5 and Cu_3Sn IMCs were able to be detected and identified. This combination will allow for a more accurate phase identification which will aid in the subsequent study of the IMC regions.

With this, the ten samples mentioned in Chapter 3 was prepared and the IMCs were analyzed and compared.

5.5 IMC Phase Identity Comparison - SAC305 vs Sn0.7Cu at Time = 0

EBSD and EDX data were collected to identify and compare the phases and composition of SAC305 and Sn0.7Cu solder substrate side IMCs. From EBSD, phase and grain orientation maps for the SAC305 solder sample (Sample 0) as well as Sn0.7Cu solder sample (Sample Z) were collected and analyzed. EDX point spectrum was also obtained from the two samples to supplement the EBSD results.

Figure 5.7 shows the EBSD phase map obtained for Sample 0. From this phase map, it was observed that in Sample 0, the IMC phase present at the substrate side was determined to be mainly $(Cu, Ni)_6Sn_5$ with some Ag_3Sn particles disperse in the solder matrix. Cu and Ni are known to be mutually substitutable in the IMC lattice. As a result, $(Cu, Ni)_6Sn_5$ will typically be the dominant IMC phase [2-4], consistent to the observation in Figure 5.7. To further confirm the identity of the $(Cu, Ni)_6Sn_5$ IMC, EDX data was also collected at two regions of the sample, Region 1 and Region 2, marked in Figure 5.7. The EDX spectra of both regions is shown in Figure 5.8 and the individual elemental composition at each region is shown in Table 5.4 and Table 5.5 respectively.

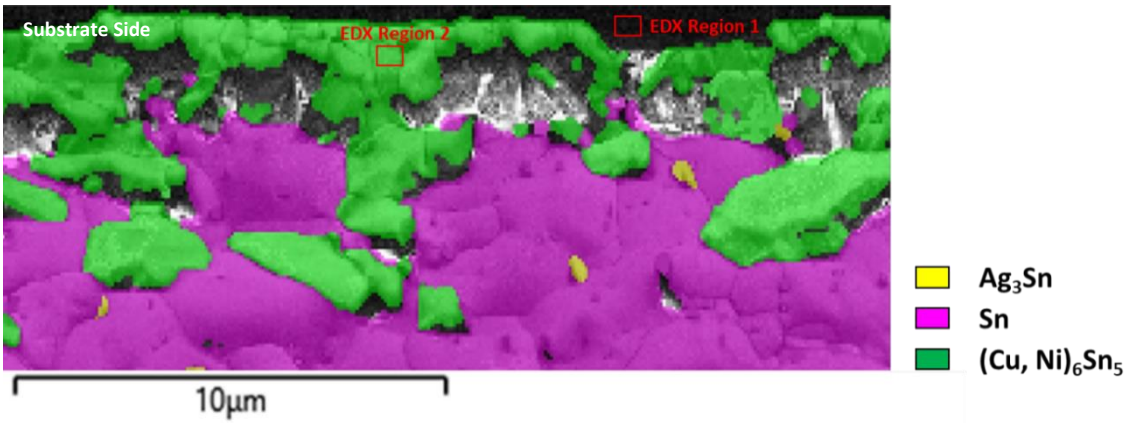

Figure 5.7: EBSD phase map of substrate side IMC showing $(Cu, Ni)_6Sn_5$ phase in Sample 0.

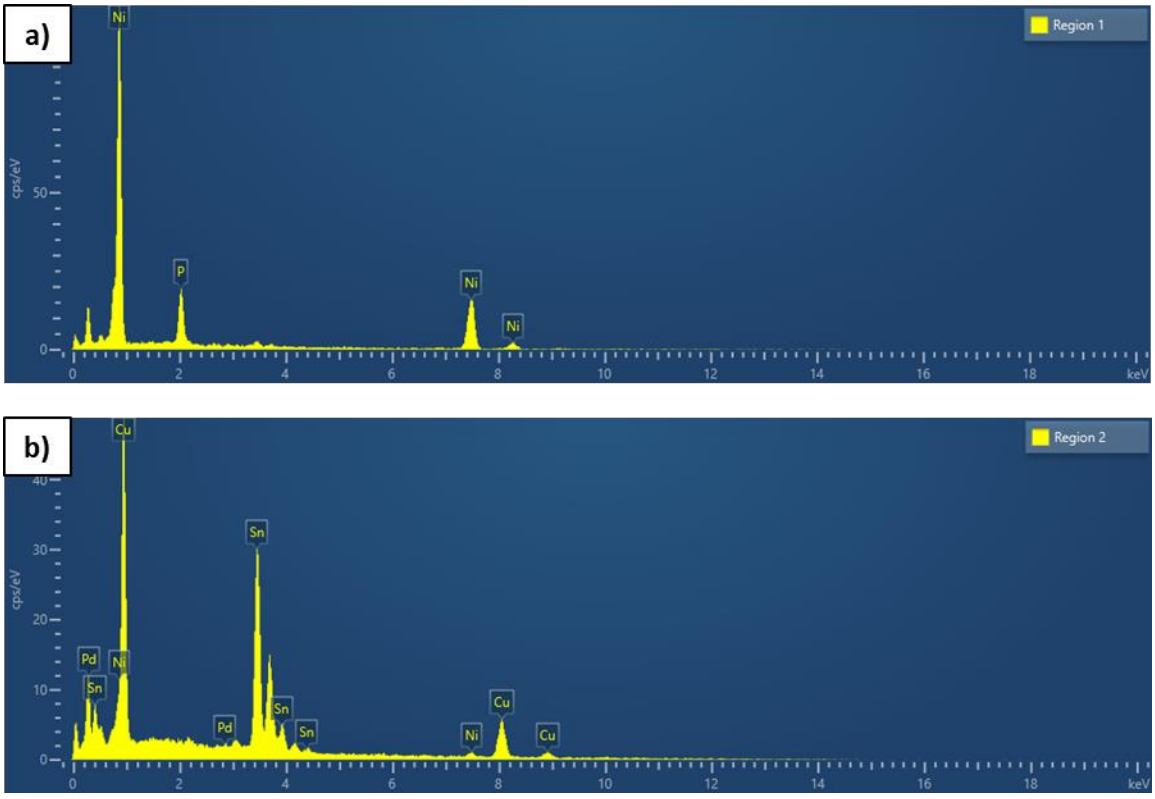

Figure 5.8: EDX spectra obtained from (a) Region 1 and (b) Region 2 in Sample 0.

Table 5.4: Region 1 EDX elemental composition.

Element	At.%
Ni	81.3
P	18.7
Total	**100.0**

Table 5.5: Region 2 EDX elemental composition.

Element	At.%
Cu	63.4
Ni	2.8
Sn	33.5
Pd	0.3
Total	**100.0**

From Figure 5.8 a) and Table 5.4, Ni and P were detected from EDX at Region 1, which suggests that Region 1 most likely consisted of the amorphous Ni-P layer. This is consistent with the observation in Figure 5.7 where Region 1 was unindexed. As EBSD is only able to index crystalline structures, amorphous phases like the Ni-P layer will remain as unindexed. Furthermore, as the substrate side pad finish was ENEPIG, the absence of Au and Pd at this region also suggested that the top-most Au and Pd layers of the ENEPIG finish, as shown in Figure 5.9, had dissolved into the molten solder in the early stages of soldering, leaving the electroless Ni-P layer exposed to the molten solder. As a result, the reaction between the molten solder and electroless Ni-P layer resulted in the formation of the $(Cu, Ni)_6Sn_5$ IMC [5].

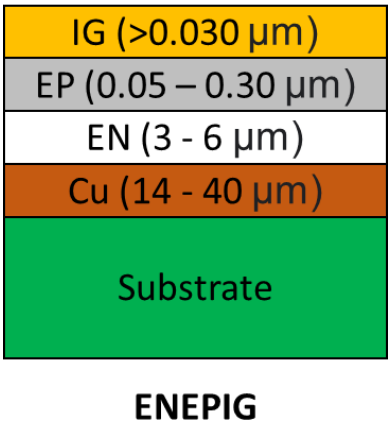

Figure 5.9: Schematic of ENEPIG configuration showing the immersion gold (IG), electroless palladium (EP), electroless nickel (EN), copper (Cu) and substrate layers [2].

However, observations from Figure 5.8 b) and Table 5.5 also showed that small amounts of Pd was detected within the $(Cu, Ni)_6Sn_5$ IMC region (Region 2). 0.3 At.% Pd was detected from EDX at Region 2. This implied that Pd had dissolved into the IMC region, eventually resulting in the formation $(Cu, Ni, Pd)_6Sn_5$. This is consistent with the observations made in the study by Tseng *et al.* (2014) where it was confirmed that in ENEPIG joints, the IMC that formed was indeed $(Cu, Ni, Pd)_6Sn_5$ as opposed to $(Cu, Ni)_6Sn_5$ [7]. The Pd layer in ENEPIG pad finishes served as the nuclei for the heterogeneous nucleation of $(Cu, Ni, Pd)_6Sn_5$. The enthalpy of formation of Pd-Cu and Pd-Sn were much greater than Pd-Ni. These greater formation enthalpies served as the driving force for Cu and Sn atoms to segregate with the Pd atoms, thus eventually forming $(Cu, Ni, Pd)_6Sn_5$.

IMCs that formed at the substrate side of interconnect joints are also known to be sensitive to the Cu concentration in the molten solder. Depending on the Cu content in the solder, the IMC formed may vary from one another. As the solder contains Cu that can contribute to the formation of the IMC at the substrate side, the use of a solder with a different concentration of Cu, such as Sn0.7Cu as compared to SAC305, might affect the IMC formation at the ENEPIG joints. Hence, the EBSD phase map and EDX spectra was obtained for Sample Z as well to compare if the slightly higher Cu content in Sn0.7Cu solder will affect the IMC formation as compared to SAC305 solder.

The EBSD phase map for Sample Z was obtained and shown in Figure 5.10. Similar to Sample 0, EDX data was also obtained at two regions of the sample, namely Region A and Region B. EDX spectra of the two regions are shown in Figure 5.11. Individual elemental composition at each of the regions are also shown in Table 5.6 and Table 5.7 respectively.

From the phase map shown in Figure 5.10, it was also observed that in Sample Z, the IMC phase that was detected at the substrate side was mainly determined as $(Cu, Ni)_6Sn_5$. Ag_3Sn particles was observed to disperse in the solder matrix as well. From the results gathered in Figure 5.11 a) and Table 5.6, Ni and P were once again detected at the unindexed region of the sample, Region A. The At% of Ni and P were 77.6 and 22.4 respectively which is relatively close in ratio to the composition of Ni and P at Region 1 of Sample 0. Hence, it

is very likely that Region A is the Ni-P layer. On the other hand, at the IMC region, Region B, the elemental composition detected was 51.2 At% Cu, 12.7 At% Ni, 35.6 At% Sn and 0.5 At% Pd. Similar to Region 2 from Sample 0, a small amount of Pd was also detected at the IMC region of Sample Z. Hence the IMC phase present was $(Cu, Ni, Pd)_6Sn_5$.

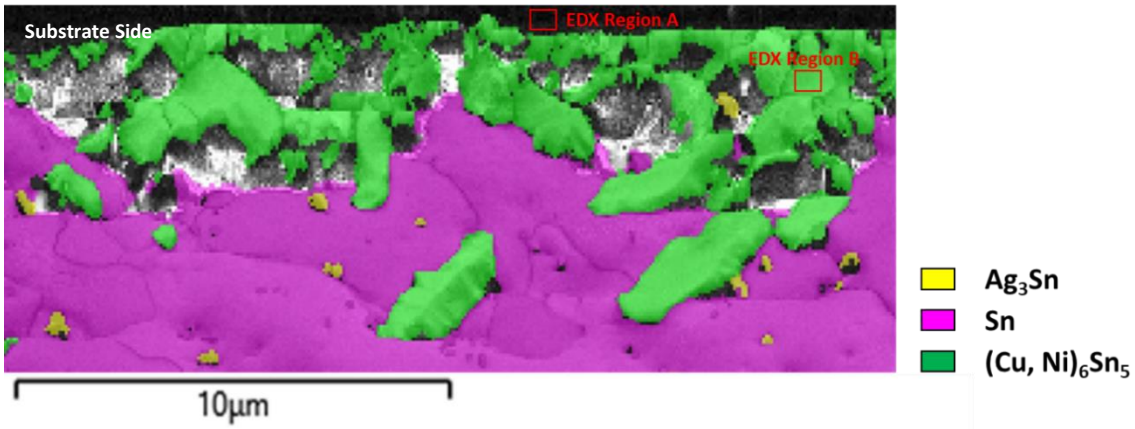

Figure 5.10: EBSD phase map of substrate side IMC showing $(Cu, Ni)_6Sn_5$ phase in Sample Z.

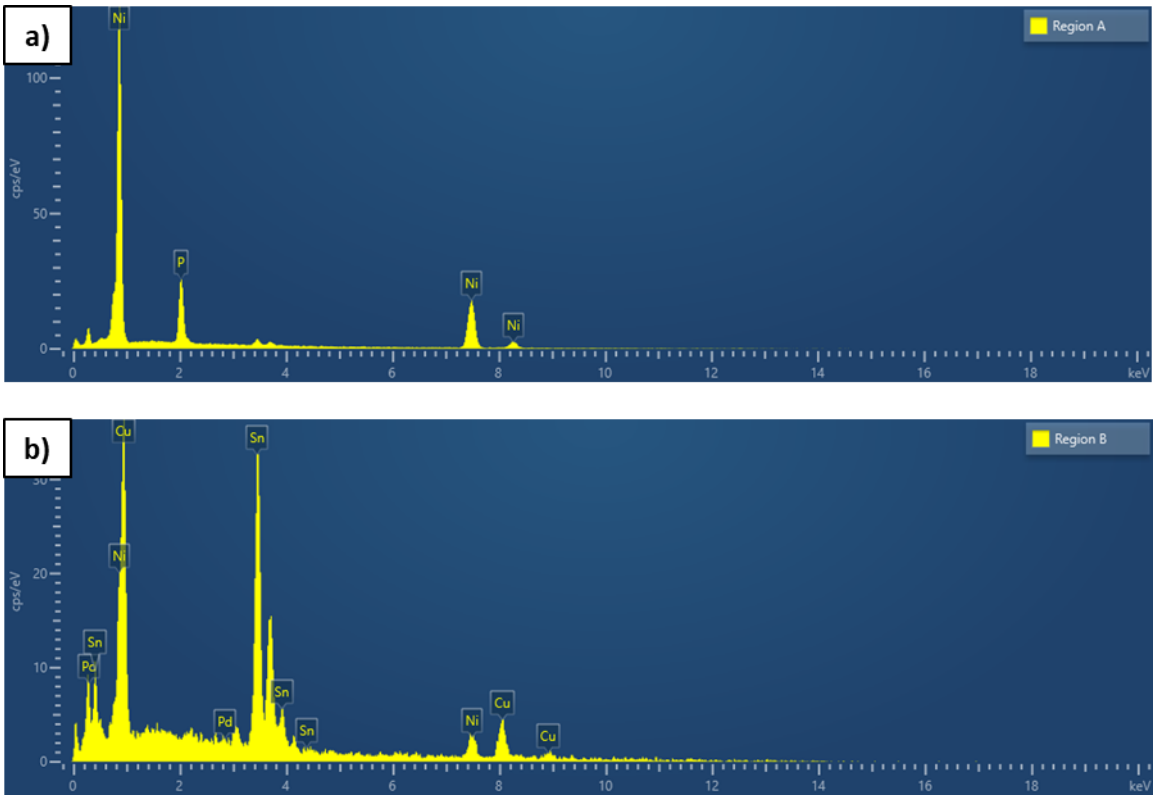

Figure 5.11: EDX spectra obtained from (a) Region A and (b) Region B in Sample Z.

Table 5.6: Region A EDX elemental composition.

Element	At.%
Ni	77.6
P	22.4
Total	**100.0**

Table 5.7: Region B EDX elemental composition.

Element	At.%
Cu	51.2
Ni	12.7
Sn	35.6
Pd	0.5
Total	**100.0**

Through the incorporation of the EDX spectra and EBSD phase mapping, the substrate side IMC observed in both Sample 0 and Sample Z was identified as $(Cu, Ni, Pd)_6Sn_5$. Another similarity observed in both samples was the absence of Cu_3Sn. This could be attributed to the presence of Ni in the IMC region as findings described from literature suggest that Ni atoms are believed to be able to suppress the formation of Cu_3Sn [8]. Ni present in the $(Cu, Ni, Pd)_6Sn_5$ IMC lowered the Gibbs free energy of the phase, which as a result increased the driving force for Sn atoms to diffuse through $(Cu, Ni, Pd)_6Sn_5$. This in turn caused more Sn atoms to diffuse towards the more thermodynamically stable $(Cu, Ni, Pd)_6Sn_5$ phase, and resulting in less of the phase decomposition to Cu_3Sn [9].

Overall, the observed IMC phases formed at the substrate side in Sample Z were similar to as those observed in Sample 0. Therefore, it can be seen that although Sn0.7Cu solder had a slightly higher Cu content of 0.7 Wt.% as compared to SAC305 solder of 0.5 Wt.% Cu, there were no significant differences in the IMC formation after soldering.

5.6 IMC Grain Orientation Comparison - SAC305 vs Sn0.7Cu at Time = 0

From the earlier study of the substrate side IMC phase, it was identified that the IMC present was $(Cu, Ni, Pd)_6Sn_5$. Although it was observed that the same IMC phase was present in both SAC305 and Sn0.7Cu substrate solder samples, it was not known how the crystallographic structure of the IMC may differ between the two solders of Sample 0 and Sample Z. Hence, to gain more insight into the crystallographic structure of the samples, crystal orientation maps were also obtained from EBSD in addition to the phase maps.

The grain orientation map or inverse pole figure (IPF) map of the substrate side IMC region was obtained and shown in Figure 5.12 and Figure 5.13 for Sample 0 and Sample Z respectively.

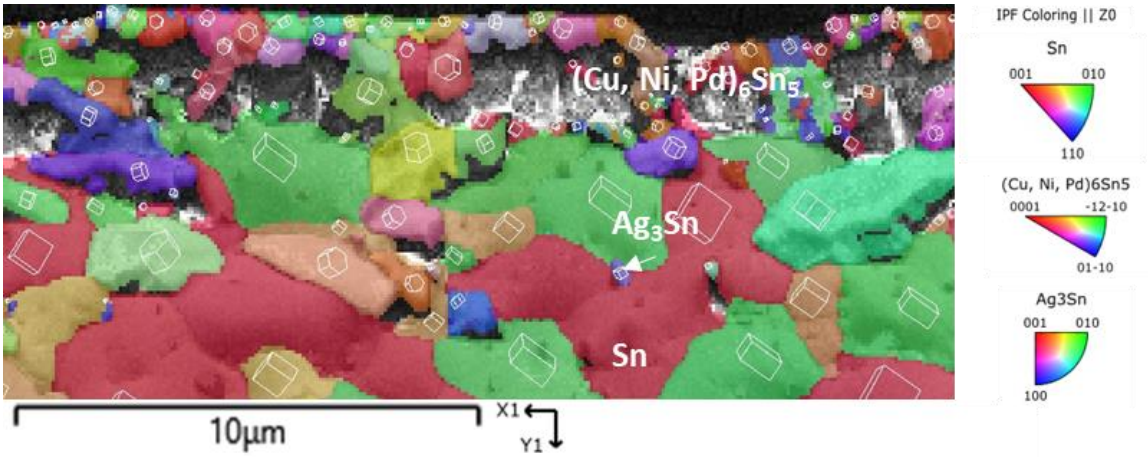

Figure 5.12: IPF-Z map of substrate side IMC showing randomly orientated $(Cu, Ni, Pd)_6Sn_5$ grains in Sample 0.

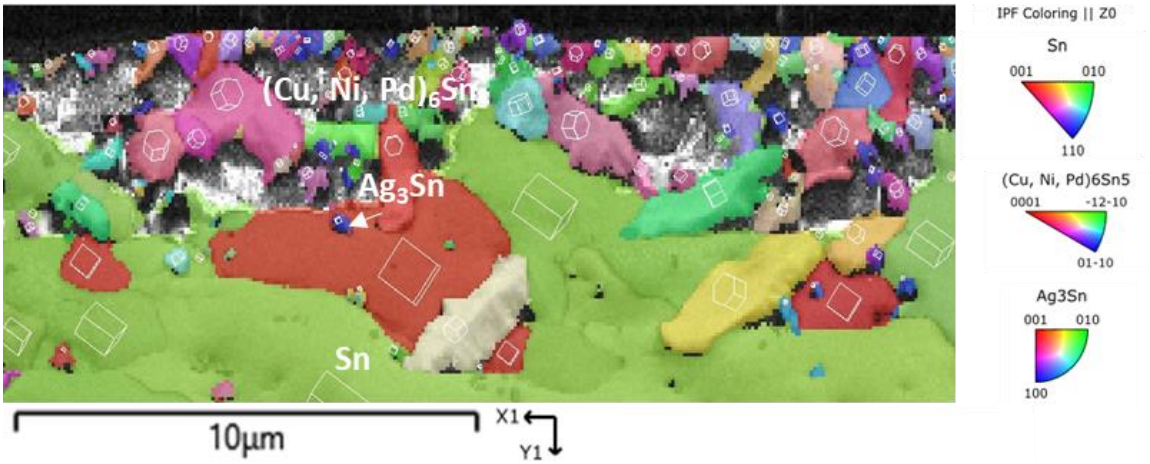

Figure 5.13: IPF-Z map of substrate side IMC showing randomly orientated (Cu, Ni, Pd)$_6$Sn$_5$ grains in Sample Z.

Studies have shown that generally hexagonal Cu$_6$Sn$_5$ IMC grains grow along the [0001] direction (or *c*-axis) of the unit cell, suggesting a strong preference where the crystal *c*-axis is orientated along the direction of the IMC growth. Even with the presence of Ni in (Cu, Ni)$_6$Sn$_5$, grain growth orientation was not significantly deviated from Cu$_6$Sn$_5$ [6]. (Cu, Ni)$_6$Sn$_5$ too grew with a preferred orientation with only slight deviations and the (0001) plane of the (Cu, Ni)$_6$Sn$_5$ grains are typically parallel to the substrate as illustrated by Figure 5.14.

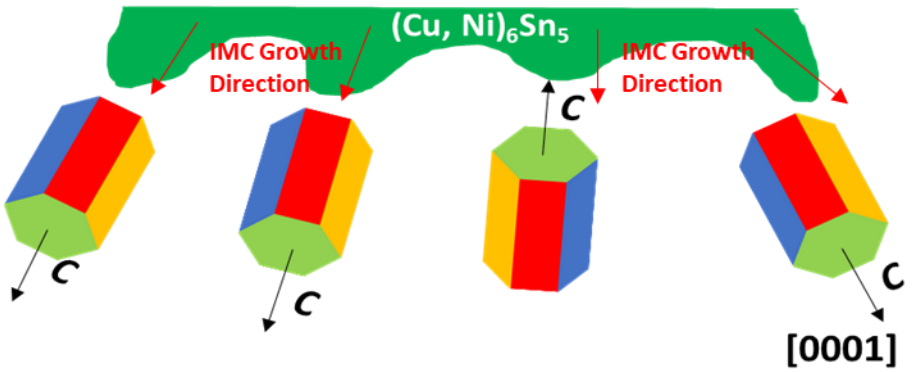

Figure 5.14: Schematic illustration of preferred crystallographic orientation of (Cu, Ni)$_6$Sn$_5$ where *c*-axis of the crystal tends to be parallel with the IMC growth direction.

Hence, it was thought that the (Cu, Ni, Pd)$_6$Sn$_5$ IMC grains in Sample 0 and Sample Z would have the same observations of preferred grain orientation where the grains grew with the *c*-axis along the growth direction. However, from the IPF maps obtained for Sample 0 and Sample Z in Figure 5.12 and Figure 5.13 respectively, the (Cu, Ni, Pd)$_6$Sn$_5$ IMC grains were observed to be mapped in a wide variety of different colors. As the different colors of each grain represent a different crystal orientation, this showed that IMC grains of (Cu, Ni, Pd)$_6$Sn$_5$ were randomly orientated with no orientation preference. This was further supported by the (0001) pole figures shown in Figure 5.15 and Figure 5.16, where various spots were observed to be distributed across the pole figure. This deviation from the expected outcome of a preferred orientation could be due to the presence of Pd in the IMC. Findings from literature have suggested that the presence of Pd in (Cu, Ni, Pd)$_6$Sn$_5$ can affect the texture of the IMC [7]. The presence of Pd lowered the surface tension between the (Cu, Ni, Pd)$_6$Sn$_5$ IMC and the solder. This subsequently enhanced the nucleation of (Cu, Ni, Pd)$_6$Sn$_5$ and as a result, caused the (Cu, Ni, Pd)$_6$Sn$_5$ IMC to grow with an elongated grain morphology that was also observed in both Sample 0 and Sample Z. The enhanced heterogeneous nucleation in the ENEPIG joints thus also resulted in the randomly orientated grains of the (Cu, Ni, Pd)$_6$Sn$_5$ IMC.

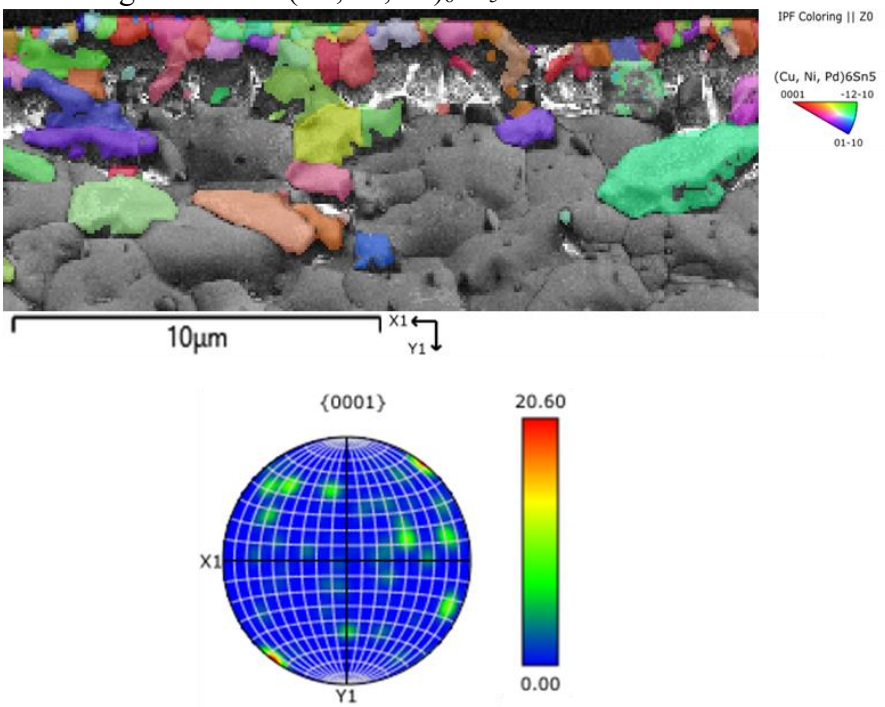

Figure 5.15: IPF-Z map of substrate side (Cu, Ni, Pd)$_6$Sn$_5$ IMC and (0001) pole figure showing randomly orientated (Cu, Ni, Pd)$_6$Sn$_5$ grains in Sample 0.

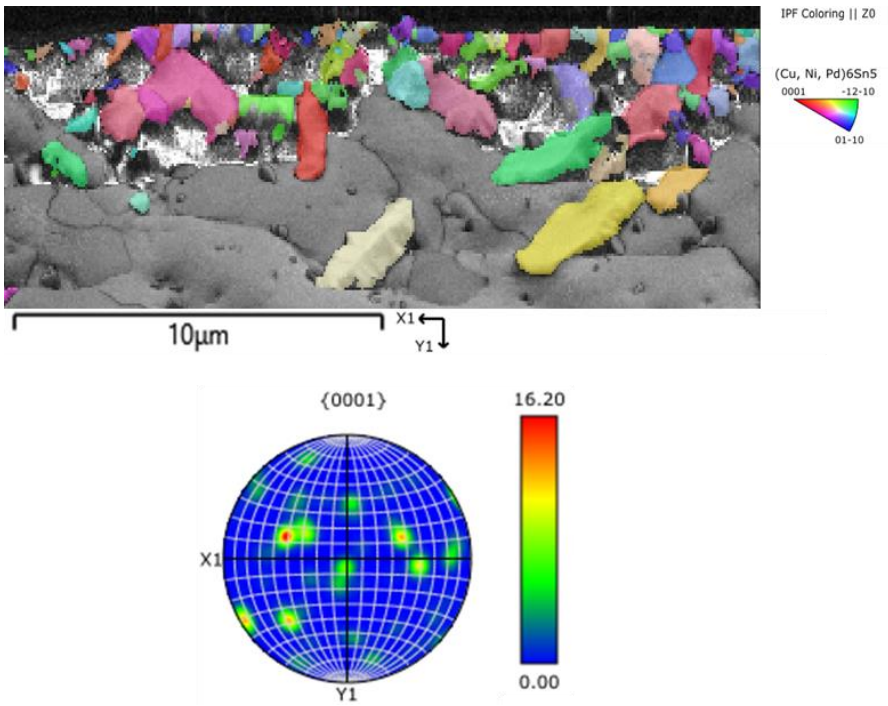

Figure 5.16: IPF-Z map of substrate side (Cu, Ni, Pd)$_6$Sn$_5$ IMC and (0001) pole figure showing randomly orientated (Cu, Ni, Pd)$_6$Sn$_5$ grains in Sample Z.

As observed in Figure 5.15 and Figure 5.16, a random grain orientation texture dominated the (Cu, Ni, Pd)$_6$Sn$_5$ IMC growth. Earlier, it was mentioned that Cu_6Sn_5 IMC grains grew with a strong preferred orientation with the [0001] direction (or *c*-axis) along the growth direction. Hence, the (0001) plane of the Cu_6Sn_5 grains tend to be parallel to the IMC interface. The (0001) plane of hexagonal Cu_6Sn_5 is known for cracks to readily initiate due to it being a basal slip plane [10]. Any cracks that form tends to propagate easily through this (0001) slip plane. In a related study by Yang *et al.* (2014), it was reported that in the (Cu, Ni)$_6$Sn$_5$ IMC, the grains generally grew with $(10\bar{1}0)$ planes parallel to the substrate as opposed to Cu_6Sn_5. As such, it became more difficult for cracks to propagate through the IMC as the path became less direct [9]. Therefore in (Cu, Ni, Pd)$_6$Sn$_5$, the random grain texture would be expected to hinder crack propagation through the (0001) plane even more effectively, resulting in stronger mechanical strength.

Through the study of the grain orientations in Sample 0 and Sample Z, no significant differences were observed between the two samples as well. However, to be able to provide more confidence that the higher Cu content in Sn0.7Cu was not significant enough to drastically affect the reliability of the IMC formed at the substrate side, further comparisons of the IMC phase were made at conditions much closer to the working environment.

5.7 Effects of Temperature Cycling on IMC

To study the effects of temperature cycling on the substrate side IMC of Sn0.7Cu solder against SAC305 solder, EBSD phase maps were collected at different temperature cycling conditions, namely at TCG 1200 cycles and at TCG 2000 cycles. Comparing with the respective solders at T=0 conditions, the phase maps for the SAC305 solder Sample 0 (T=0), Sample 1 (1200 cycles) and Sample 2 (2000 cycles) as well as Sn0.7Cu solder Sample Z (T=0), Sample A (1200 cycles) and Sample B (2000 cycles) were obtained and are as shown in Figure 5.17 and Figure 5.18 respectively.

EDX spectrum was also collected at the IMC regions of Sample 1, Sample 2, Sample A and Sample B (Region 3, Region 4, Region C and Region D respectively) to determine the elemental composition at those IMC positions. The EDX spectrum for the four samples were as shown in Figure 5.19 and the elemental compositions at each region were as shown in Tables 5.8 to Table 5.11.

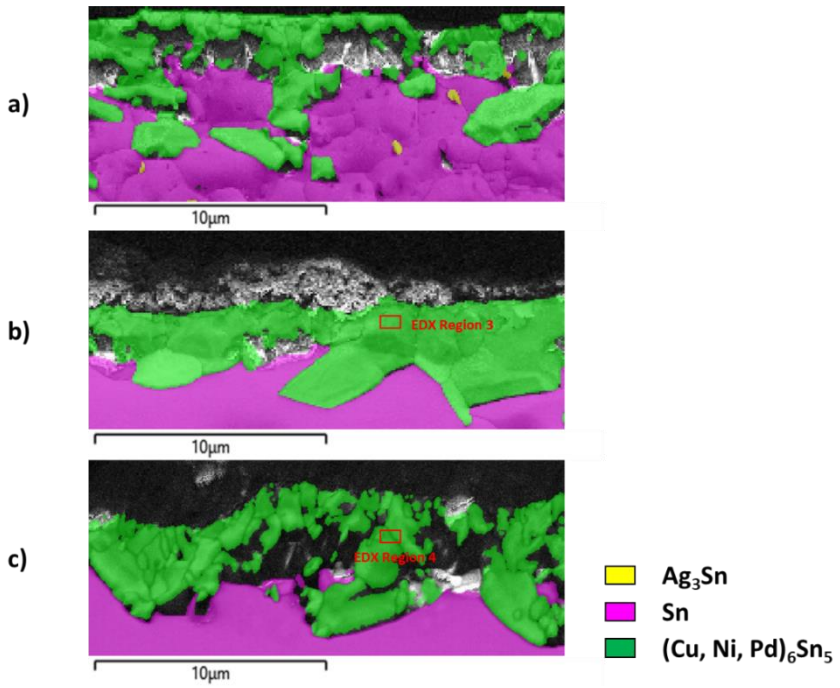

Figure 5.17: Phase map of substrate side IMC showing $(Cu, Ni, Pd)_6Sn_5$ phase in (a) Sample 0, (b) Sample 1 and (c) Sample 2.

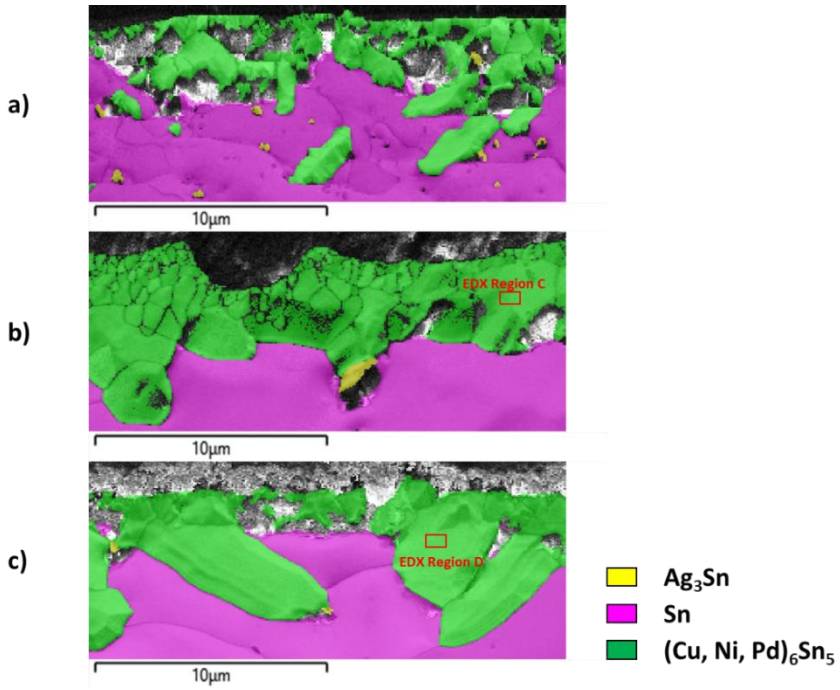

Figure 5.18: Phase map of substrate side IMC showing $(Cu, Ni, Pd)_6Sn_5$ phase in (a) Sample Z, (b) Sample A and (c) Sample B.

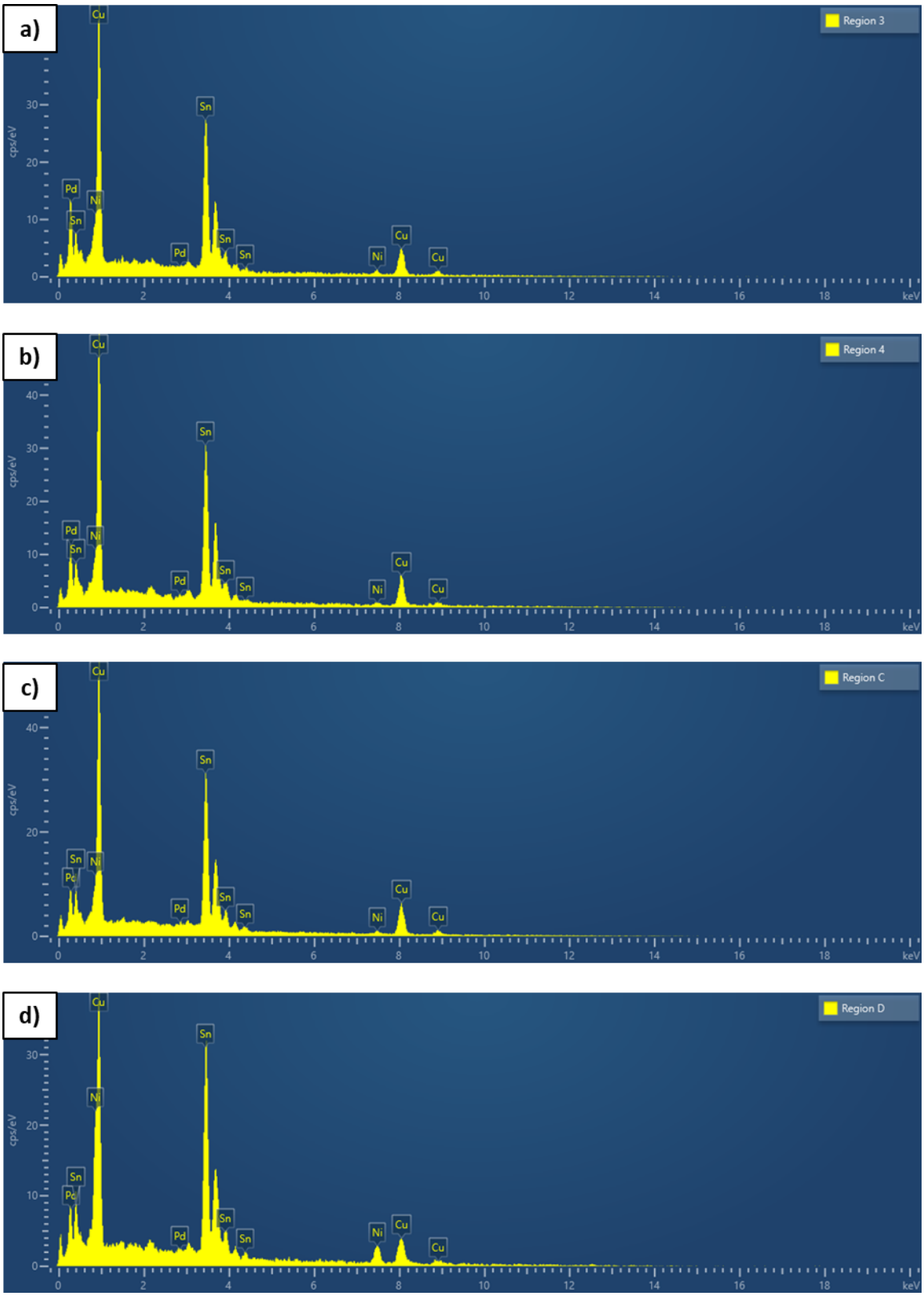

Figure 5.19: EDX spectra from (a) Region 3, (b) Region 4, (c) Region C and (d) Region D.

Table 5.8: Region 3 EDX elemental composition.

Element	At.%
Cu	48.1
Ni	17.4
Sn	34.3
Pd	0.2
Total	**100.0**

Table 5.9: Region 4 EDX elemental composition.

Element	At.%
Cu	64.5
Ni	2.6
Sn	32.4
Pd	0.5
Total	**100.0**

Table 5.10: Region C EDX elemental composition.

Element	At.%
Cu	63.9
Ni	2.1
Sn	33.6
Pd	0.4
Total	**100.0**

Table 5.11: Region D EDX elemental composition.

Element	At.%
Cu	53.3
Ni	13.0
Sn	33.1
Pd	0.6
Total	**100.0**

For the SAC305 substrate solder Samples 1 and 2, as observed from Figure 5.19 a) and b) as well as Table 5.8 and Table 5.9, a small amount of Pd was also detected from EDX. Overall ratio of (Cu, Ni, Pd) to Sn in both Samples 1 and 2 did not deviate much from the T = 0 samples at approximately 67.0 At.% to 33.0 At.%. By incorporating this EDX data together with the earlier findings from the T = 0 samples, it was determined from EBSD phase map that the IMC present was also $(Cu, Ni, Pd)_6Sn_5$, similar to Sample 0, as shown in Figure 5.17. This indicates that no significant difference was observed in terms of the identity of the IMC that is present after temperature cycling. The same observation was made as well for the Sn0.7Cu substrate solder Samples A and B, as shown form the EDX data from Figure 5.19 c) and d) as well as Table 5.10 and Table 5.11. A small amount of Pd was also detected within the IMC region in addition to (Cu, Ni, Pd) and Sn having compositions of approximately 67.0 At.% to 33.0 At.% as well, forming $(Cu, Ni, Pd)_6Sn_5$ IMC.

Figure 5.20 shows the grain crystallographic orientation maps for Sample 0, Sample 1 and Sample 2. Comparison of the three samples was done to study if there is any texture evolution during temperature cycling. However, observations from the grain crystallographic orientation maps of the samples before and after temperature cycling showed no significant changes in the grain orientations. Even after temperature cycling, the $(Cu, Ni, Pd)_6Sn_5$ IMC grains remained randomly distributed. The average IMC thickness of the samples were measured as well, and the results are as shown in Figure 5.21. It was observed that with the increasing number of temperature cycles, the $(Cu, Ni, Pd)_6Sn_5$ IMC layer gradually grew and thickened from an average thickness of 2.92 μm at T=0 to the average thickness of 4.97 μm after 2000 cycles.

The grain crystallographic orientation maps for Sample Z, Sample A and Sample B were also obtained as shown in Figure 5.22. The average IMC thickness of the samples were also measured and are as shown in Figure 5.23. As the number of temperature cycles increased from T=0 to 2000 cycles, the average thickness of the $(Cu, Ni, Pd)_6Sn_5$ IMC layer was observed to increase from 3.27 μm to 5.04 μm.

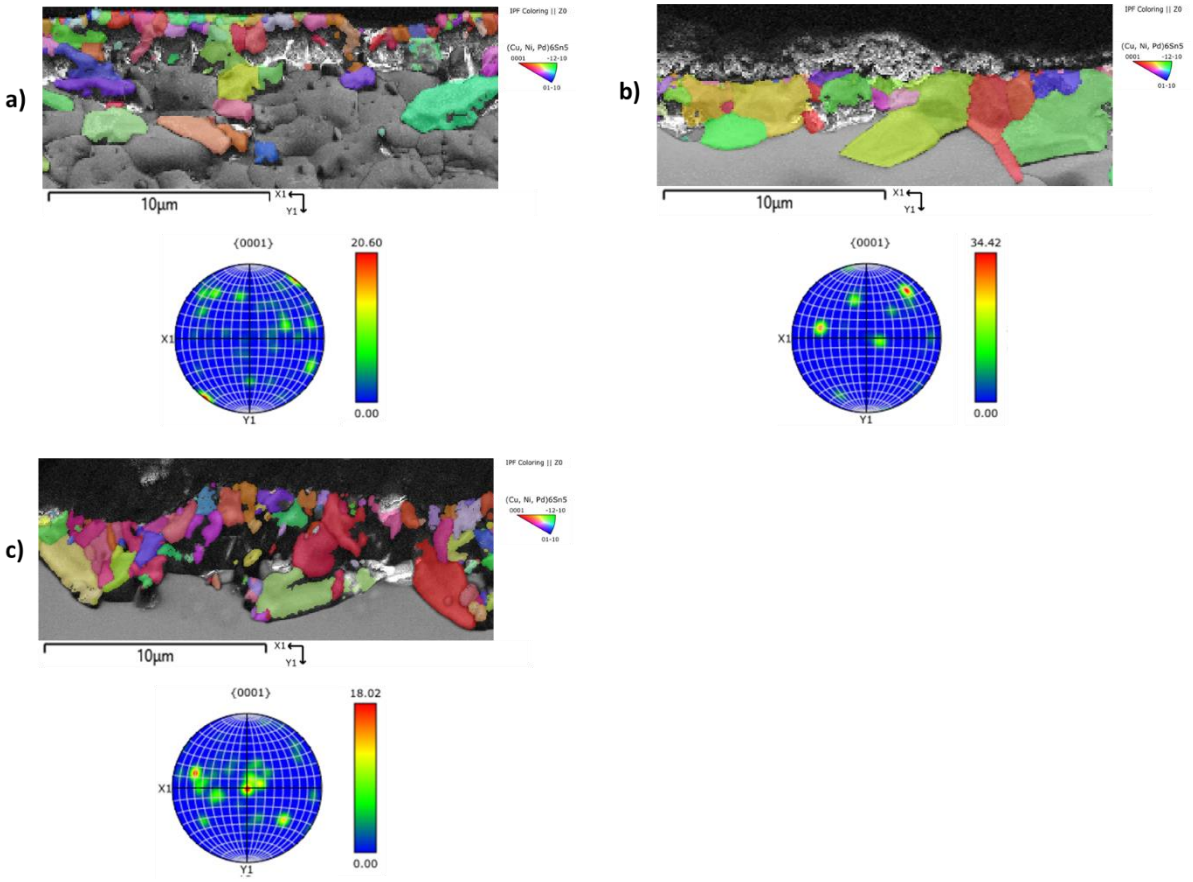

Figure 5.20: IPF-Z map of substrate side (Cu, Ni, Pd)$_6$Sn$_5$ IMC and (0001) pole figure showing randomly orientated (Cu, Ni, Pd)$_6$Sn$_5$ grains in (a) Sample 0, (b) Sample 1 and (c) Sample 2.

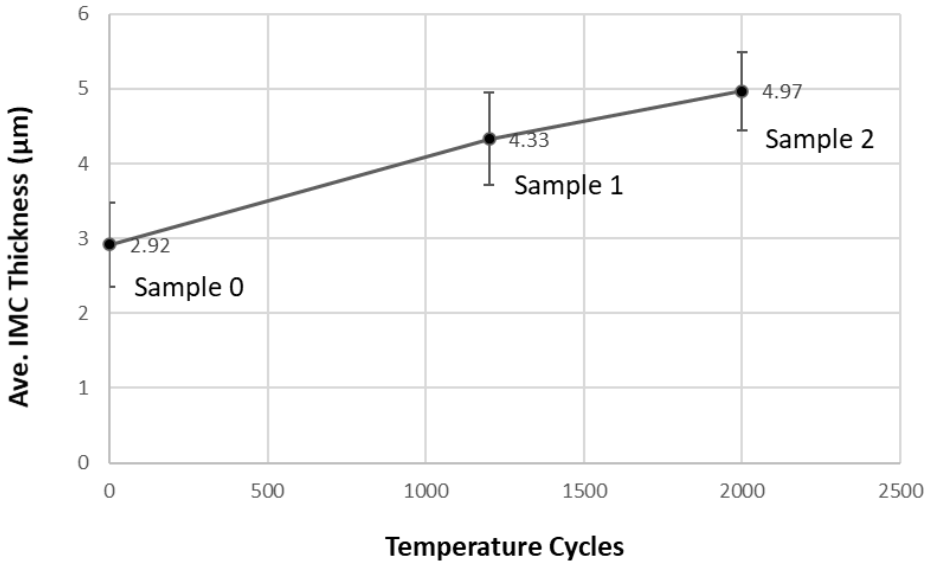

Figure 5.21: Average IMC thickness plotted against number of temperature cycles.

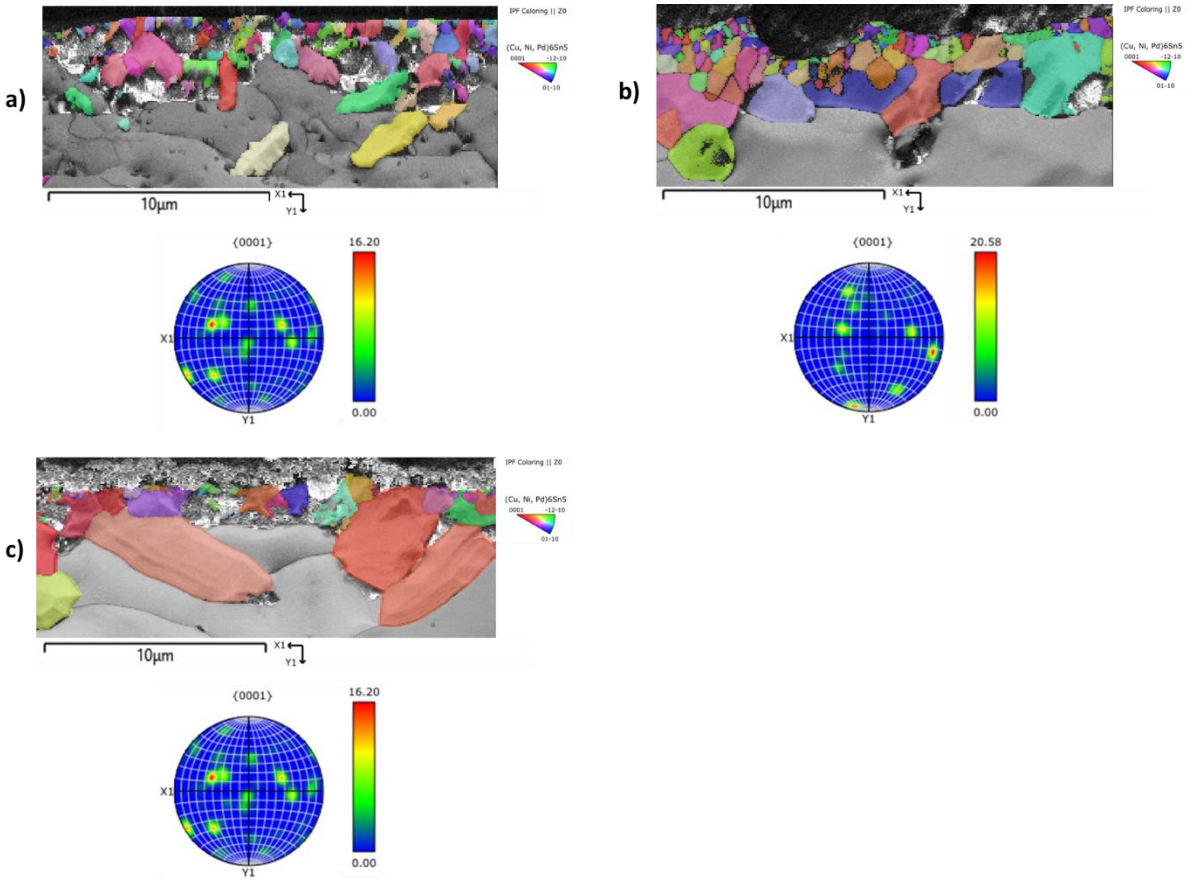

Figure 5.22: IPF-Z map of substrate side (Cu, Ni, Pd)$_6$Sn$_5$ IMC and (0001) pole figure showing randomly orientated (Cu, Ni, Pd)$_6$Sn$_5$ grains in (a) Sample Z, (b) Sample A and (c) Sample B.

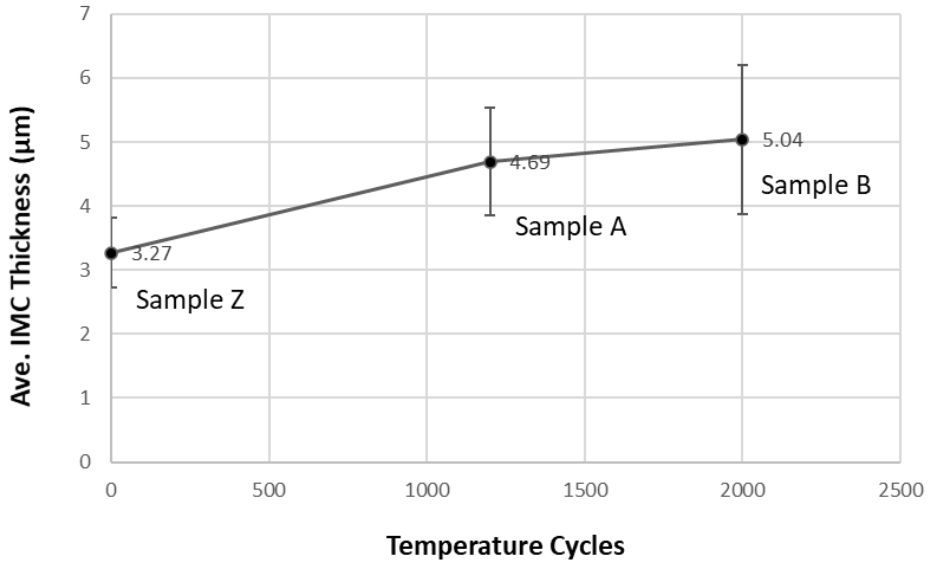

Figure 5.23: Average IMC thickness plotted against number of temperature cycles.

Overall, in both SAC305 and Sn0.7Cu substrate solder samples after thermal cycling, it was observed that there was an increase in the substrate side IMC thickness in both samples. Although there are few studies from literature that evaluate on the IMC growth as a function of temperature cycling, it was known that temperature and time played a part in the IMC growth during temperature cycling. It was suggested that the growth of the IMC can be represented by equation 5.1 as shown below [12]:

$$X - X_0 = 1.78 \times 10^{-2} t^{0.52} e^{(-57700/RT)} \quad (5.1)$$

where X = total IMC thickness after temperature cycling

X_0 = initial IMC thickness before temperature cycling

t = dwell time in seconds (s)

R = gas constant, 8.314 J/mol K

T = temperature in Kelvin (K)

Under TCG conditions, the samples were cycled at temperatures from -40 ºC to 125 ºC. Hence, from equation 5.1, it can be shown that for a fixed dwell time at the lowest temperature of -40 ºC, the IMC growth ($X - X_0$) was very low as compared to the IMC growth at the highest temperature of 125 ºC. This was consistent with the observations reported by Pan *et al.* (2009), where it was explained by the fact that at the peak temperature, Cu dissolved much faster which resulted in the formation of more IMC [12]. Therefore, it can be seen that the growth rate of IMC thickness was mainly determined by the dwell time and higher temperatures during thermal cycling and that it was not significantly affected by the amount of Cu content in the solder. In this study as the samples were subjected to the same TCG conditions, the temperature factor remains constant. Hence, the IMC growth can simply be approximated against time as equation 5.2.

$$(X - X_0) \propto \sqrt{t} \quad (5.2)$$

This was further supported by the average IMC thickness trend observed in Figure 5.21 and Figure 5.23, where a larger average IMC thickness was observed after TCG 2000 cycles as compared to 1200 cycles. In addition, comparison of the average IMC thickness between the SAC305 substrate solder Sample 2 and Sn0.7Cu substrate solder Sample B, determined that after TCG 2000 cycles, the average IMC thickness at the substrate side was determined to be 4.97 μm and 5.04 μm respectively. This difference in average IMC thickness between the two samples was only 0.07 μm which was not a very significant increase, which supports that the IMC growth rate is independent of Cu content.

There is another similar trend between the SAC305 and Sn0.7Cu substrate solder samples. From Figure 5.21, it was observed that as the number of temperature cycles increased from 1200 to 2000 cycles, the gradient of the plot decreased, which suggested that the IMC growth rate decreased with increasing temperature cycles. The same trend was also observed from Figure 5.23, where the IMC growth rate decreased as the number of temperature cycles increased. This decreasing IMC growth rate was because right at the start of temperature cycling, the IMC layer was thin. This allowed more Cu and Sn atoms from solder and Ni atoms from the ENEPIG substrate to diffuse across the interfacial IMC layer very quickly to form more IMCs. As the IMC gradually thickened through the course of temperature cycling, the diffusion of the Cu, Sn and Ni atoms will also become increasingly obstructed. This eventually resulted in the decrease of IMC growth rate [13].

5.8 Effects of High Temperature Storage on IMC

In addition to temperature cycling, to study the effects of high temperature storage (HTS) on the substrate side IMC of Sn0.7Cu solder against SAC305 solder, EBSD phase and orientation maps were obtained from samples subjected to different HTS conditions, such as at 1000 hours and at 2000 hours. The phase maps for the SAC305 solder Sample 0 (T=0), Sample 3 (1000 hours) and Sample 4 (2000 hours) as well as Sn0.7Cu solder Sample Z (T=0), Sample C (1000 hours) and Sample D (2000 hours) were obtained and is as shown respectively in Figure 5.24 and Figure 5.25 respectively.

From Figure 5.24 and Figure 5.25, it was observed that in both the SAC305 and Sn0.7Cu solder samples, the substrate side IMC present was (Cu, Ni, Pd)$_6$Sn$_5$. The IMC phase was determined after incorporating the EDX results that were obtained in the study of the temperature cycling units into the EBSD phase map. Similar to the temperature cycling samples, no Cu$_3$Sn was detected as well in all HTS samples. In general, no significant changes were observed in terms of the IMC formed after HTS as compared to temperature cycling. Figure 5.26 shows the grain crystallographic orientation maps for Sample 0, Sample 3 and Sample 4. Observations from the grain crystallographic orientation maps of the samples before and after HTS showed no significant changes in the grain orientations as well, with the (Cu, Ni, Pd)$_6$Sn$_5$ IMC grains remaining randomly distributed. The average IMC thickness of the samples were measured, and the results are as shown in Figure 5.27. It was observed that the (Cu, Ni, Pd)$_6$Sn$_5$ IMC increased from an average thickness of 2.92 μm at T=0 to the average thickness of 6.43 μm after HTS 2000 hours. The grain crystallographic orientation maps for Sample Z, Sample C and Sample D are obtained as shown in Figure 5.28. The measured average IMC thickness of the samples are shown in Figure 5.29. Similar to the SAC305 solder samples, the average thickness of the (Cu, Ni, Pd)$_6$Sn$_5$ IMC was observed to increase from 3.27 μm to 6.59 μm after HTS 2000 hours.

Overall, from the data collected, in both SAC305 and Sn0.7Cu solder samples, it was generally observed that the average IMC thickness increased with aging time. Consistent with the observations reported by Sun *et al.* (2008), this growth in the IMC thickness was promoted by HTS and can be attributed to the diffusion of Cu from the solder with time [14-15]. In addition, as demonstrated by the results of the TCG samples and HTS samples, it was observed that the average IMC thickness was larger in the HTS samples as compared to TCG samples. In the case of the IMC thickness under HTS conditions, the larger average IMC thickness was to be expected due to the longer exposure time to high temperature, as compared to TCG where exposure to the high temperature end was much shorter [16]. This larger increase in average IMC thickness observed in the HTS samples was a result of the prolonged exposure to high temperatures, which resulted in the grain growth. A measure of the average grain sizes for Sample Z, Sample C and Sample D as shown in Figure 5.30 supported this reasoning. As observed from Figure 5.30, the average grain size, measured

in equivalent circle diameter, increased from 2.31 µm at T=0 to 5.35 µm after HTS 2000 hours.

Furthermore, it was reported in literature that the presence of Pd can affect the behavior of the grain growth in the IMC. As reported by Tseng *et al.* (2014), Pd is able to limit the IMC growth by trapping Cu atoms among solder. This subsequently will further impede more Cu from diffusing towards the IMC interface, limiting its growth and thickness [7]. The depressed Cu diffusion was also be expected to suppress the nucleation of new IMC grains in $(Cu, Ni, Pd)_6Sn_5$. Hence, with a reduced grain nucleation, the grain growth experienced under HTS conditions would be dominated by the coarsening of $(Cu, Ni, Pd)_6Sn_5$, where the smaller grains merged with the larger and more stable grains.

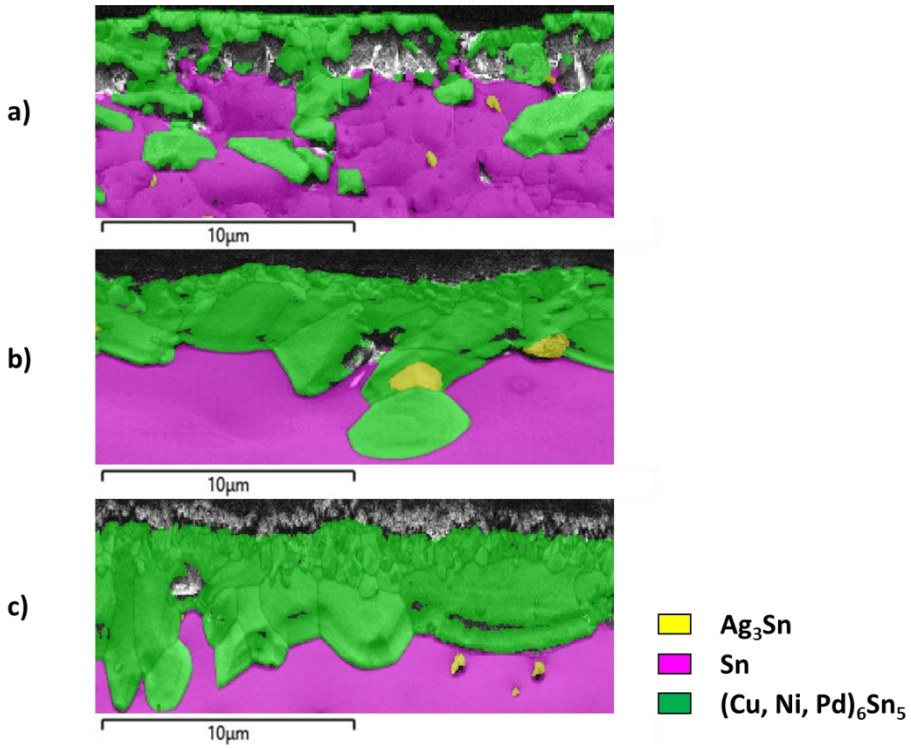

Figure 5.24: Phase map of substrate side IMC showing $(Cu, Ni, Pd)_6Sn_5$ phase in (a) Sample 0, (b) Sample 3 and (c) Sample 4.

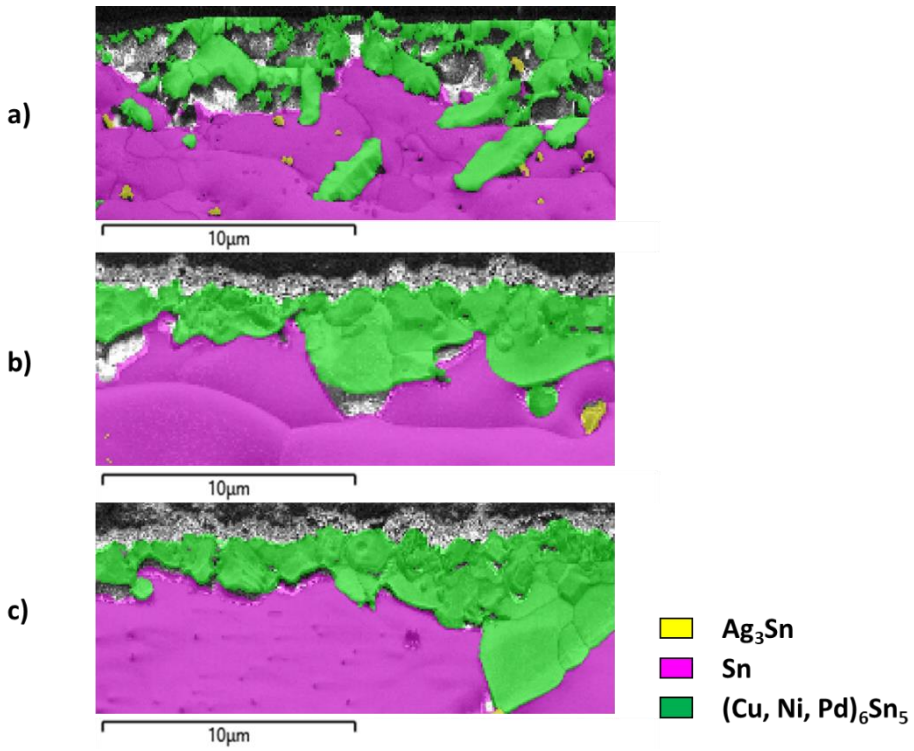

Figure 5.25: Phase map of substrate side IMC showing $(Cu, Ni, Pd)_6Sn_5$ phase in (a) Sample Z, (b) Sample C and (c) Sample D.

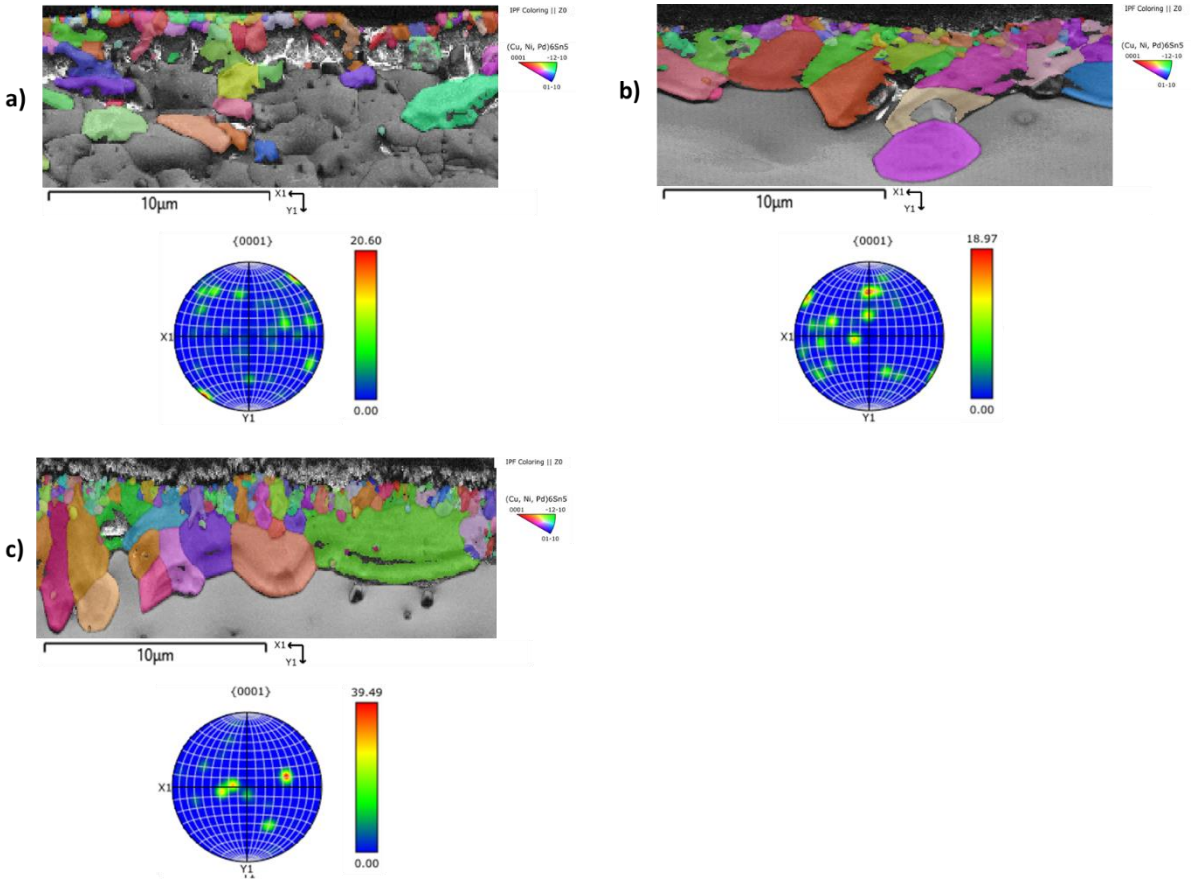

Figure 5.26: IPF-Z map of substrate side (Cu, Ni, Pd)$_6$Sn$_5$ IMC and (0001) pole figure showing randomly orientated (Cu, Ni, Pd)$_6$Sn$_5$ grains in (a) Sample 0, (b) Sample 3 and (c) Sample 4.

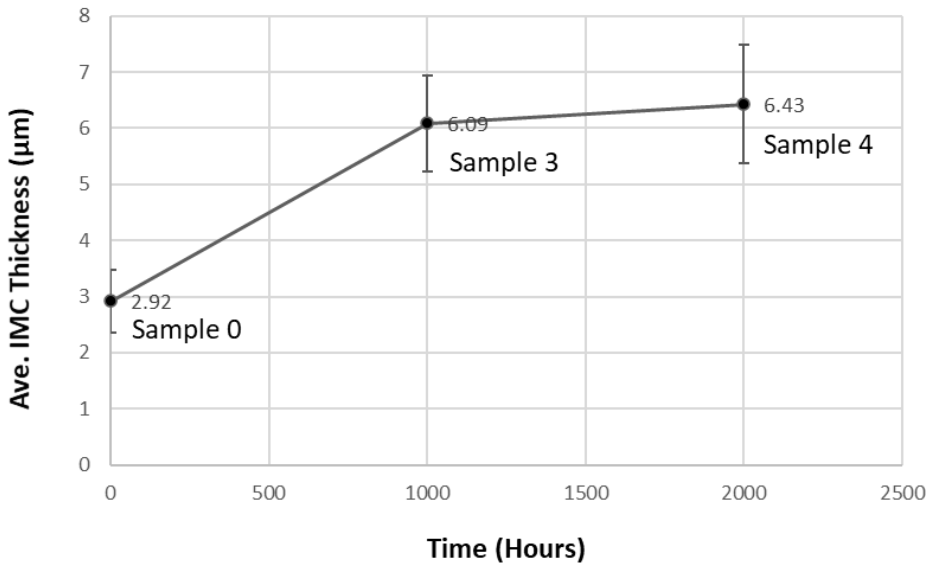

Figure 5.27: Average IMC thickness plotted against number of HTS hours.

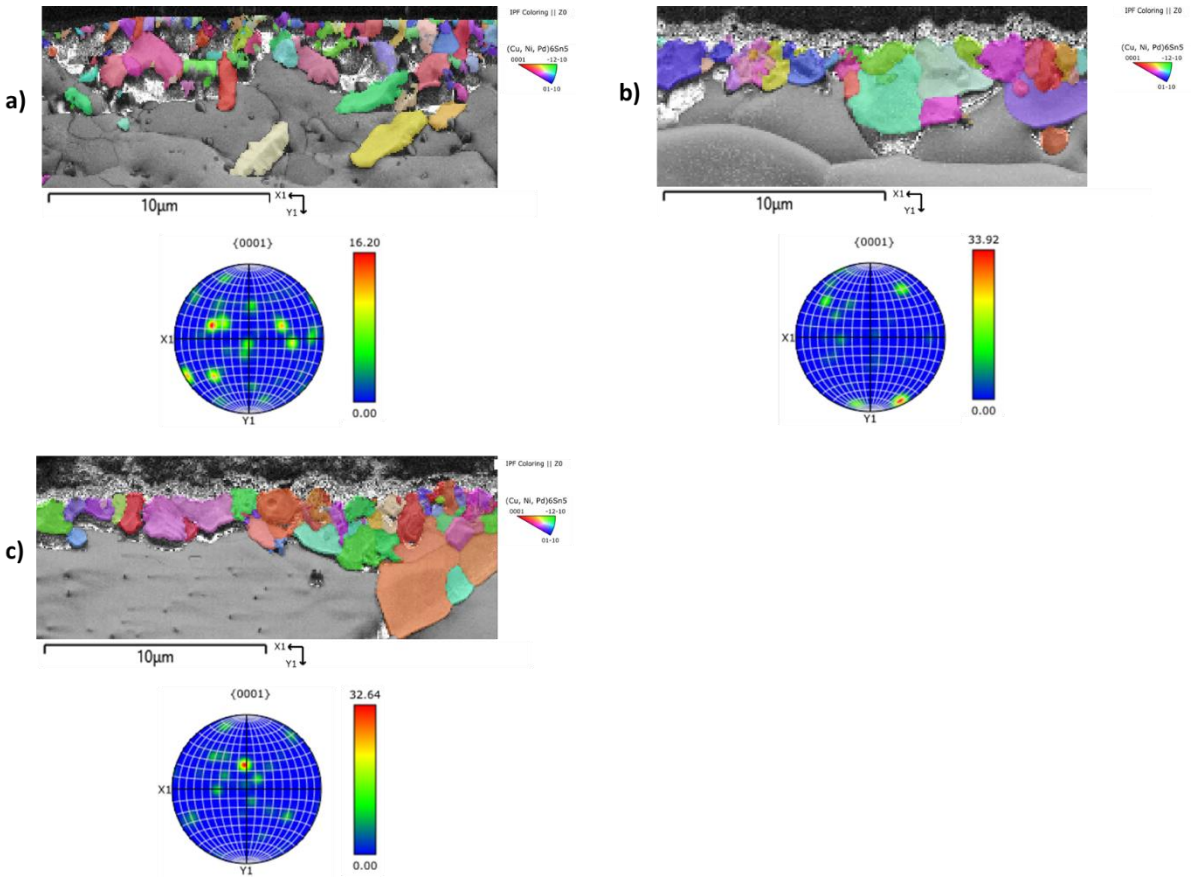

Figure 5.28: IPF-Z map of substrate side $(Cu, Ni, Pd)_6Sn_5$ IMC and (0001) pole figure showing randomly orientated $(Cu, Ni, Pd)_6Sn_5$ grains in (a) Sample Z, (b) Sample C and (c) Sample D.

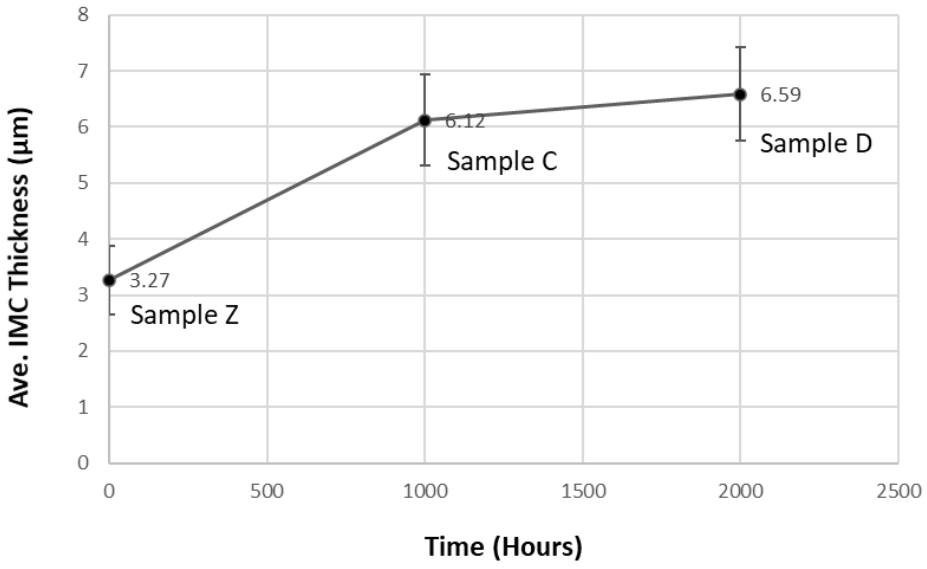

Figure 5.29: Average IMC thickness plotted against number of HTS hours.

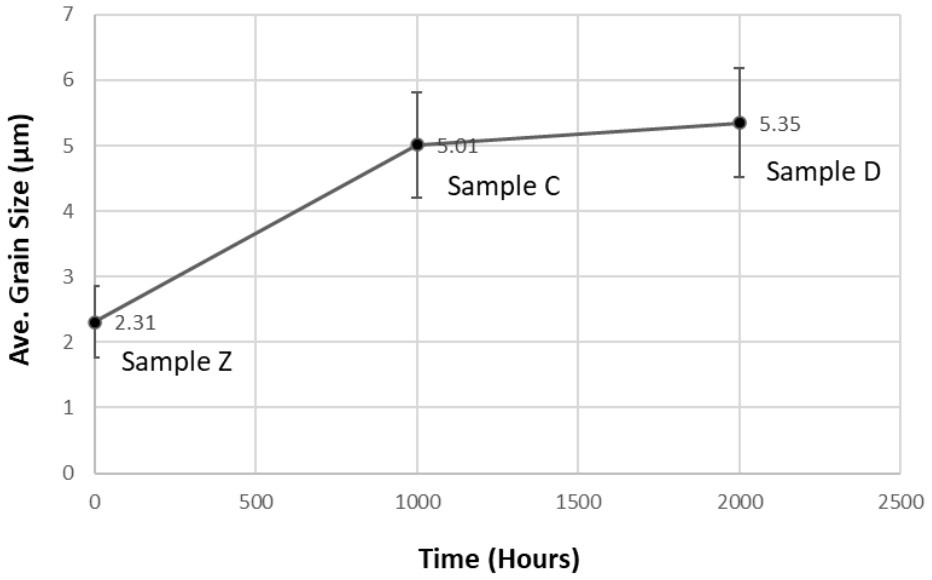

Figure 5.30: Average IMC grain size plotted against number of HTS hours.

In summary, EBSD and EDX analysis on the grain structure of the SAC305 and Sn0.7Cu substrate solder samples revealed that there were no significant differences in the IMC phases that formed at the substrate side of each type of solder sample. Furthermore, the $(Cu, Ni, Pd)_6Sn_5$ IMC that formed in both substrate solder samples showed no significant differences in terms of IMC thickness between using SAC305 and Sn0.7Cu solder. The use of either solders also exhibited the desired random grain orientations in the $(Cu, Ni, Pd)_6Sn_5$ IMC that aids in inhibiting crack propagation. Similarly, under TCG and HTS conditions, no significant differences were observed in IMC thickness, chemical composition and grain orientation between the SAC305 and Sn0.7Cu samples, concluding that Sn0.7Cu solder is a viable alternative to SAC305 solder in mitigating ILD cracks and delamination.

This was further supported by Finite Element Analysis (FEA) simulation done internally in AMD. Due to confidentiality of information, details of the FEA simulation will not be discussed in this thesis. The findings obtained determined that with the use of Sn0.7Cu solder, there was a significant decrease in ELK stress of about 30% as compared to SAC305 solder, shown in Table 5.12. This is expected to result in significant improvements in terms of ELK defects like cracks or delamination.

Table 5.12: FEA simulation results.

	SAC305	**Sn0.7Cu**
ELK Stress Ratio	1	0.69

References

[1] M. T. Rad, G. Boussinot, "Dynamics of Grain Boundary Premelting", *Scientific Reports*, 2020, Vol.10(21074)

[2] H. L. J. Pang, K. H. Tan, X. Q. Shi, Z. P. Wang, "Microstructure and Intermetallic Growth Effects on Shear and Fatigue Strength of Solder Joints Subjected to thermal Cycling Aging", Materials Science & Engineering. A. Structural Materials: Properties, Microstructure and Processing, 2001, Vol.307(1), pp. 42-50

[3] K. Nogita, T. Nishimura, "Nickel-stabilized Hexagonal $(Cu,Ni)_6Sn_5$ in Sn-Cu-Ni Lead-free Solder Alloys", *Scripta Materialia*, 2008, Vol.59(2), pp. 191-194

[4] E. Nagy, F. Kristaly, A. Gyenes, Z. Gacsi, "Investigation of Intermetallic Compounds in Sn-Cu-Ni Lead-Free Solders", *Archives of Metallurgy and Materials*, 2015, Vol.60(2), pp. 1511-1515

[5] J. W. Yoon, B. Noh, J. H. Yoon, H. B. Kang, S. B. Jung, "Sequential Interfacial Intermetallic Compound Formation of Cu_6Sn_5 and Ni_3Sn_4 Between Sn-Ag-Cu Solder and ENEPIG Substrate During a reflow Process", *Journal of Alloys and Compounds*, 2011, Vol.509(9), pp. L153-L156

[6] S. F. Choudhury, L. Ladani, "Grain Growth Orientation and Anisotropy in Cu_6Sn_5 Intermetallic: Nanoindentation and Electron Backscatter Diffraction Analysis", *Journal of Electronic Materials*, 2014, Vol.43(4), pp. 996-1004

[7] C. Tseng, C. Ho, J. Lee, J. Duh, "Crystallographic Characterization and Growth Behaviour of $(Cu, Ni, Pd)_6Sn_5$ Intermetallic Compound in Ni(P)/Pd/Au/SnAgCu/Cu Assembled Solder Joint", *Journal of Alloys and Compounds*, 2014, Vol.600, pp. 21-28

[8] N. R. A. Razak, X. F. Tan, S. D. McDonald, K. Nogita, "Interfacial Reactions between Different Sn-based Leadfree Solder Alloys and CuNi Substrates", *The Electronic Packaging Interconnect Technology Symposium*, 2019, Vol.701

[9] V. Vuorinen, T. Laurila, T. Mattila, E. Heikinheimo, J. K. Kivilahti, "Solid-state Reactions between Cu(Ni) Alloys and Sn", *Journal of Electronic Materials*, 2007, Vol.36, pp. 1355-1362

[10] A. G. Jackson, "Handbook of Crystallography: For Electron Microscopists and Others", *SpringerLink*, 1991

[11] M. Yang, Y. Cao, S. Joo, H. Chen, X. Ma, M. Li, "Cu_6Sn_5 Precipitation During Sn-based Solder / Cu Joint Solidification and its Effects on the Growth of Intermetallic Compounds", *Journal of Alloys and Compounds*, 2014, Vol.582, pp. 688-695

[12] J. Pan, D. Willie, B. Toleno, "Effects of Reflow Profile and thermal Conditioning on Intermetallic Compound Thickness for SnAgCu Soldered Joints", *Soldering and Surface Mount Technology*, 2009, Vol.21(4)

[13] R. Tian, C. Hang, Y. Tian, L. Zhao, "Growth Behaviour of Intermetallic Compounds and Early Formation of Cracks in Sn-3Ag-0.5Cu Solder Joints Under Extreme Temperature Thermal Shock", *Materials Science & Engineering – A. Structural Material: Properties, Microstructure and Processing*, 2018, Vol.709, pp. 125-133

[14] N. Harif, A. Nadzri, K. Jusoff, "Lead Free Solder Joint Thermal Condition in Semiconductor Packaging", *American Journal of Applied Sciences*, 2010, Vol.7(7), pp. 949-953

[15] F. Sun, P. Hochstenback, W. D. Van Driel, G. Q. Zhang, "Aging Effects on IMC Formation and Joint Strength of Low-Ag SAC Solder/UBM (Ni(P)-Au) for WLCSP", *EuroSimE 2008 – International Conference on Thermal, Mechanical and Multi-Physics Simulation and Experiments in Microelectronics and Micro-Systems*, 2008, pp. 1-4

[16] X. Li, F. Li, F. Guo, Y. Shi, "Effect of Isothermal Aging and Thermal Cycling on Interfacial IMC Growth and Fracture Behaviour of SnAgCu/Cu Joints", *Journal of Electronic Materials*, 2011, Vol.4, pp. 51-61

Chapter 6

Conclusions and Recommendations

A study of the substrate side IMCs was done between SAC305 and Sn0.7Cu substrate solder samples. Comparison of the IMCs was also done under temperature cycling and high temperature storage conditions to determine the feasibility of Sn0.7Cu solder as an alternative in mitigating ILD cracks and delamination risks. With the application of EDX and EBSD techniques, the results showed that there were no significant differences in the IMCs of both substrate solders, confirming Sn0.7Cu solder as a viable alternative. Recommendations were also presented for future work that would provide more understanding and further efforts into the study of IMCs and reliability of solder joints.

6.1 Conclusion

ILD cracking and delamination remain a concern in semiconductor devices even as silicon technology node continues to shrink aggressively. With interconnect size getting smaller and denser, together with the combination of ELK dielectrics, this can increase the risk of failure occurring. Hence, the motivation behind this study was to explore the application of EBSD as an analytical technique to determine the suitability of Sn0.7Cu solder as an alternative to the conventional SAC305 solder in mitigating ILD cracks and delamination.

In Chapter 2, the formation of IMCs in solder joints was discussed along with the effects of reliability testing on the IMCs. EBSD was explored as an analytical technique to study the IMC phases as well as the grain orientation. The EDX analysis technique was also discussed for its potential in providing chemical information that can support the crystallographic data provided by EBSD to obtain a more accurate phase identification.

Chapter 3 discussed the experimental method to study the viability of Sn0.7Cu as an alternative solder to SAC305 in mitigating ILD cracks and delamination. The samples analyzed consisted of two sets of devices, with each set utilizing SAC305 and Sn0.7Cu solders respectively. Each set of the samples were then reliability tested under TCG and HTS conditions and analyzed using EBSD. In EBSD analysis, sample preparation is critical. In this chapter, various sample preparation setups were explored as well to determine the best surface finish that is most suitable for EBSD analysis. It was determined that after grinding, a mechanical polish by diamond suspension followed by broad ion beam polishing on a rotary stage resulted in the best surface finish that is suitable for EBSD analysis.

Subsequently in Chapter 4, the use of EDX analysis to support EBSD data was explored. In EBSD analysis, crystallographic data was obtained. However, without the support of chemical data, there is a probability of mis-indexing phases in the sample. As such the inclusion of chemical data can alleviate this risk of mis-indexed phases. Hence, with the

use of EDX analysis simultaneously with EBSD, the IMC phases present in the samples were able to be identified and analyzed with more accuracy.

Finally in Chapter 5, the SAC305 and Sn0.7Cu substrate solder samples were analyzed and compared via the application of EBSD and EDX. The two sets of samples were also analyzed at post-reliability tested TCG and HTS conditions to determine if there were any significant differences in the IMCs that formed between the two solders. Overall, results have shown that between SAC305 and Sn0.7Cu solders, there were no significant differences in the IMCs that form, at T=0 as well as post-reliability testing. The IMC phases in both solder samples were $(Cu, Ni, Pd)_6Sn_5$ and exhibited a random grain orientation. IMC thickness between the two sets of solder samples were not significantly different as well, concluding that Sn0.7Cu solder is a viable alternative to mitigating ILD cracks and delamination.

6.2 Future Work Recommendations

In this work, Sn0.7Cu substrate solder was mainly studied and compared against SAC305 substrate solder to determine its viability as an alternative to mitigating ILD cracks and delamination. In addition to Sn0.7Cu solder, there are also other solder variants that may be possible candidates as alternatives too. Like Sn0.7Cu, there are also other variants of Sn-Cu solder with varying Cu content, such as Sn1.0Cu or Sn3.0Cu. Although different in Cu content, these Sn-Cu solders do not contain Ag as well. Hence, like Sn0.7Cu, they would also be expected to have a lower Young's modulus as compared to SAC305, making them possible candidates for IMC study. However, alternative solders are also not limited to just Sn-Cu solder. Low temperature solders such as Tin/Bismuth (Sn-Bi) could also potentially result in better solutions to mitigate ILD cracks or delamination.

Furthermore, with next generation interconnects getting smaller and flexible in form factor, such designs will be used increasingly in wider and more unconventional environments [1]. As a result of the interest in such high performance and compact devices, the effects of high-density current on solder joint reliability have become one of the most important

challenges. Several reliability issues can occur due to the high level of current density. One such reliability risk is the failure induced by electromigration (EM). Hence, it would also be of interest to study the effects of electromigration on the various substrate solder joints and how it may affect the reliability.

6.2.1 Low Temperature Solder

The use of low temperature solder has become more ubiquitous in the recent years. They are often used in temperature sensitive applications where components cannot be subjected to the peak temperatures that typical Pb-free solders are exposed to. In lead-free soldering, temperatures can go up to 240 – 250^{o}C. Furthermore, with the continued reduction in size of electrical components and devices, the higher reflow temperature of solders like SAC305 will result in thermal warpage of the components.

With the use of indium (In) or bismuth (Bi), the melting points of Sn-based solders can be significantly lowered [2]. Sn-In and Sn-Bi solders are two examples of Pb-free solders that have substantially lower melting points than Sn-Cu or Sn-Ag-Cu solder, as shown in Table 6.1.

Table 6.1: Melting temperature range and peak reflow temperature range of several solder alloys [2].

Solder Alloy	Melting Temperature (^{O}C)	Peak Reflow Temperature (^{O}C)
SAC305	219	240 – 250
Sn0.7Cu	227	245 – 255
89Sn-3Ag-5Bi-8In	200 – 205	220 – 230
48Sn-52In	118	140 – 150
42Sn-58Bi	138	160 – 170

Sn-Bi solder is one of the most commonly used low temperature solders and as shown from Table 6.1, the peak reflow temperature ranges between 160 – 170^{O}C, which makes it suitable for temperature sensitive assemblies. Furthermore, Sn-Bi solder is also compatible with other Pb-free solder. This makes it very well-suited in the step soldering process where

successive joints in an assembly are combined using solders of gradually lower reflow temperatures so as not to affect the previously soldered joints [3].

The low reflow temperature for Sn-Bi solder can also potentially minimize the IMC growth in the joints. As shown in Equation 5.1 in Chapter 5, temperature is a factor that can affect the IMC growth rate. Hence, for Sn-Bi, the low reflow temperature can potentially minimize the growth of the brittle IMCs in the solder joints as it was observed that higher temperatures generally contribute more towards the IMC growth. The IMC layer that typically forms in the Sn-Bi solder system is reportedly similar in composition to the IMCs generally observed in Sn-Cu solder systems, with the growth of Cu_6Sn_5 IMCs and the inhibition on the formation of Cu_3Sn layer at the substrate side [4]. The low soldering temperature together with the similar properties of conventional Pb-free solder makes low temperature solders like Sn-Bi worth exploring as potential solder alternatives.

6.2.2 Effects of Electromigration on IMC Evolution

Electromigration (EM) refers to a mass diffusion-controlled occurrence, where atoms are transported under a high current density in solder joints. Conditions during intended field usage would typically include electrical biasing as well, where failures can potentially occur as a result of EM. In field conditions, the growth of the IMC can affect the overall strength and mechanical properties of the solder joint [5]. Hence, another opportunity for further work would be to study the growth of IMCs under the influence of an electric current and understand how the electric current can affect the mass transportation in the solder joints.

In the absence of an electric current, the IMC formation and growth at the substrate side of the solder joints is driven by the difference in chemical potential between the substrate pad and solder joint. With the introduction of a high current density, the current transport can displace the ions and influence mass transport [5]. The transfer of momentum from electrons to atoms is the driving force for the mass transport and this can affect the IMC formation in the solder joint. Therefore, investigations of the IMC formations at the cathode

and anode sides of the solder will allow a better understanding of the polarity effect as a result of the electric current.

Lastly, comparison of the IMC formation in samples under the influence of EM can also be done with the samples studied in this work. This will allow the determination of the difference in effects of EM on IMC evolution against the effects of thermal influence on the IMC and whether if current or heat plays a bigger influence on the solder joint reliability.

References

[1] T. K. Lee, T. R. Bieler, C. U. Kim, H. Ma, “Fundamentals of Lead-free Solder Interconnect Technology: From Microstructures to Reliability”, 2014

[2] Surface Mount Process, “What Do You Think of Low Temperature Lead Free Solder Paste?”, 2021 [Online]. Available: https://www.surfacemountprocess.com/low-temperature-lead-free-solder-paste.html

[3] Indium Corporation, “Low Temperature Solders: Important, Valuable”, 2014 [Online]. Available: https://www.indium.com/blog/low-temperature-solders-important-valuable.php

[4] F. Wang, Y. Huang, Z. Zhang, C. Yan, “Interfacial Reaction and Mechanical Properties of Sn-Bi Solder Joints”, *Materials (Basel)*, 2017, Vol.10(8), pp. 920

[5] H. Gan, K. N. Tu, “Effects of Electromigration on Intermetallic Compound Formation in Pb-free Solder-Cu Interfaces”, *52nd Electronic Components and Technology Conference 2002*, 2002, pp. 1206-1212